5-2016

Microstructure and Creep Deformation Behavior of a Hierarchical-Precipitate-Strengthened Ferritic Alloy with Extreme Creep Resistance

Gian Song
University of Tennesse - Knoxville, gsong1@vols.utk.edu

To the Graduate Council:

I am submitting herewith a dissertation written by Gian Song entitled "Microstructure and Creep Deformation Behavior of a Hierarchical-Precipitate-Strengthened Ferritic Alloy with Extreme Creep Resistance." I have examined the final electronic copy of this dissertation for form and content and recommend that it be accepted in partial fulfillment of the requirements for the degree of Doctor of Philosophy, with a major in Materials Science and Engineering.

Peter K. Liaw, Major Professor

We have read this dissertation and recommend its acceptance:

Yanfei Gao, Hahn Choo, Hairong Qi

Accepted for the Council:

Carolyn R. Hodges

Vice Provost and Dean of the Graduate School

(Original signatures are on file with official student records.)

Microstructure and Creep Deformation Behavior of a Hierarchical-Precipitate-Strengthened Ferritic Alloy with Extreme Creep Resistance

A Dissertation Presented for the
Doctor of Philosophy
Degree
The University of Tennessee, Knoxville

Gian Song
May 2016

ACKNOWLEDGEMENTS

I want to pay my sincere gratitude to all those who helped me complete the Ph.D. in Materials Science and Engineering. I would like to thank my academic advisor Prof. Peter Liaw for his instructions on my graduate study and guidance on my professional career. I am grateful to my committee members, Profs. Hairong Qi, Prof. Yanfei Gao, and Prof. Hahn Choo for their helpful discussions and suggestions on my dissertation work. I greatly appreciate the characterization of the particle-dislocation interactions by transmission-electron microscopy (TEM) from Prof. Mingwei Chen at Tohoku University. I'd like to thank Dr. Jonathan Poplawsky for helping me characterize the precipitate by atom-probe tomography (APT) through the Center for Nanophase Materials Sciences (CNMS) program at the Oak Ridge National Laboratory (ORNL). The completion of this work would not be possible without the help from Prof. Dunand at Northewstern University for the compression creep tests, Dr. Xie Xie for his tutoring on mechanical testing, Dr. Zhiqian Sun for the teamwork in writing journal papers/progress reports/proposals, Dr. Lin Li for his tutoring on finite-element simulations, Dr. Bjørn Clausen for helping me analyze the neutron-diffraction data, Dr. John R. Dunlap for teaching me how to operate TEM at The University of Tennessee, Knoxville, the machine shop members, Doug Fielden, Larry Smith, and Danny Hackworth, for their help on sample machining.

This work was supported by the Department of Energy (DOE), Office of Fossil Energy Program, under Grants of DE-09NT0008089, DE-FE0005868, and DE-FE-0024054 with

Mr. Richard Dunst, Mr. Vito Cedro, Dr. Patricia Rawls, Mr. Steven Markovich, and Dr. Jessica Mullen as the program managers. The work has been benefitted from the use of the Lujan Neutron Scattering Center at the Los Alamos Neutron Science Center (LANSCE), which is funded by the Office of Basic Energy Sciences (DOE). Los Alamos National Laboratory is operated by the Los Alamos National Security LLC under the DOE Contract number of DE-AC52-06NA-25396. The present research was supported by the CNMS at the ORNL, which is sponsored by the Scientific User Facilities Division, Office of Basic Energy Sciences, U.S. Department of Energy. The beamtime at ENGIN-X was awarded from ISIS, Rutherford Appleton Laboratory (United Kingdom). ISIS is funded by the Science and Technology Facilities Council. I am grateful to Profs. Morris Fine, Gautam Ghosh, and David Dunand at Northwestern University, Prof. Mark Asta at the University of California, Berkeley, and Prof. Chain T. Liu at the City University of Hong Kong for their collaborations in these DOE programs.

Lastly and most importantly, I would like to dedicate my thesis to my parents, Young-Ja Jo and Seung-Seop Song, and to my sisters, Gi-Suk Song, Gi-Ju Song, Gi-Seon Song, and Gi-Yeon Song for their love, encouragement, and support in all my pursuits.

ABSTRACT

Hierarchical NiAl [nickel-aluminium compound]/Ni_2TiAl [nickel-titanium-aluminum compound] or single Ni_2TiAl-precipitate-strengthened ferritic alloys have been developed by adding 2 or 4 weight percent [wt. %] of Ti [titanium] into a previously-studied NiAl-precipitate-strengthened ferritic alloy. A systematic investigation has been conducted to study the interrelationships among the composition, microstructure, and mechanical behavior, and provide insight into deformation micro-mechanisms at elevated temperatures.

The microstructural attributes of hierarchical or single precipitates are investigated in the Ti-containing ferritic alloys. Transmission-electron microscopy in conjunction with the atom-probe tomography is employed to characterize the detailed precipitate structure. It is observed that the 2-wt.-%-Ti alloy is reinforced by a two-phase NiAl/Ni_2TiAl precipitate, which is coherently distributed in the Fe [iron] matrix, whereas the 4-wt.-%-Ti alloy consists of a semi-coherent single Ni_2TiAl precipitate. The creep resistance of the 2-wt.-%-Ti alloy is significantly improved than the NiAl-strengthened ferritic alloy without the Ti addition and greater than the 4-wt.-%-Ti alloy.

The microstructural evolution of precipitates during heat treatment at 973 K is investigated in the 2-and 4-wt.-%-Ti alloys. Transmission-electron microscopy and atom-probe tomography are used to study the precipitate evolution, such as the size, morphology, composition of the precipitates. It reveals that the hierarchical structure within the precipitate of the 2-wt.-%-Ti alloy evolves from the fine two-phase-coupled to agglomerated coarse structures, as the aging time increases. Moreover, the transition from

the coherency to semi-coherency is concomitant with that of hierarchical structure within the precipitate.

In-situ neutron-diffraction experiments during tensile and creep deformations reveal the interphase load-sharing mechanisms during plastic deformation at 973 K. The evolution of lattice strains during high-temperature deformation is further verified by crystal-plasticity finite-element simulations. In-situ neutron-diffraction experiments during stress relaxation at 973 K exhibits the load, which is transferred from the matrix to precipitate is relaxed, which indicate the occurrence of the diffusional flow along the matrix/precipitate interface.

These results could provide a new alloy-design strategy, accelerate the advance in the development of creep-resistant alloys, and broaden the applications of ferritic alloys to higher temperatures.

TABLE OF CONTENTS

LIST OF TABLES

LIST OF FIGURES

CHAPTER 1 INTRODUCTION

Recent decades, extensive projects all over the world have been conducted to develop high-temperature materials with better temperature and stress capabilities for fossil-energy power plants [1-9]. This trend is due to the fact that the energy efficiency of the plants and the emission of the greenhouse gas are strongly dependent upon the steam temperature and pressure of the operating condition. Figure 1 shows the plant efficiency as a function of temperature and pressure. Note that all figures are listed in the Appendix. An increase of the operating temperature from 813 to 1,033 K and the pressure by 10 MPa lead to a rise of the efficiency of 5.3 %. Fossil-energy plants operating above a steam pressure of 22 MPa and steam temperature at 813 to 838 K are termed to the supercritical, and those operating at > 22 MPa and > 838 K are termed to the ultra-supercritical (USC). Currently, ultra-supercritical (USC) fossil-energy plants require an increase of the steam temperature to 1,033 K and the steam pressure to 35 MPa [10, 11].

Nowadays, the most efficient fossil-power plants operate in the steam temperatures of the 873 K range [12]. It is expected that steam temperatures will rise another 50 to 100 K in the next 20 to 30 years [12]. Figure 2 exhibits the maximum allowable stresses as a function of temperature for comparing the temperature capabilities of boiler materials for USC plants [13]. In this figure, the high-temperature materials are categorized into three classes (ferritic steels, austenitic steels, and Ni-based alloys). The Ni-based alloys possess the better creep resistance than the austenitic steels. For instance, the Ni-based alloys, such as Inconel 740, Haynes 230, Inconel 625, Inconel 617, HR6W, and HR 120 have a much higher temperature capability (in decreasing order as listed),

relative to austenitic steels. The ferritic steels are normally utilized at lower temperatures than the austenitic steels. Figure 2 also indicates the actual operating temperatures for each material. For example, ferritic steels are limited up to a metal temperature of ~ 893 K, while austenitic steels can be used up to ~ 948 K. At metal temperatures higher than this, Ni-base alloys with better temperature- and stress-capabilities are generally employed.

Ferritic steels have been well employed for heavy-section components, such as pipes and headers in fossil-power plants, due to good thermal conductivity, low thermal expansion, and cost efficiency, as compared to austenitic steels and Ni-based superalloys [3, 12, 14]. For example, an illustration of a header is shown in Figure 3 [12]. Headers are also pipes, but they consist of a number of sub-tubes connected to the header, which carries steam in or out from the header. In general, this header has a dimension of 50 cm in the outer diameter and 10 cm in the wall thickness. Since ferritic steels with the good thermal conductivity and low thermal expansion are less prone to thermal fatigue, as compared to austenitic steels and Ni-based alloys, research during the last decade has focused on developing cost-effective, and creep-resistant ferritic steels capable of operating at temperatures up to 893 K [2]. However, from both the creep and corrosion-resistance point of view, the strongest of ferritic steels is still limited to temperature of 866 K [12].

Masuyama et al. has presented a historical aspect on the development of steels for fossil-power plants, as shown in Table 1 [15]. Figure 4 shows the 10^5 h creep-rupture strength at 873 K by the year of development. The ferritic steels are classified into four

generations, as shown in Table 1. Note that all tables are listed in the Appendix. Table 2 shows the chemical compositions of ferritic steels for boiler materials. In the operating temperatures higher than 823 K, 9Cr and 12Cr steels, listed in Table 2, have been extensively used all over the world as materials for headers and steam pipes in USC plants. The P-92 steel, which has the highest creep resistance among the 9 wt. % Cr steels, is limited below temperatures of 893 K. Beyond 893 K, the 12 wt. % Cr steels, such as P-122, NF12, and SAVE 12 (Table 1), have to be employed (The compositions are summarized in Table 2).

The alloying elements in the development of the ferritic steels play an important role in affecting the microstructure, and, thus, the creep properties [16]. Tungsten, molybdenum, and cobalt are mainly solid-solution strengtheners. Vanadium and niobium forms fine and coherent precipitates of $M(C,N)_x$ carbonitrides in the ferrite matrix, which gives rise to precipitation strengthening. Vanadium also precipitates during tempering or creep. The amount of Chromium is more significant, relative to other alloying elements. Chromium is added for solid-solution strengthening as well as oxidation/corrosion resistance. Nickel is known to improve the toughness, but degrade creep strength. Partial replacement of Ni by Cu helps stabilize the creep strength. Carbon is required to form fine carbide precipitates, but the amount needs to be optimized for good weldability.

Chromium steels (9 – 12 wt. %) are strengthened by fine distributions of $M_{23}C_6$-rich carbides, high density of dislocations, and fine distributions of martensite-lath subgrains. These strengthening microstructures are produced by heat-treatments, including austenitisation at temperatures around 1,373 K, followed by tempering at

around 1,023 K [3, 14, 17]. Figure 5 shows the optical and transmission-electron micrographs after tempering of the 9Cr-2W steel with a chemical composition of Fe-0.100C-8.92Cr-1.92W-0.48Mn-0.28Si-0.012O-0.002N (weight percent) [18]. The width of the lath was about 0.5 μm. The $M_{23}C_6$ carbides of about 0.1 μm or less in size are observed as black dots in Figure 5(b) and are dispersed preferentially along lath boundaries and prior austenite grain boundaries. It is worth noting that a high density of dislocations produced by martensitic transformation during quenching still remains after tempering.

Creep experiments on Cr–Mo–W–V-type steels tested at low stresses and long rupture times have shown that the creep-rupture curves have a sigmoidal shape (Figure 6) [19]. The change in shape with increasing the rupture time (lower stress) is indicative of a change in microstructures influenced by the stress and elevated-temperature exposures. Previous studies have shown that this phenomenon is associated with micro-structural instabilities in the alloy, due to precipitation, coarsening, and dissolution of various carbides and other phases during the long-term exposure to elevated temperatures, which limits the applications of ferritic steels to temperatures below 893 K [20-24].

CHAPTER 2 OVERVIEW OF THIS RESEARCH

2.1 Background: Literature Review

2.1.1 NiAl-Precipitate-Strengthened Ferritic Alloys

The NiAl-precipitate-strengthened ferritic alloys have been developed and investigated because of their excellent creep and oxidation resistance [25-29]. The research on the NiAl-precipitate-strengthened ferritic alloys has mainly focused on the microstructural characterization, including precipitation and coarsening kinetics, and room/elevated temperature mechanical behavior [25-27, 30-37].

The microstructure of the NiAl-precipitate-strengthened ferritic alloys is analogous to that of γ/γ′ Ni-based alloys, consisting of a disordered body-centered-cubic (BCC) α-Fe and an ordered B2-structure NiAl phase [38], providing the possibility of achieving the similar strengthening effect of γ/γ′ Ni-based superalloys at room/elevated temperatures [39, 40]. Transmission-electron-microscopy (TEM) studies revealed that spherically or cuboidally shaped precipitates with a B2 (CsCl-type) crystal structure are homogeneously embedded in the Fe matrix with a BCC structure [35, 41, 42]. Atom-probe tomography (APT) was carried out to derive the chemical composition of the B2-type NiAl precipitates in the NiAl-strengthened ferritic alloys [43, 44]. The APT studies revealed that NiAl precipitates mainly contains Ni and Al with a small amount of Fe, while Mo was found to partition preferentially to the Fe matrix. Neutron and synchrotron diffraction investigations on the microstructure of the NiAl-strengthened ferritic alloys revealed that the NiAl precipitate is coherent with the α-Fe matrix from the room

temperature to 973 K (a lattice misfit of 0.01 %), reflecting an excellent resistance to the coarsening behavior of the precipitate during the long-term exposure to elevated temperature [26, 45].

The precipitation kinetics (coarsening behavior) of the NiAl-type precipitates in the NiAl-precipitate-strengthened ferritic alloys has been studied, based on the Lifshitz-Slyozov-Wagner (LSW) theory [29, 35]. The coarsening constants have been determined in the temperature range from 973 to 1,223 K [31, 46, 47]. Calderon et al. derived the coarsening constant of ~ 5 $nm/h^{1/3}$ and interfacial energy of 16 – 42 mj/m^2 at 773 ~ 1,073 K in two NiAl-strengthened ferritic alloys with different amounts of Mo [31]. Calderon et al. [48, 49] suggested that segregation of Mo at the precipitate-matrix interface could result in a reduction of the lattice misfit between the NiAl precipitate and Fe matrix and the sluggish coarsening process of NiAl-type precipitates. However, the APT characterizations found no evidence of the Mo segregation at the interface [44]. Sun et al. [50] also determined the coarsening constants and interfacial energies at 973 ~ 1,223 K in a Fe-10Ni-10Cr-6.5Al-3.4Mo-0.25Zr-0.005B weight percent (wt. %) alloy (denoted as FBB8 in the present study). It was found that the coarsening constants and interfacial energies in their studies are larger than those in the study of Calderon et al. [31]. It was suggested that the discrepancy could be due to the compositional difference between the precipitates [50].

The creep properties of the NiAl-strengthened ferritic alloys have been examined by compressive and tensile creep tests in the stress range of 10 – 350 MPa and temperature range of 873 – 1,273 K [27-29, 51-53]. Vo et al. [53] suggested that the

creep-deformation mechanisms of FBB8 is dominated by a general climb dislocation process with an unexpected high experimental values of normalized threshold stress (a stress below which creep does not appear to occur, or is at least very slow). Based on the transmission-electron-microscopy (TEM) observation, it was proposed that the elastic interactions due to the mismatch in lattice constant between matrix and precipitate lead to additional elastic interactions between precipitates and dislocations, thus, the high threshold stress [53]. Teng et al. reported that the FBB8 possesses a limited creep resistance at 973 K, as compared to other Fe-based materials candidates for steam-turbine applications [25]. In particular, the creep resistance at low rupture stresses is comparable, but as the rupture stress increases, the creep resistance becomes inferior to other Fe-based candidates. In-situ neutron-diffraction studies on the FBB8 at elevated temperatures up to 973 K, conducted by Huang et al., revealed that the extensive diffusional flow occurs at the interface between the precipitate and matrix (interfacial relaxation), thus, inducing an acceleration of the creep deformation [54, 55]. Moreover, this trend was also suggested to be due to the limited mechanical properties of the NiAl precipitate at high temperatures [55-58].

2.1.2 Ni_2TiAl or NiAl/Ni_2TiAl-Precipitate-Strengthened Ferritic Alloys

To improve the creep resistance of the NiAl-strengthened ferritic alloys, a Ni_2TiAl phase (Heusler phase) or NiAl/Ni_2TiAl two-phase as a strengthening precipitate has been suggested due to intrinsically-superior high-temperature properties of the Ni_2TiAl phase and structural similarity between NiAl and Ni_2TiAl phases [59-61]. It has been reported that such microstructures, consisting of a single Ni_2TiAl or two-phase

NiAl/Ni_2TiAl precipitates, which are distributed in the Fe matrix, can be attained by the addition of Ti to the NiAl-strengthened ferritic alloys.

The creep behavior of a $L2_1$-Ni_2TiAl alloy at high temperatures has been investigated [62]. The $L2_1$-Ni_2TiAl structure has an additional ordering with eight B2 unit cells and three distinct sublattices, which provides the extremely stable Heusler type structure at high temperatures. Strutt et al. reported that the single-phase $L2_1$-Ni_2TiAl alloy possesses an excellent creep resistance in the temperature range of 1,026 to 1,273 K in terms of the creep rate, as compared to a single-phase B2-NiAl alloy [62]. It was suggested that the creep strength of the $L2_1$-Ni_2TiAl alloy is due to an inability for a_0<110> dislocations to undergo cross slip in the Heusler structure and the highly stabilized dislocation networks formed by the reaction of a_0<110> dislocations.

A NiAl-strengthened Ni_2TiAl alloy was developed and studied in terms of microstructural characterization and creep behavior [63]. The small cells constituting the large Ni_2TiAl unit cell are ~ 1 % larger in size than the NiAl unit cell, which gives rise to semi-coherent interfaces with a high density of interfacial dislocations in the NiAl-strengthened Ni_2TiAl alloy [62]. It was reported that the creep strength of this alloy is at least comparable with that of the nickel-base superalloy (MARM-200) for values of T/T_m in the range from 0.68 to 0.82 (T and T_m are the creep test and melting temperatures, respectively) [63]. Polvani et al. suggested that the improvement of the creep strength of this alloy, as compared to the single-phase Ni_2TiAl alloy, is due to the differences in operative glide modes between the Ni_2TiAl and NiAl phases and the pre-existing interfacial networks [63]. Specifically, the significance of the dislocation network

stabilized at phase interfaces was emphasized which plays a role in interactions between mobile dislocations and the interfacial networks during creep deformation.

Recently, the Fe-Cr-Ni-Al ferritic alloys containing a single Ni_2TiAl or two-phase NiAl/Ni_2TiAl precipitates embedded in the Fe matrix has been developed by adding various amounts of Ti contents [59-61]. Liebscher et al. reported the formation of hierarchical precipitate structures consisting of two-phase NiAl/Ni_2TiAl precipitate in Fe–15.5Al–12.1Cr–1.0Mo–16.0Ni–xTi ribbon samples with X = 2 and 4 in at. % in the early stage of the aging treatment at 973 K [60, 61]. Transmission-electron microscopy studies of these alloys revealed that the precipitate structure depends upon the amounts of Ti contents. For example, the 2-wt.-%-Ti addition leads to the formation of a parent Ni_2TiAl precipitate reinforced by a fine network of a NiAl phase, while 4-wt.-%-Ti addition gives rise to the inverse type precipitate structure. Liebscher et al. suggests possible mechanisms on the formation of the hierarchical structure in the precipitate [64-67], involving a wetting transition or heterogeneous nucleation on $L2_1$ anti-phase domain boundaries [60, 66, 67]. However, in contrast to microstructural studies, there is no report regarding the effect of the precipitate structure on mechanical behavior of the alloys at elevated temperatures, such as creep properties, due to the restricted sample geometry (ribbon type samples).

To summarize, creep resistance remains a major issue to be further studied. It is crucial to obtain the fundamental understanding on the effect of the Ti addition and the hierarchical structure in the precipitate on the mechanical properties, which allows for the optimization of the microstructural features (the volume fractions, size, inter-particle

spacings of Ni_2TiAl and $NiAl/Ni_2TiAl$ precipitates, and element partitions) as well as excellent properties (room-temperature ductility, high-temperature creep resistance, and oxidation/steam-corrosion resistance).

2.2 Objectives and Motivation

The overall purpose of the sponsored Department of Energy (DOE) program is to design Fe-based alloys with excellent creep, coarsening, and steam-corrosion resistance under the ultra-super critical environment (at a stress level of 35 MPa and temperature of 1,033 K). As a part of the program, the main objective of my Ph.D, research is to (1) design and characterize the microstructures of the hierarchical $NiAl/Ni_2TiAl$ and single Ni_2TiAl precipitate-strengthened ferritic alloys (denoted by HPSFA and SPSFA in this study). The current study utilized using neutron-diffraction (ND), scanning-electron microscopy (SEM), conventional/scanning transmission-electron microscopy (TEM/STEM), and local-electrode-atom-probe (LEAP) (Chapters 3 ~ 4); (2) The second objective is to study the creep resistance of these ferritic alloys and the influence of the precipitate structures on the creep behavior by tension creep tests in the temperature range of 973 ~ 1,033 K (Chapter 3); (3) The last goal is to understand the effect of precipitates (hierarchical and single phases) on the mechanical properties at elevated-temperatures using in-situ neutron diffraction coupled with crystal-plasticity finite-element simulations (Chapter 5), thus, obtaining an in-depth understanding of the creep mechanisms of the coherent-precipitate-strengthened ferritic alloys. The current research could provide an insight into the alloy design and optimization of the

microstructure and creep properties of the ferritic alloys for applications in fossil-fuel plants. Figure 7 shows an overview of the current research.

CHAPTER 3 EFFECT OF TI ON MICROSTRUCTURE AND CREEP BEHAVIOR

3.1 Introduction

The prototype precipitation-strengthened ferritic alloy with a composition of Fe-6.5Al-10Cr-10Ni-3.4Mo-0.25Zr-0.005B weight percent (wt. %) (denoted as FBB8 in this study) consists of coherent B2-NiAl precipitates in the BCC Fe matrix (Figure 8) with a volume fraction (vol. %) of 16 ~ 18 % and an average diameter of 130 nm after the heat treatment (a solution treatment at 1,473 K for 0.5 hours, followed by aging at 973 K for 100 hours) [33]. The morphology of the coherent precipitate is a function of misfit strains and interfacial energies. The spherical shape of the NiAl precipitates indicates the dominance of the interfacial energy and low misfit strain between the matrix and precipitate [68], which is supported by the previous neutron-diffraction (ND) study (a lattice mismatch of 0.01 % at 973 K) [54].

Our approach to improve the creep resistance of ferritic alloys is to introduce a new type of two-phase precipitates with intrinsically-superior high-temperature properties, while retaining the interfacial coherency between the matrix and precipitate [59]. From the available literature, the $L2_1$ (Heusler phase) phase has an excellent creep resistance in the temperature range from 1,026 to 1,273 K [62], and a similar lattice structure/constant for the small lattice mismatch with the BCC Fe structure [69, 70], which satisfies the requirements of our microstructural design. Another strategy for the further improvement of the creep resistance is to establish a hierarchically-structured

precipitate comprising a network of B2-NiAl and $L2_1$-Ni_2TiAl phases. The hierarchical structure is characterized by the relative chemical ordering, spatial dimensions of the phases, and their spatial distribution [61]. Specifically, the Fe-base matrix features the largest length scale, whereas the primary precipitates are characteristic of a smaller length scale. The primary precipitate is further divided by the sub-structure on the lowest length scale. The matrix has a chemically disordered structure (a disordered body-centered-cubic phase), while the constitutive phases in the primary precipitate have chemically ordered structures (B2 and $L2_1$ structures are different from each other in terms of the sublattice occupancy). Such a hierarchical structure has been developed and reported in ribbon samples of Fe–Al–Cr–Ni–Ti alloys and been well used to describe such a microstructure of the two-phase precipitate in the ferritic alloys [60, 61]. In order to design novel hierarchical NiAl/Ni_2TiAl and single Ni_2TiAl precipitate-strengthened ferritic alloys (denoted as HPSFA and SPSFA, respectively, in this study), 2 or 4 wt. % Ti elements were added to the prototype FBB8 alloy, respectively.

3.2 Objective

In this chapter, the microstructural characterization of novel ferritic alloys with 2 or 4-wt.-%-Ti elements, consisting of either single-phase Ni_2TiAl precipitates or two-phase hierarchical NiAl/Ni_2TiAl precipitates are investigated. Systematic investigations were conducted, using the scanning/transmission-electron microscopy (S/TEM), neutron diffraction (ND), and atom-probe tomography (APT). The main objectives of the present study are to study the effect of Ti addition on the microstructures and (2) obtain the important microstructural features, such as size, morphology, and volume fraction of the

precipitates. The in-depth understanding of the microstructure will provide the necessary knowledge to understand the creep-deformation mechanisms, and the insight for the design and optimization of creep-resistant ferritic alloys and for wide and practical applications in advanced steam-turbine systems.

3.3 Experimental Methods

The nominal composition of the alloys is Fe-6.5Al-10Cr-10Ni-xTi-3.4Mo-0.25Zr-0.005B with x = 2 and 4 in weight percent (wt. %). An ingot of the 2-wt.-%-Ti alloy with a dimension of 12.7 × 25.4 × 1.9 cm^3 and a rod ingot of the 4-wt.-%-Ti alloy with 2 kg and a diameter of 5.08 cm were prepared by Sophisticated Alloys, Inc., using the vacuum-induction-melting facility. Hot isostatic pressing (HIP) was applied to the ingots at 1,473 K and 100 MPa for 4 hours in order to reduce defects formed during the casting and cooling processes. These alloys were homogenized at 1,473 K for 30 minutes, followed by air cooling and, then, aged at 973 K for 100 hours.

Scanning-electron microscopy (SEM) was conducted, using a Zeiss Auriga 40 equipped with an Everhart-Thornley secondary-electron detector. The SEM images were analyzed, using the ImageJ software [71] to obtain the sizes and volume fractions of the precipitates, and the averaged values were estimated, using more than 200 particles. The thin foils for scanning-transmission-electron microscopy (STEM) and conventional transmission-electron-microscopy (CTEM) observations were prepared by electropolishing, followed by ion milling at the ion energy of ~ 2 kV and an incident angle of ± 6 degree. The TEM specimens were cooled by liquid N_2 during ion milling. The STEM observations were performed with a JEOL JEM-2100F TEM equipped with

double spherical aberration correctors for probe-forming and image-forming lenses. The high-angle annular dark-field (HAADF) STEM images were acquired, using a detector-collection angle ranging from 100 to 267 mrad, while the bright-field (BF) STEM images were simultaneously recorded, using a STEM BF detector.

The sharp-tip specimens for atom-probe tomography (APT) were prepared in a FEI Nova 200 equipped with a dual-electron-beam and focused-ion-beam (FIB) column. The APT data acquisition was conducted, using a CAMECA local electrode atom probe (LEAP), 4000X HR, equipped with an energy-compensated reflectron lens. The APT measurements were performed in both voltage and laser modes to validate the precipitate compositions and sizes in both modes. The data-acquisition temperature was set to 50 K, and the pulse frequency and fraction were 200 kHz and 20 %, respectively, for the voltage-mode runs. The temperature was set to 30 K, and the laser energy was set to 100 pJ for the laser-pulsed runs. The TEM energy-dispersive X ray spectroscopy (EDS) was conducted, using a Zeiss Libra 200 MC TEM/STEM equipped with an EDS detector, a Bruker X-Flash 5030. The X-ray collection time was between 300 and 500 s, and at least 10 single measurements were obtained. The EDS compositions were averaged over the 10 measurements.

The in-situ neutron-diffraction (ND) experiments were carried out on the Spectrometer for MAterials Research at Temperature and Stress (SMARTS) diffractometer of the Los Alamos Neutron Science Center (LANSCE) facility located at the Los Alamos National Laboratory [72]. The ND instrument utilizes time-of-flight (TOF) measurements, in which the incident beam is polychromatic with a range of wave

lengths, which allows for the ND measurements with a diffraction pattern covering a wide range of d spacings without the rotation of samples or detectors. The ND measurements were conducted in the temperature range from 293 to 973 K. The samples were measured by ND at elevated temperatures after the sample saturated within ± 1 K of the target temperature, and the sample displacement was equilibrated. The ND data were collected for 15 minutes.

Two types of tension-creep samples were machined, (a) a round type with a gage diameter of 3.175 mm and a gage length of 28 mm and (b) a dog-bone type with a cross section of 3 mm × 3 mm and a gage length of 25 mm. Tension-creep tests were conducted at 973 and 1,033 K under a constant load. Samples for tension-creep tests on HPSFA at 1,033 K were subjected to the solution treatment at 1,473 K for 30 minutes, followed by the aging treatment at 1,073 K for 5 hours, which gives a similar size and morphology of the precipitate of the HPSFA aged at 973 K for 100 hours. Step-loading compressive creep tests were conducted at 973 K in which an 8-mm-diameter × 16-mm-height sample was loaded at a constant load until a steady-state creep rate was reached, and, then, the applied load was increased, and so on. Tension tests with a round type sample (a gage diameter of 3.175 mm and a gage length of 28 mm) at 973 K were conducted at the strain rate of 10^{-4} s^{-1}, using the hydraulic Materials Testing System (MTS) machines. A thermocouple was attached to the center of the specimen gauge-length section. The sample was heated to and held at 973 K for at least 0.5 hour until the sample temperature is stabilized at 973 K within ± 10 K.

3.4 Results

3.4.1 Structural Identification on B2-NiAl and $L2_1$-Ni_2TiAl

Two types of precipitate-structures are present in the studied alloys with the single-phase precipitate and two-phase hierarchical precipitate, as shown in Figures 9(a) and (b). The single-phase-precipitate-strengthened alloy (denoted as SPSFA) consists of a $L2_1$-Ni_2TiAl precipitate [Figure 9(a)], while the hierarchical-precipitate-strengthened ferritic alloy (denoted as HPSFA) is composed of a parent $L2_1$-Ni_2TiAl phase strengthened by a fine network of a B2-NiAl phase [Figure 9(b)]. Both precipitates are embedded in the A2-Fe matrix. These three phases (A2-Fe, B2-NiAl, and $L2_1$-Ni_2TiAl) possess similar structures and lattice parameters [69, 70]. Since the present study focuses on the precipitate structures, it is important to obtain a basic understanding of the structural differences between the B2-NiAl and $L2_1$-Ni_2TiAl, which mainly comprise of the precipitates. Figures 9(c)-(d) illustrate the unit-cell structures of the B2-NiAl and $L2_1$-Ni_2TiAl phases, while the corresponding electron-diffraction patterns along the <101> zone axis are shown in Figures 9(e)-(f), respectively. The B2-NiAl phase has an ordered body-centered-cubic (BCC) structure with the preferential site occupancy of Ni and Al atoms [Figure 9(c)]. This ordering behavior leads to the formation of weak-intensity superlattice reflections, such as <010> and <111> (green), besides the fundamental reflections (blue), as shown in Figure 9(e). The $L2_1$-Ni_2TiAl structure has an additional ordering with eight B2 unit cells and three distinct sublattices, which can be identified by the presence of additional superlattice reflections, such as <111> and <131> (red) [Figure 9(f)], as compared to the B2-NiAl structure [Figure 9(e)].

The hierarchical precipitate contains both B2-NiAl and $L2_1$-Ni_2TiAl phases. In order to characterize the hierarchical structure in the precipitate, a dark-field transmission-electron microscopy (DF-TEM) technique was employed in this current study, based on the electron-diffraction information (Figure 9). In certain directions, all the electron-diffraction patterns are overlapped, which makes it difficult to identify the B2-NiAl and $L2_1$-Ni_2TiAl phases in the hierarchical precipitate. For example, all the reflections, including superlattice (red for B2 and green for $L2_1$) and fundamental reflections (blue), along the <100> zone axis, are completely overlapped, as shown in Figure 10(a). However, along the <101> zone axis, additional superlattice reflections, such as <111> and <131>, which are unique to the $L2_1$-Ni_2TiAl structure, are present, as illustrated in Figure 10(b). With the DF-TEM images using the $L2_1$-superlattice reflections, the formation of the $L2_1$ phase can be determined. Another approach to identify the B2-NiAl structure in the hierarchical precipitate is the contrast intensity on the DF-TEM images. It is known that the image intensity of the DF-TEM image is dependent upon the structure factor of the crystal structure and composition [73]. Moreover, the B2-NiAl structure has a higher structure factor than that of the $L2_1$-Ni_2TiAl structure [60]. Therefore, the B2 superlattice reflections (green) give rise to a higher contrast than the $L2_1$ superlattice reflections (red) on the DF-TEM images, as illustrated in Figures 10(a) and (b). These two methods were used in the present DF-TEM characterization to identify the detailed structure of the hierarchical precipitate.

3.4.2 Microstructure of 2-wt.-%-Ti Alloy

A dark-field TEM image of the HPSFA microstructure after the heat-treatment process (a solution treatment at 1,473 K for 0.5 hours, followed by aging at 973 K for 100 hours) is shown in Figure 11(a). The HPSFA contains an average volume fraction of 16.3 ± 2.3 % cuboidal precipitates with an average width of 98 ± 23 nm and length of 111 ± 27 nm embedded in the Fe matrix. A Fe-15.4Al-12.1Cr-1.0Mo-16.0Ni-4.3Ti (in atomic percent) ribbon sample was studied, using TEM, to characterize the detailed microstructures of the two-phase precipitates consisting of B2-NiAl and $L2_1$-Ni_2TiAl phases [60]. A dark-field (DF)-TEM technique was used on the same region employing different reflections unique to the superlattice-ordered precipitate phases. Figure 11(b) exhibits the selected-area-diffraction pattern (SADP) of the [101] zone axis with superlattice reflections of the $L2_1$ structure. Figures 11(c) and (d) are the dark-field (DF)-TEM images acquired on the same region, using different superlattice reflections. Figure 11(c) is a DF-TEM image acquired, using the <111> reflection, and exhibits the narrow dark zones within the $L2_1$ precipitate. The DF-TEM image in Figure 11(d), using the <020> reflection, reveals narrow zones within the parent $L2_1$ phase, showing a higher intensity than the surrounding $L2_1$-precipitate phase. The DF-TEM image, using the <111> reflection in Figure 11(b), which is unique to the $L2_1$ structure, exhibits the possible presence of anti-phase boundaries (APBs) or a second phase (B2-NiAl) within the $L2_1$ phases. Moreover, the DF-TEM image, using the <020> reflection in Figure 11(b), which is common to both phases, presents the same narrow zones, but brighter contrast than those originating from the $L2_1$ precipitates. Since APBs should be invisible,

when imaged using the <020> or <222> reflections [73], and the B2-NiAl has a higher structure factor, relative to the $L2_1$ structure [60], the bright contrast zones in Figure 11(d) are considered as the B2 phases. Besides the B2 and $L2_1$ phases in the precipitate, dark contrast zones are often observed inside the precipitates of HPSFA, as indicated by white arrows in Figures 11(c) and (d), and are identified as an Fe matrix inclusion by the energy-dispersive X-ray spectroscopy (EDS) analysis in the TEM. It is worth noting that the B2/$L2_1$ and matrix/precipitate interfaces are devoid of misfit dislocations (Figure 11). The cuboidal shape without the interfacial misfit dislocations implies that the precipitate/matrix interface is coherent with a higher misfit strain, as compared to FBB8. Similarly, the flat B2/$L2_1$ interface without misfit dislocations also indicates the coherency of the interface with a high misfit strain, which is in contrast to the two-phase NiAl-Ni_2TiAl alloy (with a high density of interfacial dislocations) [63].

To verify the TEM results, APT was conducted, the results of which are shown in Figure 12. Figure 12(a) shows two iso-concentration surfaces, 10-at.-% Ti and 10-at-% Ni, which clearly show the presence of the B2 and $L2_1$ phases in the precipitate. The compositions of the B2 and $L2_1$ phases derived from the APT analysis are $Ni_{42.8}Al_{38.2}Fe_{14.0}Ti_{4.4}Cr_{0.4}Mo_{0.1}$ and $Ni_{36.2}Al_{29.3}Fe_{18.1}Ti_{15.4}Cr_{0.6}Mo_{0.5}$ in at. %, respectively. A proximity-histogram composition profile between the B2 and $L2_1$ phases is presented in Figure 12(b), and clearly reveals the Ni, Al, Ti, and Fe partitioning behavior within the primary precipitate.

In addition to the primary precipitates, the APT results revealed the formation of a secondary nm-size precipitate in the matrix, as was also observed in alloy FBB8 [25]. A

7.6 at. %-(Ni + Ti) iso-concentration surface is shown in Figure 13(a), which clearly shows the distribution of ultra-fine secondary precipitates in the matrix. The compositions of these ultra-fine precipitates and the adjacent matrix are estimated to be $Ni_{41.6}Al_{34.4}Fe_{17.8}Ti_{3.1}Cr_{2.3}Mo_{0.7}$ and $Fe_{75.8}Cr_{12.8}Al_{7.1}Ti_{0.4}Ni_{1.5}Mo_{2.3}$ in at. %, respectively, as determined from the APT data. A proximity-histogram composition profile between the matrix and a secondary precipitate is shown in Figure 13(b). The compositions of the matrix, $L2_1$, B2, and secondary precipitates are summarized in Table 3. Similar duplex precipitates were observed in the NiAl-strengthened ferritic and Ni-based alloys [28, 74]. It is believed that the ultra-fine precipitates formed during air-cooling and completely dissolved in the matrix at 973 K [25]. Thus, these secondary precipitates significantly contribute to the room-temperature strengthening, but could not influence the creep properties at 973 K.

The size and volume fraction of the secondary precipitates were derived from the analysis of the APT needle specimen that only included the matrix and secondary precipitates [the inset of Figure 13(c)] and was performed by subtracting the primary precipitates, as shown in Figure 13(a). The average size and volume fraction of the secondary precipitates were determined to be 2.05 ± 0.85 nm and 2.785 %, respectively.

Figure 14 shows the representative neutron-diffraction (ND) patterns of HPSFA measured at room temperature without loading (a reference state, 5 MPa), refined by the General Structural Analysis System (GSAS) Rietveld analysis [75]. The ND patterns of HPSFA contain fundamental matrix/precipitate reflections (e.g., 110, 200, 211, and 220 peaks), and low-intensity superlattice peaks (e.g., 111, 200, 222, 311, and 420 peaks)

from the $L2_1$ precipitate, as shown in Figure 14(a). The ND pattern of HPSFA exhibits that the fundamental peaks of Fe and $L2_1$ phases are overlapped, as shown in the Figure 14(b). Since HPSFA consists of a $L2_1$ phase as a parent precipitate surrounding a small fraction of a B2 phase, as shown in the TEM results (Figure 11), the superlattice reflections are believed to originate from the parent $L2_1$ phase, although ND cannot detect the superlattice reflections (e.g., 111 and 311 peaks, which are unique to the $L2_1$ structure) due to the limited intensity of neutrons. Moreover, the ND with the limited resolution appeared to be incapable of detecting the B2 phase. Thus, the Rietveld refinement was conducted with an assumption of the presence of the Fe matrix and $L2_1$ phases for HPSFA.

The averaged phase strain represents the volume-averaged lattice strain of the individual phase (Fe or $L2_1$), which depends on the elastic and plastic anisotropy of the individual phases. In order to obtain the averaged phase strain, a whole-pattern Rietveld refinement was performed to fit the entire ND spectrum, employing the GSAS Program developed at the Los Alamos National Laboratory [75]. The average phase strain is calculated, using the following formula

$$\varepsilon = (a - a_0)/a_0 \quad (1)$$

where a is the lattice parameter of a given phase measured during heating and/or loading, and a_0 is the corresponding lattice parameter before loading (5 MPa at 973 K). The lattice parameters extracted from the Rietveld-refinement approach were utilized for the misfit calculations, which is defined as

$$\delta = \frac{2(a_{L2_1} - 2a_{Fe})}{(a_{L2_1} + 2a_{Fe})} \quad (2)$$

where δ is the lattice misfit, and a_{Fe} and a_{L2_1} are the lattice parameters of Fe and $L2_1$ phases, respectively.

Lattice parameters of the precipitate and matrix were determined at room temperature, using the Rietveld refinement [75]. Note that the lattice parameter of the $L2_1$ structure phase is about 2 times larger than that of the BCC Fe structure, since a $L2_1$ structure consists of eight sub-lattices of a BCC structure. The lattice parameters of the Fe and $L2_1$ phases at room temperature for SPSFA are 2.8864 and 5.8537 Å, while those of HPSFA are 2.8894 Å and 5.8224 Å, respectively. The lattice misfit between the matrix and precipitate phases at room temperature was calculated, using Eq. (2), to be 1.3 % for SPSFA and 0.7 % for HPSFA, respectively.

3.4.3 Microstructure of 4-wt.-%-Ti Alloy

Figure 15 shows the secondary-electron microscopy (SEM) and dark-field transmission-electron microscopy (DF-TEM) images of the Ni_2TiAl-strengthened ferritic alloy aged at 973 K for 100 hours after the solution treatment at 1,473 K for 0.5 hour. The SEM image in Figure 15(a) exhibits elliptical precipitates homogeneously distributed in the Fe matrix with an average size of 220.7 ± 46.2 nm and volume fraction of 22.2 ± 2.2 %. Note that the precipitate shape is elliptical, and, thus, the average size is derived from a minor diameter of the ellipses. Figure 15(b) shows a selected-area-diffraction-pattern of the [110] zone, which reveals the formation of the $L2_1$ structure. This pattern contains two types of super-lattice reflections; <111> and <131> unique to the $L2_1$ structure, <222> and <020> common to both $L2_1$ and B2 structures [60]. The DF-TEM taken along the [110] zone axis, using the <111> super-lattice reflection, reveals the formation of the

$L2_1$-type precipitate with misfit dislocations at the matrix/precipitate interface, as denoted by blue arrows in Figure 15(c). The DF-TEM images using the <222> or <020> reflections (not shown) revealed that there is no B2-type phase formed in the precipitate, as reported in Ref. [76]. The presence of the misfit dislocation indicates a relatively-larger difference in the lattice parameters between the Fe matrix and $L2_1$-type precipitate, and semi-coherent interface [76], as compared to the FBB8 [54].

Moreover, nano-scaled zones are often observed inside the $L2_1$ precipitate [76], as indicated by white arrows in Figures 15(a) and (b). In order to characterize the nano-scaled zone, energy-dispersive X-ray (EDS) line scanning was conducted, as shown in Figure 16. Figure 16 presents (a) a high-angle annual dark-field (HAADF) scanning-transmission-electron micrograph (STEM) and (b) a EDS-line profile of constitutive elements. The EDS line scanning was conducted along the red line in Figure 16(a). The inclusion in the precipitate is enriched in Fe and Cr, while the amounts of other elements, such as Ni, Al, and Ti, significantly reduce, as shown in Figure 16(b). These results support that the inclusion inside the precipitate is the Fe phase [76]. The EDS measurements were conducted to derive the compositions of the Fe matrix and $L2_1$ precipitate [76]. Due to the presence of the Fe-rich inclusion inside the $L2_1$ precipitate, care was taken to avoid the Fe-rich inclusion for the EDS measurements on the $L2_1$ precipitate. The composition of the bulk sample, Fe matrix, and $L2_1$-type precipitate is summarized in Table 4.

The $L2_1$-Ni_2TiAl phase has an off-stoichiometric composition with a Al/Ti ratio of 5/3 rather than 1/1. A composition of the $L2_1$-N_2TiAl phase was derived from

calculating structure factors by Liebscher et al., which demonstrates the formation of the off-stoichiometric $L2_1$-Ni_2TiAl phase with an approximate composition of $(Ni_{35}Fe_{15})(Al_{37}Ti_{13})$ in a Fe-15.4Al-12.1Cr-1.0Mo-16.0Ni-4.3Ti (atomic percent, at. %) alloy [60]. Assuming that the Ni sublattice is only occupied by Ni and Fe in the Ni_2TiAl phase [60], this process gives rise to a composition of $(Ni_{35}Fe_{23})(Al_{25}Ti_{17})$ (at. %) in the $L2_1$ phase in the present study. In this study, the $L2_1$-type precipitate has a higher amount of Fe and the lower amount of Al than the previous report [60]. The discrepancy in the $L2_1$ composition reflects a feasibility that Fe atoms are not only occupied in the Ni sublattice but also in the Ti sublattice, which leads to an approximate composition of $(Ni_{35}Fe_{15})(Al_{25})(Ti_{17}Fe_8)$ (at. %) of the $L2_1$ phase in this study.

The precipitate volume fraction (V_p) can be estimated by the lever rule;

$$V_p = \frac{C_{bulk} - C_{matrix}}{C_{L21} - C_{matrix}} \quad (3)$$

where C_{bulk}, C_{matrix}, and C_{L21} are the compositions of the bulk alloy, Fe matrix, and $L2_1$-type precipitate, respectively. Figure 17 shows a plot of ($C_{bulk} - C_{matrix}$) vs. ($C_{L21} - C_{matrix}$) for 6 elements (Fe, Cr, Al, Ni, Ti, and Mo), which gives rise to a reasonable linear fit. The volume fraction of the $L2_1$ phase is determined from the slope and found to be about 24.8 ± 2.1 %, which is in reasonable agreement with the SEM-image analysis (22.2 %) in Figure 15(a).

The Rietveld-refinement technique was used to obtain average lattice parameters of the Fe and $L2_1$-type phases, using the GSAS code developed by Larson and Von Dreele [75] at the LANSCE. The average lattice parameters of the Fe matrix and $L2_1$-type precipitate at room temperature are 2.8864 and 5.8537 Å, respectively, and gradually

increase with temperature, as shown in Figure 18(a). The lattice mismatch between the lattice parameters of the Fe and $L2_1$ phases is calculated, using Equation (2). The average lattice parameters of the Fe and $L2_1$ phases, and corresponding lattice misfits at room and elevated temperatures are summarized in Table 5. The lattice misfit at room temperature is 1.39 %, and no clear temperature dependence of the lattice misfit is observed. The thermal strains of both phases were estimated, using Equation (1), and Figure 18(b) shows the thermal strains of the Fe and $L2_1$ phases as a function of temperature. Thermal strains determined, using ND, have been employed to obtain the coefficients of thermal expansion (CTEs) of constitutive phases in composite materials [26, 58]. Similarly, the average CTEs were determined from the slopes of linear fits to the data in Figure 18(b) and found to be 1.34×10^{-5} /K and 1.42×10^{-5} /K for the Fe and Ni_2TiAl phases, respectively. The reported CTE of the α Fe is 1.18×10^{-5} /K [77], which is in agreement with the CTE of the Fe matrix in the current alloy. However, there is no available experimental value of the CTE of the Ni_2TiAl with a high amount of Fe elements. An experimental CTE of a Fe_2TiAl alloy with the $L2_1$ structure has been determined by ND [78], and was found to be 1.45×10^{-5} /K, which is close to that of the Ni_2TiAl phase in the current alloy. The CTEs of the Fe matrix and Ni_2TiAl phases, acquired from the ND results in the present study, are listed in Table 6.

3.4.4 Creep Resistance at 973 K

The creep resistance (the steady-state creep rate and time to rupture as a function of applied stress) of HPSFA at 973 K was compared with FBB8, SPSFA, and conventional ferritic steels of P92, P122, T91, T122, and 12Cr in Figure 19 [22, 53, 79-81]. Tension and compression creep tests were conducted, which cover a wide range of strain rates from 10^{-4} to 10^{-9} s^{-1}, and the creep rates derived from both tension and compression tests are comparable to assure the reliability of the creep experiments in Figure 19(a). The steady-state creep rate of HPSFA at 973 K is significantly reduced by more than four orders of magnitude at corresponding stresses [Figure 19(a)], compared to FBB8 and conventional ferritic steels [22, 53]. The apparent stress exponent (n_{app}) is measured, using the Power law,

$$\dot{\varepsilon} = A\sigma^{n_{app}} \tag{4}$$

where $\dot{\varepsilon}$ is the steady-state strain rate, A is a constant, and σ is the applied stress. The estimated value of n_{app} is higher than 4, observed in single-phase alloys [82]. In precipitate-strengthened alloys, the strain rate can be expressed, using the modified version of the creep equation [83]. In precipitate-strengthened alloys, the strain rate can be expressed, using the modified version of the creep equation [84],

$$\dot{\varepsilon} = B\frac{\mu \boldsymbol{b} D}{kT}\left(\frac{\sigma_a - \sigma_{th}}{\mu}\right)^n \tag{5}$$

where B is a constant, μ is the shear modulus of the matrix, $\boldsymbol{b}$ is the Burger's vector in the matrix, D is the effective diffusivity of a controlled element in the matrix, σ_a is the applied stress, σ_{th} is the threshold stress, and n is the stress exponent of the matrix. The threshold stress at strain rates above 1×10^{-8} s^{-1}, estimated by a linear least-squares

regression of $\dot{\varepsilon}^{1/n}$ vs. $\sigma_a - \sigma_{th}$ with n = 4, is about 186 MPa. This value is more than two times higher than that of FBB8 (69 MPa) [53]. Moreover, the time to rupture at 142 MPa (2,675 hours) is more than two orders of magnitude greater than FBB8 at 140 MPa (about 4.5 hours) [Figure 19(b)]. The creep curves of HPSFA at 973 K and 160 MPa (Figure 20) exhibit a prolonged-secondary region, where the minimum creep rate remains constant, as the creep time increases, in the studied stress range (140 ~ 240 MPa), while those of FBB8 show a dominant extended-tertiary region. The prolonged secondary creep region in HPSFA gives a significantly-improved creep resistance than that in FBB8. In addition, HPSFA shows much better creep resistance than SPSFA with a higher volume fraction of the precipitates [Figures 19(a) and (b)].

3.5 Discussions

Microstructural parameters, such as the volume fractions and the compositions of the constitutive phases (B2-NiAl, $L2_1$-Ni_2TiAl, and Fe phases), are closely related to the alloy chemistry [85, 86]. The volume fractions of the primary NiAl-precipitate in FBB8 (16 ~ 18 %) are determined largely by the amount of Ni and Al [25]. In the current study, the addition of Ti (2 and 4 wt. %) into FBB8 gives rise to volume fractions of the primary precipitates (16 ~ 22 %), comparable to those of FBB8. As Ti partitions preferentially into the primary precipitates (Table 3), two-phase decomposition (B2 and $L2_1$) within the primary precipitate occurs for the 2-wt.-%-Ti alloy, whereas complete ordering from the B2 to $L2_1$ structure occurs in the precipitates of the 4-wt.-%-Ti alloy. It has been reported that similar hierarchical structures can be formed by controlling the Ti

content in Fe-Cr-Ni-Al-Ti alloys [60, 61]. Liebscher et al. suggested the heterogeneous nucleation of B2 zones in $L2_1$ anti-phase domain boundaries as a possible mechanism for the formation of these hierarchical structures in precipitates [60]. Here, the effect of the Ti content on the precipitate structure and creep resistance of the current alloys are discussed in the following sections.

3.5.1 Effect of Ti Addition on Precipitate Structure of HPSAF and SPSFA

- **Volume fractions of precipitates of HPSFA**

By ignoring the formation of the secondary precipitates (minor phase), the volume fraction of the primary precipitates can be calculated, using the lever rule [25],

$$V_m + V_{po} = 1, \text{ where } V_{po} = V_{L21} + V_{B2} \quad (6)$$

$$V_{po} = \frac{C_o - C_m}{C_{po} - C_m} \quad (7)$$

where V_m, V_{po}, V_{L21}, and V_{B2} are the volume fractions of the matrix, primary precipitate, $L2_1$, and B2 phases, respectively, and C_o, C_m, and C_{po} are the compositions of the bulk sample, matrix, and primary precipitate, respectively. C_{po} and, thus, V_{po} cannot be determined from the APT results, since the primary precipitate contains the B2 and $L2_1$ phases with unknown volume fractions. Thus, in order to derive C_{po} and V_{po}, a similar equation was adopted, defined as,

$$V_{B2} = \frac{C_{po} - C_{L21}}{C_{B2} - C_{L21}}, \text{ where } C_{p0} = \frac{C_0 - C_m}{V_{p0}} + C_m \quad (8)$$

where C_{L21} and C_{B2} are the compositions of the $L2_1$ and B2 phases, respectively. In order to acquire C_{po}, V_{B2}, and V_{po}, and, thus, V_m and V_{L21}, reasonable values of V_{po} ranging from 15.0 to 20.0 %, which bracket the value (16.3 %) determined from the SEM-image

analysis [76], were substituted in Equation (8), and the resulting plots of (C_{po} - C_{L21}) vs. (C_{B2} - C_{L21}) were determined. Figure 21(a) shows a plot of (C_{po} - C_{L21}) vs. (C_{B2} - C_{L21}) with V_{po} = 19.4 %, which provides the best linear fit. The slope of the plot in Figure 21 indicates the volume fraction of the B2 phase within the primary precipitates, which accounts for 57.1 % of the volume fraction of the primary precipitate [V_{po}: 19.4 %, V_{B2}: 11.1 %, and V_{L21}: 8.3 %]. The calculated V_{po} is higher than that determined from the SEM image analysis (16.3 %) [76]. This discrepancy could be due to the presence of the secondary precipitate. By considering the secondary precipitates in the matrix, Equations (6) - (8) are modified as follows,

$$V_m' + V_{po} = 1, \text{ where } V_m' = V_m + V_{S.P} \text{ and } V_{S.P} = V_m' \times V_{S.P}' \quad (9)$$

$$C_{p0} = \frac{C_0 - C_m'}{V_{p0}} + C_m', \text{ where } C_m' = V_{S.P}' \times (C_{S.P} - C_m) + C_m \quad (10)$$

where V_m' is the volume fraction of the matrix, including the secondary precipitate, $V_{S.P}$ and $V_{S.P}'$ are the volume fractions of the secondary precipitates in the bulk material and in the matrix, respectively, and C_m' and $C_{S.P}$ are the combined compositions of the secondary precipitates and matrix, and the secondary precipitates, respectively. Substituting the calculated C_{po} into Equation (8) with V_{po} = 17.3 %, the best linear fit can be achieved, and V_{B2} accounts for 49.9 % of V_{po}, as shown in Figure 21(b). The calculated compositions of C_m' and C_{po} are also summarized in Table 3. It should be noted that the calculated C_{po} of Cr and Mo has negative values in Table 3, which could result from the formation of additional minor phases. Indeed, minor phases are often observed within the grains and along the grain boundaries, as shown in the inset of Figure 21(b). The SEM energy-dispersive X-ray analysis indicates that these minor phases are enriched in Zr, Cr, and Mo

(not shown), which could affect the current calculation. Therefore, four elements (Fe, Al, Ni, and Ti), which constitute the primary matrix and precipitate phases, were used for the current plots [Figures 21(a)-(b)]. Based on this calculation, the volume fractions of the matrix, secondary precipitates, and the $L2_1$ and B2 phases in the primary precipitates are 80.4, 2.3, 8.7, and 8.6 %, respectively. Note that $V'_{S.P}$ (2.785 %) was derived from the volume of the APT needle specimen only containing the matrix and secondary precipitates [Figure 13(a)]. Thus, the overall fraction of the secondary precipitate in the bulk material ($V_{S.P}$) was derived, using Equation (9), and is 2.3 %. The volume fraction of the primary precipitates (V_{po} = 17.3 %) derived from the APT-composition analysis is in good agreement with that determined by the SEM-imaging analysis (16.3 %) [76].

- **Precipitate structures of SPSFA at room and elevated temperatures**

The volume fraction of the $L2_1$ precipitate derived from the EDS composition analysis (24.8 %) is in reasonable agreement with the value obtained from the SEM-image analysis (22.2 %) [76]. The EDS measurements reveal that the $L2_1$ phase has an off-stoichiometric composition with the enrichment of Fe, as observed in the previous report [60]. However, the presence of the nano-sized Fe-rich inclusion inside the precipitate could contribute to the EDS measurements on the composition of the $L2_1$ phase. For example, the high amounts of Fe and Cr in the precipitate indicate the possible effect of the Fe-rich inclusion on the EDS measurement. To verify this hypothesis, the neutron-intensity ratio from the matrix and precipitate was used.

A direct separation of the fundamental peaks can be made, using GSAS single-peak fitting (SPF) [75], due to the reasonable intensity of the $L2_1$ phase and well-

separated fundamental reflections, as shown in Figure 22. In this study, fundamental reflections of $(110)_{Fe}/(220)_{L21}$ were selected to determine the intensity ratio, as shown in Figure 23. The intensity ratio of $L2_1$ to Fe can be determined from the structure factor and volume fraction, using the following equations [87]:

$$\frac{I_{hkl}^{L21}}{I_{hkl}^{Fe}} = \frac{\left(F_{hkl}^{L21}\right)^2}{\left(F_{hkl}^{Fe}\right)^2} \frac{v_f}{(1-v_f)} \tag{11}$$

$$F_{hkl}^{Fe} = b_{c0} e^{2\pi i(0h+0k+0l)} + b_{ce} e^{2\pi i(0.5h+0.5k+0.5l)} \tag{12}$$

$$F_{hkl}^{L21} = b_{c0} e^{2\pi i(0h+0k+0l)} + b_{ce} e^{2\pi i(0.5h+0.5k+0.5l)} + b_{h.ce} e^{2\pi i(0.25h+0.25k+0.25l)} \tag{13}$$

where I_{hkl}^{L21} and I_{hkl}^{Fe} are the intensities of the (hkl) peaks in the $L2_1$ and Fe phases, respectively, F_{hkl}^{L21} and F_{hkl}^{Fe} are the structure factors of the (hkl) peaks in the $L2_1$ and Fe phases, respectively, b_{co}, b_{ce}, and $b_{h.ce}$ are the scattering lengths of the corner, center, and half center atoms, respectively, and V_f is the volume fraction of the $L2_1$-type precipitate. The values of scattering lengths are functions of the actual compositions of phases, expressed by:

$$b_{co,ce}^{Fe} = \sum c_{i,co,ce}^{Fe} b_i \tag{14}$$

$$b_{co,ce,h.ce}^{L21} = \sum c_{i,co,ce,h.ce}^{L21} b_i \tag{15}$$

where $c_{i,co,ce}^{Fe}$ and $c_{i,co,ce,h.ce}^{l21}$ are the atomic concentration of the element, i, in the Fe and $L2_1$ phases, respectively, b_i is the scattering length of neutrons by the atom of the element, i, which can be obtained from the literature [88]. The EDS analysis revealed the considerable amount of Fe dissolved in the $L2_1$-type precipitate, which alters the structure factor, and, thus, intensity. Assuming that 15 at. % of Fe in the $L2_1$-type precipitate occupies on the Ni sublattice site, while the rest on the Ti sublattice site, the structure

factors and volume fractions have been calculated for four $(Ni_{35}Fe_{15})(Al_{25})(Ti_{25-x}Fe_x)$ (at. %) compounds with x = 0 ~ 7.5. The compositions, corresponding ratios of structure factors, and volume fractions of the $L2_1$ phase are summarized in Table 7.

The volume fraction of the $L2_1$-phase determined from the SEM-image analysis (22.2 %) is in better agreement with the value (22.7 %) calculated, based on an approximate composition of $(Ni_{35}Fe_{15})(Al_{25})(Ti_{20}Fe_5)$ (at. %) in Table 7, which supports that the $L2_1$-Ni_2TiAl phase is enriched in Fe. Based on the composition of the $L2_1$-Ni_2TiAl phase $[(Ni_{35}Fe_{15})(Al_{25})(Ti_{20}Fe_5)]$ (at. %), the volume fraction of the $L2_1$-Ni_2TiAl phase was recalculated, using Equation (3), and found to be 23.5 ± 2.1 %, which is in better agreement with the volume fractions derived from the SEM-image (22.2 %) and ND (22.7 %) analyses. Assuming that the compositions of the Fe and $L2_1$ phases do not vary at higher temperatures, the volume fraction is calculated at 845 and 973 K, which are given in Table 8. The calculated volume fraction at 845 K remains fairly the same as that at room temperature, but increases to 23.4 % at 973 K. In general, it is known that as the temperature increases, the volume fraction of precipitates decreases. Thus, the increase in the volume fraction is unlikely to happen at 973 K. This trend reflects that the compositions of the matrix and $L2_1$ phases could vary at 973 K. The intensity ratio of $L2_1$ to Fe (I_{L21}/I_{Fe}) in Table 8 remains fairly constant (0.178 ~ 0.179) at room temperature and 845 K. However, the intensity ratio increases to 0.184 at 973 K. With a decrease in the volume fraction at high temperatures, it would be expected that the intensity ratio decreases accordingly (Equation 11). However, structure factors can also contribute to the intensity magnitude, which depends on the compositions of the constitutive phases

(Equations 12 ~ 15). First, more elements from the precipitate, such as Al, Ni, and Ti, could be dissolved into the matrix, which results in a reduction of the intensity of the Fe matrix. This is because Fe has the higher solubility of Al, Ni, and Ti at high temperatures [89], and these solute elements have all smaller scattering lengths than Fe [88]. Second, since the TEM and ND analyses reveal the enrichment of Fe in the $L2_1$-type phase, it can be inferred that more amounts of Fe could be dissolved into the $L2_1$ precipitate at 973 K, which results in an increase in the intensity of the $L2_1$ phase.

The difference in the CTEs between constitutive phases contributes to the temperature dependence of the lattice misfit [90]. The linear CTE of the $L2_1$ phase is slightly higher than that of the Fe matrix [Figure 18(b)], and, thus, the slight increase of the misfit at 845 K is observed (Table 5). However, the misfit at 973 K is smaller than that at 845 K (Table 5). Another feasible influence on the temperature dependence of the misfit is the compositional variation of the two phases. As the temperature increases, the compositional variation starts to occur, which is supported by the increase in the intensity ratio of $L2_1$ to Fe (I_{L21}/I_{Fe}) (Table 8). As mentioned above, it is believed that the Fe matrix has the higher solubility of Al, Ni, and Ti, while the $L2_1$ precipitate contains the more amount of Fe at 973 K, as compared to the room temperature and 845 K. Since the atomic size of Fe is smaller than that of Al and Ti [91], it can be inferred that the increase in the solubility of Al and Ti in the Fe matrix leads to an increase of the lattice parameter of the Fe matrix, whereas the enrichment of Fe in the $L2_1$ precipitate results in a reduction of the lattice parameter of the $L2_1$ phase. Hence, the changes in the lattice parameters of the Fe and $L2_1$ phases result in the decrease of the lattice misfit at 973 K (Equation 2), as

compared to 845 K (Table 5). Based on the misfit evolution (Table 5) and the change of the intensity ratio (I_{L21}/I_{Fe}) (Table 8), it is suggested that the compositional change accompanied with the variation in the volume fraction of the precipitate appears to become significant at temperatures near 973 K.

3.5.2 Effect of Lattice Misfit on Morphology of Precipitate

The lattice mismatch between the Fe and B2/$L2_1$ phases of HPSFA cannot be accurately determined from the present ND measurements, due to the low volume fraction and structural similarity of the B2 and $L2_1$ phases (Figure 14). Assuming that the Fe and $L2_1$ phases only contribute to the ND intensity, the lattice constants of the Fe and $L2_1$ phases were derived and are 2.8894 and 5.8224 Å at room temperature, respectively, which correspond to a misfit of 0.7 %. In contrast, the reasonable intensity of the $L2_1$ phase superlattice and well-separated fundamental reflections of SPSFA made more accurate ND analyses possible (Figure 22). The lattice constants of the Fe and $L2_1$ phases of SPSFA were determined, using the Rietveld full pattern refinements [75]. They are 2.8864 and 5.8537 Å at room temperature, respectively, which correspond to a lattice misfit of 1.3 %. The compositions of the Fe and $L2_1$ phases of HPSFA, determined by atom-probe tomography (APT), are almost identical to those of the Fe and $L2_1$ phases of SPSFA, derived from the TEM EDS analysis (Table 3), and, thus, the lattice mismatch between the Fe and $L2_1$ phases of HPSFA is believed to range from 0.7 to 1.3 %. Our previous study on the microstructure of FBB8 using APT and ND reveals that the lattice mismatch between the B2 precipitate and Fe matrix is near zero [25]. Similarly, the composition of the B2 phase of HPSFA, obtained from APT (Table 3), is close to that of

FBB8 [25]. Hence, it is also believed that the lattice mismatch between the B2 precipitate and Fe matrix of HPSFA is near zero. The TEM observation of the interface morphology among the Fe, B2, and $L2_1$ phases in Figure 11 also supports this approximation: flat interfaces of Fe/$L2_1$ and $L2_1$/B2 (high misfit strains), and round-like interfaces of Fe/B2 (low misfit strains), which is also reflected in the schematic of Figure 24.

The morphology of the coherent precipitates strongly depends on the misfit strain, interfacial energy, and size of the precipitate [68]. With a high level of the misfit strain caused by the lattice mismatch between the matrix and precipitate, the stable shape of the coherent precipitates becomes cuboidal, as observed in HPSFA [Figures 11 and 24(a)]. However, as the size of the precipitate and the lattice mismatch increase, the misfit strain increases accordingly. When the misfit strain becomes higher than the critical level that the microstructure can accommodate, misfit dislocations will form to release the excessive misfit strain at the interface (semi-coherent) [92], which leads to a transition from a cuboidal to an elliptical shape with the reduced misfit strain. This trend is observed in SPSFA with a higher lattice mismatch (1.3 %) and larger precipitate size (220 nm) (Figure 11) than HPSFA (lattice mismatch: 0.7 %, precipitate size: 90 nm), (Figure 15). In contrast, the HPSFA with 2-wt.-% Ti exhibits hierarchical precipitates with a lamellar structure of B2/$L2_1$ phases. It has been reported that such a lamellar structure in the coherent precipitate can lower the elastic strain at the interface [93]. Moreover, the hierarchical precipitate structure with tri-material interfaces in the 2-wt.-%-Ti alloy, consisting of individual bi-material interfaces separated by tri-material boundary lines (Figure 24), may play an important role in maintaining the misfit strain at

a more complex series of interfaces, thus retaining the full coherency of the precipitates. Therefore, we hypothesize that the hierarchical precipitates with the tri-material interfaces in the 2-wt.-%-Ti alloy is particularly effective at retaining the coherency of the misfitting precipitates.

3.5.3 Creep Deformation Behavior

The coarsening behavior of the precipitates is significant for the long-term creep properties [94]. It has been shown that the low mismatch between the precipitate and the matrix in FBB8 is effective in suppressing the structural change, and, thus, leads to the excellent resistance to precipitate coarsening during exposure to elevated temperatures [25, 53]. The temporal evolution of the precipitate size of HPSFA at 973 K is observed to be comparable to that of FBB8 (Figure 25), demonstrating the comparable coarsening resistance of HPSFA at 973 K. Moreover, a large number of interfacial dislocations form at the matrix/precipitate interface on the crept sample of HPSFA at 140 MPa and 973 K for 200 hours, as indicated by blue arrows in Figure 26. Since the specimen under the standard heat treatment is devoid of misfit dislocations, the interfacial dislocation in Figure 26 is formed during creep deformation, which was not observed in NiAl-strengthened alloys [53]. The misfit strain at the interface between the matrix and NiAl/Ni_2TiAl precipitates of HPSFA could lead to an attractive force due to the strain fields of precipitates and dislocations [82]. Thus, more dislocations will be trapped at the interfaces, and the density of the mobile dislocations decreases [82]. However, SPSFA contains a high density of interfacial dislocations in the aged condition, as shown in Figure 15(c), which reduces the misfit strain at the interface. This reduction in the

coherency misfit strain and the presence of interfacial dislocations allowing the pipe diffusion in SPSFA may reduce the effectiveness of the precipitates as obstacles against matrix dislocations by shearing and/or climb-bypass [82], thus increasing the creep rate of the alloy, relative to HPSFA [Figures 19(a) and (b)].

The creep resistance of alloys containing coherent, misfitting precipitates is known to increase as the magnitude of the precipitate/matrix lattice mismatch increases, thus increasing the elastic-strain field created in the matrix by the precipitates [95]; this effect also becomes more pronounced as the precipitate size increases [96, 97] and is explained by the fact that the elastic field in the matrix created by mismatching precipitates enhances the elastic interaction between the precipitate and mobile dislocations [98], reducing the climb rate of the dislocations bypassing the precipitates, and, thus, decreasing the creep rate of the alloy. Similarly, the 2-wt.-%-Ti alloy with the hierarchical structure phase contains coherent precipitates with a cuboidal morphology. This morphology indicates a high level of the elastic-mismatch strain [99, 100], and, thus, a high level of elastic interactions can be expected between the precipitates and dislocations. We believe that this trend explains the high creep resistance of this alloy, but modeling needs to confirm the magnitude of this mechanism, thus, opening the door to a prediction of the optimal concentration of Ti in these alloys.

The creep strength at 923 and 973 K for 10^5 hours is estimated, using the Larson-Miller parameter (LMP) [101], which is compared to the creep strength for the available conventional ferritic steels (T122 and 0.002C) [6, 81]. The LM parameter is defined as $P_{LM} = T (\log t_r + C)$, where T is the absolute temperature in Kelvin, t_r is the

time to creep rupture in hour, and C is a LM constant. Figure 27 presents the LM parameter of HPSFA as a function of stress with C = 36.11, which was employed for high-Cr ferritic steels, such as T122 and 0.002C [6, 81]. Since T122 and 0.002 C steels possess the best creep resistance among the available conventional ferritic steels [6, 81], the LM parameters of the T122 and 0.002C steels are also included for comparison in Figure 27. The creep strength was calculated to be 164 MPa at 923 K for HPSFA, about 64 MPa higher than that of the 0.002C steel (100 MPa), which is the most creep resistant among the available conventional ferritic steels [6]. The calculated creep strength at 973 K was 89 MPa for HPSFA, about five times higher than that (18 MPa) for T122 [81], which is one of the most creep-resistant steels, compared in Figure 19(b). Moreover, the yield strength at 973 K of HPSFA is two times higher (280 MPa) than FBB8 (120 MPa), which also indicates the superior high-temperature properties of HPSFA (Table 9). The considerable increase of the creep and tension strengths implies the possibility of the HPSFA alloy to be used for higher temperatures, such as 1,033 K, which is the currently-required temperature for the USC steam turbines [10].

3.6 Summary

Novel hierarchical or single-precipitate-strengthened ferritic alloys were developed by adding Ti into the NiAl-strengthened ferritic alloy. The addition of the 2-wt.-% Ti leads to the coherent hierarchical precipitate consisting of the parent $L2_1$-Ni_2TiAl phase, which is reinforced by the narrow B2-NiAl zones, whereas the addition of the 4-wt.-% Ti results in the semi-coherent single $L2_1$-Ni_2TiAl precipitates. These precipitates are embedded in the Fe matrix. Systematic microstructural investigations

were conducted, using transmission-electron microscopy (TEM), in-situ neutron-diffraction (ND), and atom-probe tomography (APT).

The aged microstructure of a hierarchical-precipitate-strengthened ferritic alloy (HPSFA) has been studied. HPSFA consists of duplex precipitates embedded in the Fe matrix; primary precipitates with an average width of 98 ± 23 nm, and secondary precipitates with an average radius of 2.05 ± 0.85 nm. The primary precipitate contains a mixture of the B2-type NiAl and $L2_1$-type Ni_2TiAl phases. The compositions of the B2 and $L2_1$ phases are $Ni_{42.8}Al_{38.2}Fe_{14.0}Ti_{4.4}Cr_{0.4}Mo_{0.1}$ and $Ni_{36.2}Al_{29.3}Fe_{18.1}Ti_{15.4}Cr_{0.6}Mo_{0.5}$ in at. %, respectively, while that of the Fe matrix is $Fe_{75.8}Cr_{12.8}Al_{7.1}Ti_{0.4}Ni_{1.5}Mo_{2.3}$ in at. %. The composition of the secondary precipitates is measured to be $Ni_{41.6}Al_{34.4}Fe_{17.8}Ti_{3.1}Cr_{2.3}Mo_{0.7}$ in at. %, which is close to that of the B2 phase in the primary precipitate. Based on the APT-composition analysis, the volume fractions of the matrix, secondary precipitate, $L2_1$ and B2 phases in the primary precipitate are derived, using the lever rule, and are 80.4, 2.3, 8.7, and 8.6 %, respectively.

The aged microstructures of a Ni_2TiAl-precipitate-strengthened ferritic alloy at room and elevated temperatures have been studied. The SEM and TEM observations reveal that this alloy consists of a $L2_1$-type Ni_2TiAl precipitate homogeneously embedded in the Fe matrix with an elliptical shape of 220 nm and a volume fraction of 22.2 %. The TEM energy-dispersive X-ray spectroscopy (EDS) and ND results revealed that the $L2_1$-type Ni_2TiAl phase has an off-stoichiometric composition with the Fe enrichment (about 20 at. %). The volume fraction of the Ni_2TiAl phase is determined, based on the EDS and ND analyses and is found to be 22.7 ~ 23.5 %, which is in agreement with the value

derived from the SEM result (22.2 %). The average lattice parameters of the Fe and $L2_1$ phases and the lattice misfits between them at room and elevated temperatures were determined by the Rietveld refinement, using the General Structural Analysis System (GSAS). The lattice parameters of the Fe and $L2_1$ phases gradually increase with temperature, whereas the lattice misfit exhibits no clear temperature dependence. The intensity ratio of $(110)_{Fe}/(220)_{L21}$, obtained from the single peak fitting technique, increases at 973 K, as compared to room temperature and 845 K. This trend indicates the occurrence of compositional variations of the $L2_1$ and Fe phases, and feasible changes of the lattice parameters, and, thus, the misfit around 973 K, which is also related to the volume-fraction change.

The ND results reveal that the hierarchical structure gives rise to coherent interfaces between the Fe and precipitate phases with optimized misfit strains, which leads to the excellent creep resistance at 973 K. Moreover, the TEM results from the crept sample of HPSFA exhibit a strong interaction between the matrix and mobile dislocations, which indicates the insufficient diffusional flow along the matrix/precipitate interface. This trend is in sharp contrast to the behavior of FBB8 at 973 K. These results could provide a new alloy-design strategy, accelerate the advance in the development of creep-resistant alloys, and broaden the applications of ferritic alloys to higher temperatures.

CHAPTER 4 MICROSTRUCTURAL EVOLUTION DURING AGING TREATMENTS AT 973 K

4.1 Introduction

During the long-term exposure to elevated temperatures, the microstructures undergo morphological evolutions caused by the long-range diffusion-assisted mass transport, such as growth and coarsening [46, 102-105]. The morphological changes of coherent precipitates have been extensively investigated in Ni-based superalloys via experimental and theoretical approaches [68, 99, 106, 107]. Since such microstructural evolutions also affect the degree of the elastic strain [64], and, thus, high-temperatures deformation behavior [108], it is crucial to obtain an in-depth understanding of the microstructural evolutions of HPSFA and SPSFA and their effect on the mechanical properties for both the fundamental study and industrial applications.

4.2 Objective

In this chapter, a systematic characterization of the microstructural evolution in the single-phase Ni_2TiAl precipitates and two-phase hierarchical $NiAl/Ni_2TiAl$ precipitates-strengthened ferritic alloys (denoted as SPSFA and HPSFA, respectively) with different amounts of Ti (2 and 4-wt. %) has been conducted. The microstructural evolutions during heat treatments (solution and aging processes) were investigated through the combined use of characterization techniques [transmission-electron microscopy (TEM), scanning-electron microscopy (SEM), and atom probe tomography

(APT)]. In the solution-treated state, both alloys form the single-phase $L2_1$-Ni_2TiAl precipitate with different sizes, morphologies (irregular and cuboidal shapes), and interface structures (semi- and fully-coherent interfaces). During the subsequent solid-state aging, the 2-wt.-%-Ti alloy (HPSFA) develops the hierarchical microstructure, while the 4-wt.-%-Ti alloy (SPSFA) retains the single-phase $L2_1$-Ni_2TiAl precipitate structure. Moreover, the microstructural distinctions between SPSFA and HPSFA lead to the different growth/coarsening behavior. The main objectives of the present study are to investigate the effects of (1) the Ti amount on the formation of the microstructures, and (2) the single and hierarchical precipitates on the microstructural evolutions. Those aspects will be discussed, in terms of the size, morphology, and spatial distribution of the precipitates and elastic misfit, which provides clear insights and fundamental knowledge into the alloy design and optimization strategy for high-temperature applications, such as fossil-fuel-power plants.

4.3 Experimental Methods

The model alloys has nominal compositions of Fe-6.5Al-10Cr-10Ni-xTi-3.4Mo-0.25Zr-0.005B with x = 2 and 4 in weight percent (wt. %). An ingot of the 2-wt.%-Ti alloy with a dimension of 12.7 × 25.4 × 1.9 cm^3 and a rod ingot of the 4-wt.%-Ti alloy with 2 kg and a diameter of 5.08 cm were prepared by Sophisticated Alloys, Inc., using the vacuum-induction-melting facility. Hot isostatic pressing (HIP) was applied to the ingots at 1,473 K and 100 MPa for 4 hours in order to reduce defects forming during the casting and cooling processes. These alloys were homogenized at 1,473 K for 30 minutes,

followed by air cooling and, then, aged at 973 K for different aging times (1 ~ 500 hours).

Scanning-electron microscopy (SEM) was conducted, using a Zeiss Auriga 40 equipped with an Everhart-Thornley secondary-electron detector. The SEM images were analyzed, using the ImageJ software [71] to obtain the sizes and volume fractions of the precipitates, and the averaged values were estimated, employing more than 200 particles. The thin foils for conventional transmission-electron-microscopy (CTEM) observations were prepared by electropolishing, followed by ion milling at the ion energy of ~ 2.5 kV and an incident angle of ± ~ 5 degree. The TEM specimens were cooled by liquid N_2 during ion milling. The TEM observations were conducted with a Zeiss Libra 200 MC TEM/STEM equipped with an energy-dispersive X-ray (EDX) detector, a Bruker xFlash 5030. The TEM images were acquired at an acceleration voltage of 200 kV. The X-ray collection time was between 300 and 500 s, and at least 10 single measurements were obtained. The Cliff-Lorimer method was used for quantification [109].

Sharp-tip specimens for atom-probe tomography (APT) were made, using standard liftout methods with an FEI Nova focused ion beam (FIB) [110, 111]. The data acquisition was performed, using a CAMECA local electrode atom probe (LEAP) 4000XHR equipped with an energy-compensated reflectron lens. The APT runs were done in a voltage mode for the precipitate-density calculation and a laser mode to achieve long runs or capture large regions of interest, such as the $L2_1$-$NiAlTi_2$ phase. For the voltage-mode runs, the acquisition parameters were as follows: a 50-K base temperature, 200 kHz pulse rate, 20 % pulse fraction, and a 0.5 % detection rate. For the laser-mode

runs, the acquisition parameters were as follows: 30 K, 200 kHz, 25-pJ laser energy, and a 0.5 ~ 2.0 % detection rate.

4.4 Results

4.4.1 Microstructure of HPSFA in the Solution-Treated State

Figure 28 exhibits the microstructure of the HPSFA specimen subjected to the solution treatment at 1,473 K for 0.5 hour, followed by air cooling. The selected area diffraction pattern (SADP) in Figure 28(a) was acquired along the [110] zone axis, which indicates the formation of the $L2_1$-type phase. Figure 28(b) exhibits a dark-field transmission-electron microscopy (DF-TEM) image obtained using the <111>-type reflection, which is unique to the $L2_1$ structure. It is observed that the cuboidal $L2_1$-type precipitates with an average width of 50 nm are preferentially aligned along the elastically softest (100) direction of the Fe matrix, and the precipitates are closely spaced with each other. Moreover, the interface between the $L2_1$-precipitate and Fe-matrix is free of misfit dislocations [Figures 28(b)-(d)].

Dark contrast zones are often observed inside the $L2_1$ precipitate, as indicated by white arrows in Figure 28(b). In order to identify the dark zones inside the $L2_1$ precipitate, the DF-TEM images, using <111>- and <222>-type reflections, were taken on the same region, as shown in Figures 28(c) and (d), respectively. The DF-TEM image in Figure 28(c) clearly shows the presence of curved dark domains in the $L2_1$ precipitates, as denoted by white arrows. However, when imaging using the <222>-type reflection, common to both $L2_1$ and B2 structures, the curved dark domains are invisible in Figure

28(d). Following a report of similar observation on a Fe-15.4Al-12.1Cr-1.0Mo-16.0Ni-4.3Ti in atomic percent (at. %) ribbon sample [60], it is believed that antiphase boundaries (APBs) with a shift vector of R_{100} = 1/2<100> could be present in the $L2_1$-Ni_2TiAl precipitate. Based on the APB extinction rule [73], APBs with R_{100} = 1/2<100> are visible when imaged with the <111>-reflection, while invisible when imaged with the <222> reflection, which is consistent with the present observation. Therefore, it can be concluded that the internal dark domains in the $L2_1$ precipitate are the APBs with R_{100} = 1/2<100>.

Atom-probe tomography (APT) was conducted on the solution-treated sample to obtain the chemical compositions of the constitutive phases on the nano-scale. Figure 29 exhibits (a) two iso-concentration surfaces of 5-at.-% Ni (green) and 5-at.-% Ti (yellow), and atom maps of (b) Al, (c) Ni, (d) Fe, and (e) Ti. The iso-concentration surfaces clearly show two types of precipitates, large primary and ultra-fine precipitates (denoted by secondary precipitate in this study), as illustrated in Figure 29(a). On the closer inspection inside the primary $L2_1$ precipitate in Figure 29(a), nano-scaled Ti depletion zones can be noticed, as denoted by red arrows, while Figures 29(b)-(d) reveal that no clear elemental partitioning of Al, Ni, and Fe atoms is observed. The composition profile in Figure 30(a) is derived along the red arrow in Figure 29(a) and reveals that the plate zones with an approximate width of ~10 nm are accompanied with modest compositional fluctuations (Ti, Ni, and Al). In particular, the amount of Ti is reduced, while those of Ni and Ti are increased in the plate zones. Figures 30(b) and (c) exhibit a proximity histogram of a 13-at.-% Ni iso-concentration surface between the Fe matrix and primary $L2_1$-Ni_2TiAl

precipitate, and a proximity histogram of a 7.6-at.-% Ni + Ti iso-concentration surface between the Fe matrix and secondary precipitate, respectively. Figure 30(b) shows a compositional profile between the Fe matrix and primary $L2_1$ precipitate. The compositions of the Fe matrix and $L2_1$ precipitate were determined from Figure 30(b) and found to be $Fe_{77.20}Al_{6.34}Ni_{1.34}Ti_{0.33}Cr_{12.49}Mo_{2.26}$ and $Ni_{36.81}Al_{33.95}Fe_{18.26}Ti_{9.75}Cr_{0.65}Mo_{0.37}$ in at. %, respectively, which are summarized in Table 10. Based on the TEM results in Figures 28(b)-(c), which reveal the formation of the narrow APBs inside the $L2_1$ precipitate, the plate zones in Figure 29(a) are considered as the APBs.

In addition, a high density of nano-scaled precipitates (denoted by secondary precipitate in this study) is distributed in the Fe matrix, as shown in Figure 29(a). The composition of the secondary precipitate is obtained from the APT analysis [Figure 30(c)], and is $Ni_{42.45}Al_{36.84}Fe_{13.34}Ti_{6.90}Cr_{0.35}Mo_{0.09}$ in at. %. The compositions of the constitutive phases in the solution-treated HPSFA specimen, determined from the APT analysis, are summarized in Table 10. A radius frequency histogram of the secondary precipitate, derived from the iso-concentration surface of 7.6-at.-% Ni in Figure 29(a), is shown in Figure 30(d). Since the secondary precipitates are not observed in the DF-TEM images (Figure 28) due to their small size (1 ~ 6 nm), it is not possible to identify the structure of the secondary precipitate using TEM. However, the composition of the secondary precipitate is different from that of the primary precipitate. In particular, the amount of the Ti in the secondary precipitate is very low, as compared to that in the primary precipitate. Furthermore, the APT study on the microstructure of the HPSFA sample aged at 973 K for 100 hours confirmed the formation and composition of the

secondary precipitate in the Fe matrix (Figures 12 and 13). The composition of the secondary precipitate in the solution-treated sample (Table 10) is close to both the B2 phase in the primary precipitate and secondary B2-precipitate in the sample aged at 973 K for 100 hours (Figures 12 and 13). Based on these findings, thus, the secondary precipitate is considered to be the B2-type phase.

4.4.2 Microstructural Evolution of HPSFA during Aging-Treatments

Figure 31 shows the microstructures of the HPSFA (2-wt.-% Ti) specimens aged at 973 K for (a)-(b) 10 and (c)-(d) 100 hours after the solution treatment at 1,473 K for 0.5 hour. The DF-TEM images acquired using the <002> $L2_1$ reflection in Figures 31(a) and (b) show the precipitates with nano-scaled bright zones, which is in contrast to the solution-treated sample [Figure 28(b)-(c)]. The narrow bright zones are similar in shape and size to that of the APBs observed in the solution-treated sample [Figures 28(b)-(c)]. Note that the super-lattice reflection employed to from the DF-TEM images is common to the B2 and $L2_1$ structures (<001>-B2 and <002>-$L2_1$). By considering the image intensity, and structure factor [60, 73], the narrow zones inside the precipitate are believed to be the B2-NiAl phase, while the surrounding regions are the $L2_1$-Ni_2TiAl phase. This trend indicates that the hierarchical precipitate with a fine network of the B2-NiAl and $L2_1$-Ni_2TiAl phases had been developed during the aging treatment at 973 K for 10 hours.

On the subsequent aging to 100 hours, the well-developed hierarchical structure with a fine network inside the precipitate is observed in the DF-TEM image [Figure 31(c)], which was acquired along the (100) zone axis using the <002> $L2_1$ reflection.

Similar to the sample aged for 10 hours, the cuboidal morphology and spatial arrangements (the close separation and preferential alignment) of the hierarchical precipitates remain the same as those in the solution-treated sample (Figure 28). Furthermore, the precipitate/matrix interface is free of interfacial dislocations, indicative of the retention of the coherent interface during the aging treatment for 100 hours, as can be seen in Figures 31(c) and (d).

The formation of the hierarchically-structured B2-NiAl/$L2_1$-Ni_2TiAl precipitate in the Fe matrix was also found by Liebscher et al. [60, 61] upon aging the Fe–15.5Al–12.1Cr–1.0Mo–16.0Ni–xTi ribbon samples with x = 2 and 4 in at. % at 973 K. In particular, the as-quenched sample of the 2-wt.-%-Ti alloy in the previous study contains a primary $L2_1$-Ni_2TiAl precipitate with internal anti-phase boundaries, and further aging to 10 hours at 973 K leads to the formation of the fine B2-NiAl zones on the anti-phase domain boundaries [60]. The current study exhibits the qualitatively-similar transformation pathway, as compared to the previous work [60]. Liebscher et al. suggests possible mechanisms on the formation of the hierarchical structure in the precipitate [64-67], involving a wetting transition or heterogeneous nucleation on $L2_1$ anti-phase domain boundaries [60, 66, 67].

Figure 32 exhibits the scanning-electron-microscopy (SEM) microstructures of the HPSFA specimens aged at 973 K for (a) 200, (b) 300, and (c) 500 hours. During the aging treatments, striking microstructural variations are observed, as compared to the specimens aged for 100 hours or less (Figure 31). In particular, as the size of the precipitate increases, elongated- and irregular-shaped precipitates are often observed, as

denoted by blue arrows in Figure 32. The number density of the abnormally-elongated precipitates seems to increase with the aging time. Furthermore, the precipitates appear to retain the alignment in certain orientations in Figure 32(a), while the alignment trend is not clearly observed in Figures 32(b)-(c).

Figure 33 presents the TEM microstructure of the HPSFA specimen aged at 973 K for 500 hours. The BF-TEM image in Figure 33(a) exhibits a large precipitate with an irregular shape, as observed in Figure 32. In order to identify the B2 and $L2_1$ phases inside the precipitate, the <111> and <222> superlattice reflections are used to form the DF-TEM images in Figure 33(b) and (c), respectively. The hierarchical structure inside the precipitate is composed of agglomerated domains of the B2-NiAl and $L2_1$-Ni_2TiAl phases, as observed in Figures 33(b) and (c), instead of the fine network (Figure 31). This trend indicates the occurrence of the coarsening of the B2-NiAl and $L2_1$-Ni_2TiAl phases inside the precipitate. It is worth noting that misfit dislocations are often observed, especially at the interface between the Fe matrix and $L2_1$ phase, which reflects the coarsening behavior of the precipitate and leads to the formation of the misfit dislocation, and, thus, the semi-coherent interface.

Besides the large irregular precipitate, there are other types of smaller primary precipitates, for example, one mainly is a single-$L2_1$ precipitate (not shown), while another contains nano-scaled $L2_1$ zones embedded in a parent B2 phase, as presented in Figures 34(a)-(b). Figures 34(a)-(b) are the DF-TEM images on the same region using (a) the <111> and (b) <222> reflections, respectively. The APT data was collected on a similar primary precipitate shown in Figures 34(a)-(b), which is presented in Figure

34(c). Figure 34(c) presents two iso-concentration surfaces of 10-at.-% Ti (yellow) and 10-at.-% Ni (green), clearly illustrating the presence of the narrow $L2_1$-Ni_2TiAl zones embedded in the parent B2-NiAl phase. The compositions of the B2-NiAl and $L2_1$-Ni_2TiAl phases were determined using the APT analysis, and are summarized in Table 11. Figure 34(d) shows the APT results on the Fe matrix, which is located between two primary precipitates. Figures 35(a) and (b) present the proximity histograms of 15-at.-% Ni and 7.5-at.-%-Ti iso-concentration surfaces, respectively, whereas a proximity histogram of the secondary precipitates shown in Figure 34(d) is presented in Figure 35(c). The compositions of the Fe matrix, B2/$L2_1$ phases within the primary precipitate, and the secondary precipitate are determined from Figures 35(a), (b), and (c), and are summarized in Table 11. A radius frequency histogram of the secondary precipitates, obtained from the iso-concentration surface of 7.6-at.-% Ni in Figure 34(d) is shown in Figure 35(d). As observed in Figure 28, the ultra-fine secondary precipitates are present in the Fe matrix. However, the size of the secondary precipitate is smaller [1.5 nm in radius, Figure 35(d)] than that in as-solution-treated sample (1.7 nm in radius, Figure 28). The composition profile between the Fe and the secondary precipitate is presented in Figure 35(c). Although it was difficult to determine the exact composition of the secondary precipitate due to its small size, an approximate composition was obtained from the APT analysis and summarized in Table 11.

4.4.3 Microstructure of SPSFA in the Solution-Treated State

The microstructures of the SPSFA (4-wt.-% Ti) specimen subjected to the solution treatment at 1,473 K for 0.5 hour, followed by air-cooling are presented in Figure 36. The SEM image in Figure 36(a) exhibits the polygonal precipitates distributed in the Fe matrix. Considering the morphology of the precipitate as an ellipse, the size of the precipitate was determined and is 126 ± 28 nm in diameter and 160 ± 33 nm in length, which is about 2 times greater than those of the HPSFA (50 nm). As observed in the microstructures of the HPSFA samples aged for less than 200 hours [Figures 28 and 31], the precipitates in Figure 36(a) seem to have the preferential alignment and close-separation, but not to impinge each other, as indicated by red arrows. The SADP along the (110) zone axis in Figure 36(b) reflects the presence of the $L2_1$-structure phase. According to the electron diffraction and image contrast techniques, as discussed in the Section 3.3.1, conducted on the SPSFA specimens, all the SPSFA specimens subjected to the solution and aging treatments contains a single $L2_1$-Ni_2TiAl phase in the primary precipitate. The DF-TEM images in Figure 36(c) exhibit the formation of primary and secondary $L2_1$-type precipitates. It could be noticed that the primary $L2_1$-type precipitate is decorated with interfacial dislocations, as denoted by white arrows in Figure 36(c). The bright-field (BF) TEM image in Figure 36(d), which was obtained on the same region as Figure 36(c), more clearly shows the formation of the interfacial dislocations around the primary precipitate, suggesting the semi-coherent interface between the Fe matrix and the primary $L2_1$-precipitate. In contrast, the secondary $L2_1$-Ni_2TiAl precipitate is free of the

interfacial dislocations indicative of the coherent interface between the Fe matrix and secondary precipitate.

4.4.4 Microstructural Evolution of HPSFA during Aging-Treatments

Figure 37 exhibits the SEM microstructures of the SPSFA samples aged at 973 K for (a) 1 hour, (b) 10 hours, (c) 50 hours, and (d) 100 hours. The size of the precipitate was measured, using the SEM-image analyses, based on the elliptical-precipitate shape. As expected, the size of the precipitate increases from 130 nm (1 hour) to 220 nm (100 hours), during the aging treatments. There are interesting microstructural variations in this aging stage, as follows. First, the morphology of the precipitates appears to be polygonal and gradually change to an ellipsoidal or spherical shape. This morphological transition seems to become apparent between Figures 37(a)-(b) and Figures 37(c)-(d). Second, the precipitates are closely spaced without impinging each other in Figure 37(a), as denoted by blue arrows. As the precipitate coarsens (the aging time increases), irregularly-shaped precipitates, as indicated by blue arrows in Figure 37(b)-(d), are often observed, and the number density seems to increase. Lastly, the precipitates are preferentially aligned along certain orientations in Figures 37(a)-(b), while the orientation trend is not clearly observed in Figures 37(c)-(d). These three changes (the morphology, distribution, and orientation) are simultaneously emerging in the microstructure evolution of SPSFA during the aging treatment from 1 to 100 hours.

Figure 38 present the TEM microstructures of the SPSFA specimens aged at 973 K for (a)-(b) 1 hour and (c)-(d) 100 hours. The interface between the $L2_1$-Ni_2TiAl precipitate and Fe matrix appears to be aligned along the <100> directions, and the

precipitates are closely located, but not connected, as can be seen in Figure 38(a). However, further aging to 100 hours leads to a loss of the alignment of the precipitates and the coalescence of the primary precipitates [Figure 38(c)], which results from a coalescence between neighboring precipitates, as observed in Figure 38(a). These observations are consistent with the SEM microstructures in Figures 37(a) and (d). Moreover, dark zones with different sizes and spatial distributions inside the $L2_1$ precipitate are observed for both samples, as indicated by red arrows in Figures 38(a) and (c). The DF-TEM electron-diffraction and image-contrast results revealed that the dark zones are not the B2 phase. The microstructure aged at 973 K for 100 hours of SPSFA was characterized using the TEM-EDS in Figure 16, which revealed the formation of the Fe inclusion inside the $L2_1$ precipitate. Based on this finding, it can be inferred that the nano-scaled Fe-matrix inclusion inside the $L2_1$ precipitate in Figure 38(a) formed and had coarsened during the aging treatment at 973 K. Similar to the as-solution-treated microstructure of SPSFA [Figure 36(d)], the precipitates are decorated with a high density of dislocations at the interface, as can be seen in Figures 38(b) and (d), which indicates the semi-coherent interface between the Fe matrix and $L2_1$ precipitate.

4.5 Discussions

4.5.1 Dispersion of Secondary Precipitates

Due to the ultra-fine size of the secondary precipitate, the DF-TEM technique is not capable of detecting the secondary precipitate for the HPSFA and SPSFA samples. The secondary precipitate with a size of 10 ~ 30 nm is only visible in the SPSFA

specimen solution-treated at 1,473 K, while the presence of the secondary precipitate in the SPSFA sample aged at 973 K cannot be established. However, the APT results on the HPSFA sample aged at 973 K reveal the formation of ultra-fine secondary precipitates (with a radius of 1 ~ 2 nm), which reflects the possible formation of secondary precipitates in the aged SPSFA samples. Moreover, the size of the secondary precipitate in the HPSFA sample aged at 973 K remains fairly constant during the aging treatments at 973 K, but they are smaller than that in the solution-treated one at 1,473 K, suggesting that the secondary precipitates are completely dissolved into the Fe matrix at 973 K (the aging-treatment temperature) and form during the cooling process [25, 30]. In order to confirm these hypotheses, Vickers-hardness tests were conducted on the SPSFA samples aged at 1,073 K for different aging times, followed by air cooling.

Considering the effect of the primary precipitate on the strengthening behavior, the hardness of the specimens aged at 1,073 K is expected to be lower than that at 973 K, due to the coarsened primary precipitate. However, the hardness of the samples aged at 1,073 K is greater than those of the specimens aged at 973 K for the given aging times (Figure 39). Therefore, it is believed that the hardness increase is associated with the strengthening contribution of such ultra-fine secondary precipitates, due to the significant decrease in the inter-spacing of the secondary precipitates in the matrix [74]. Furthermore, the higher hardness at 1,073 K than that at 973 K reflects that the size, volume fraction, and distribution of the secondary precipitate are strongly dependent on the aging temperature (cooling rate), and the higher aging temperature (a higher cooling rate) gives rise to the larger size and higher volume fraction of the secondary precipitate.

Sun et al. [112] investigated the effect of the cooling rate on the size and volume fraction of the secondary precipitate using the ultra-small angle X-ray scattering, and demonstrated that the size and volume fraction of the secondary precipitate in a NiAl-strengthened ferritic alloy are affected by the cooling rate. Due to the fine distribution of the secondary precipitate, the strengthening effect of the secondary precipitate is believed to be significant than that of the primary precipitate at room temperature [30, 112]. However, as the secondary precipitate is completely dissolved in the Fe matrix at the high temperature (in this case, the aging temperature of 973 K), no strengthening effect from the secondary precipitate is expected at 973 K. Systematic investigations concerning the effects of the secondary precipitates on mechanical properties, which are beyond the scope of the present study, have been performed in various alloy systems, such as Ni-based superalloys, and NiAl-strengthened ferritic alloys [28-30, 50, 74, 112, 113].

4.5.2 Evolution of Primary Precipitates and Their Effect on Strengthening

Microstructural evolution involves various kinetic processes (such as diffusion, domain switching, or grain-boundary migration) under the driving force being the generalized functional derivative of the total free energy with respect to field parameters, such as the concentration and polarization [114-116]. For our alloy system that consists of second phases and lattice defects, the total free energy shall include the free energy of mixing (which dictates the phase diagram), the phase-boundary energy among the matrix and two types of precipitate phases, and the long-range elastic energy due to the lattice mismatch and lattice defects. Figure 40 illustrates the microstructural evolutions of the precipitates during the aging treatments at 973 K in terms of the internal structure and

morphology of the precipitates and elastic strain at the interface. To illustrate this schematic, next we discuss the dependence of the total free energy on the precipitate size, shape, and other geometric parameters.

The classic work by Eshelby [117] investigates the strain energy of an inclusion-matrix system. For an inclusion that has a lattice mismatch strain with the matrix phase (in general, ε_{ij}^{m}), a self-stress field will be induced, as governed by the equilibrium equations:

$$c_{ijkl}\left(\varepsilon_{kl,j}^{total} - \varepsilon_{kl,j}^{m}\right) = 0 \tag{16}$$

where c_{ijkl} are the elastic constants. For a spherical inclusion with a hydrostatic lattice mismatch (so that $\varepsilon_{ij}^{m} = \varepsilon_{m}\delta_{ij}$ with the Kronecker delta, δ_{ij}), the strain energy is

$$E_{el} = \frac{8\pi}{3}\mu\frac{1+v}{v}\varepsilon_{m}^{2}a^{3} \tag{17}$$

where a is the radius of the spherical inclusion, and μ and v are the shear modulus and Poisson's ratio, respectively. For an arbitrarily-shaped inclusion, the elastic-strain energy follows the same scaling law in Eq. (17),

$$E_{el} = f\left(c_{ijkl}/c_{1111}, shape\right)c_{1111}\varepsilon_{m}^{2}V \tag{18}$$

where V is the inclusion volume, and f is a prefactor that depends on the shape of the inclusion and the ratios of elastic constants.

The equilibrium shape of the inclusion minimizes the following free energy:

$$\prod = \int_{\Gamma}\gamma(\boldsymbol{n})dA + E_{el} \tag{19}$$

where **n** gives the surface normal of the inclusion. Since the first term in Eq. (19) is quadratic in a, and the second term is cubic in a, a critical size can be defined by comparing these two terms, given by

$$a_{crt} = \frac{3\gamma_0}{2\mu\varepsilon_m^2}\left(\frac{1-\nu}{1+\nu}\right) \tag{20}$$

where γ_0 denotes the magnitude of the surface energy. When the inclusion size is smaller than a_{crt}, the surface energy dominates, and the shape of the inclusion will be governed by the interface-energy anisotropy in $\gamma(\boldsymbol{n})$. Experimental observations of the precipitate morphology in coherent systems, such as Ni-based superalloys [64, 68, 104, 118, 119], can be qualitatively explained from the above thermodynamic formulation. For example, a lower lattice misfit between the precipitate and matrix lowers the ratio of the elastic strain energy to interface energy. Thus, the equilibrium shape of the precipitate is governed by the interface-energy anisotropy. Usually the degree of this type of anisotropy is weak. Hence, small precipitates are spherical, as observed in low-misfit Ni-based superalloys and NiAl-strengthened ferritic alloys [26, 31, 40, 46, 120]. In contrast, with a higher lattice misfit or a lower interface energy (i.e., equivalent to the situation, when the inclusion size is larger than a_{crt}), the elastic-strain energy dominates, which leads to the cuboidal shape of the precipitate [99, 100] in crystals with the cubic symmetry. Moreover, the elastic strain influences the spatial distribution of the coherent precipitate, such as the alignment of the interface and close inter-precipitate separation. In order to minimize the elastic interaction, the inclusions will align in the compliant directions or assume a cuboidal shape that resembles the dependence of the direction modulus on the crystallographic orientation [118, 121, 122]. It has been reported that the elastic-strain

energy at the interface leads to an elastic interaction between coherent precipitates, which is attractive at long distances and repulsive at short distances [64, 121]. The microstructure of the SPSFA specimen subjected to the solution treatment [Figure 40(a)] shows the alignment of the interface and close inter-separation of the precipitates, which indirectly reflects the presence of the elastic strain and interaction (the short-range repulsive force between precipitates).

Johnson and Cahn [93] further points out that when $a \gg a_{crt}$, the spherical inclusion will transform into needle-like ellipsoidal ones, which further reduce the elastic-strain energy. In the SPSFA case, this trend is not observed at all because of the formation of misfit dislocations even at small sizes, as shown in Figure 40(a). For the HPSFA case, for moderate sizes, such as Figures 40(b) and (d), the overall shape is still cuboidal. The elongated shape in Figure 40(e), however, is not due to the elastic interaction, as discussed in Johnson and Cahn [93]. The shape in Figure 40(e) is formed because of the coarsening and agglomeration behavior of two neighboring precipitates, and the corresponding elastic interaction is relaxed because of misfit dislocations on the precipitate-matrix interface. On the other hand, we note the formation of the lamellar structure of APB and eventually B2 structures in Figures 40(b) and (d), respectively. In these cases, there are two stress fields, one being caused by the lattice mismatch between the $L2_1$ phase and matrix, and the other being caused by the mismatch between the $L2_1$ phase and APB (or B2 phase). According to Eshelby [117], the former field gives rise to a constant strain field inside the $L2_1$ phase, so that the interaction energy of these two stress fields will be independent of the shape of the APB/B2 phase. On the other hand,

the latter field will give rise to a lower strain energy, if the second phase is elongated by the mechanism described in Johnson and Cahn [93].

With the appearance of interface dislocations, the misfit strain will be reduced accordingly, as given by $\varepsilon_m^{eff} = \varepsilon_m - b/\lambda$ where the line density of dislocations is $1/\lambda$. For simplicity, considering again a spherical inclusion, the total strain energy will be

$$E_{el} = \frac{8\pi}{3}\mu\frac{1+v}{1-v}a^3\left(\varepsilon_m - \frac{b}{\lambda}\right)^2 + \frac{2\pi a}{\lambda}\frac{Eab^2}{4(1-v^2)}\left[ln\left(\frac{4a}{\rho_0}\right) - 1\right] \quad (21)$$

with a dislocation core cutoff radius ρ_0 [123]. Since $a^3 > a^2 \ln a$, a comparison between Eqs. (17) and (21) suggests that the misfit dislocation will be preferable at large inclusion sizes. We note that misfit dislocations appear in SPSFA at small inclusion sizes but only in HPSFA in very large sizes. This trend results from the fact that the hierarchical precipitate structure in HPSFA effectively reduces the misfit strain between the precipitate and the matrix, as indirectly supported by the steep decrease in the hardness during the aging treatments from 10 to 100 hours (Figure 41). Noting $a_{crt} \propto \gamma_0/\mu\varepsilon_m^2$, the critical size in HPSFA is much larger so that misfit dislocations appear in the later stage during the growth and coalescence of these precipitates.

Due to the presence of the interfacial dislocation, which releases the elastic strain, it is expected that the degree of the elastic strain for SPSFA is lower than that for HPSFA. Furthermore, the elastic strain at the semi-coherent interface seems to be relaxed on the further aging treatments by forming more interfacial dislocations [Figures 36 and 38]. Once the precipitate becomes larger in size [accompanied with the gradual decrease in the hardness of SPSFA (Figure 41)], the elastic strain will be further relaxed, which

reduces the elastic strain/interaction, thus, inducing the agglomeration of two neighboring precipitates and the disappearance of the alignment, as illustrated in Figure 40(e).

The coherent and hierarchically-structured precipitates of HPSFA are sustained until the aging times between 100 and 200 hours. Moreover, further aging to 100 hours induces the well-developed hierarchical structure [Figure 31(c)], as compared to the microstructure aged for 10 hours [Figures 31(a)-(b)]. As mentioned above, since the hierarchical structure is effective in retaining the coherent interface [Figure 40(d)], the spatial distributions (the alignment of the interface and close inter-precipitate-separation) can be retained. Further aging treatment to 500 hours leads to the agglomeration of the B2-NiAl phases within the $L2_1$-Ni_2TiAl precipitate, as illustrated in Figure 40(f). Once the primary precipitate loses the fine network hierarchy, the interfacial dislocations start to form to release the elastic-strain energy, which is similar to the case of SPSFA (Figure 38). After the loss of the hierarchical structure with the fine network and the coherency of the primary precipitate, the hardness behavior of HPSFA shows the modest decrease, as observed in that of SPSFA (Figure 41).

4.6 Summary

The microstructural formation and evolution of Fe-Ni-Al-Cr-Ti alloys with different amounts of Ti contents (2 or 4 weight percent, wt. %) were investigated during aging treatments at 973 K following the solution treatment at 1,473 K. The detailed microstructures were characterized, using transmission-electron microscopy (TEM), scanning-electron microscopy (SEM), and atom-probe tomography (APT). Moreover, Vickers-hardness tests were conducted to study the effect of the microstructural evolution

on the strengthening behavior of the materials. Both alloys consist of a single $L2_1$-Ni_2TiAl phase as a primary precipitate with the different morphology, sizes, and inter-phase structures in the solution-treated state. The 2-wt.-%-Ti alloy is composed of a coherent and cuboidal precipitate with an average edge length of 50 nm, and narrow anti-phase boundaries with an approximate width of ~ 10 nm are present inside the precipitate. In contrast, the addition of the 4-wt.-%-Ti content leads to a semi-coherent and irregular/polygonal-shaped precipitate with a size range of 130 ~ 160 nm, and the precipitate is observed to be decorated with misfit dislocations at the interfaces. In the subsequent aging treatments at 973 K, both alloys exhibit distinct microstructural evolutions in terms of the internal structure, interface structure, and spatial arrangements of the precipitates (the alignment of the interface and small inter-separation of the precipitates), which are closely associated with the coherency strain, and can be summarized as follows.

1. Fe-Ni-Al-Cr-Ti alloy with 4-wt.-% Ti

[Single-precipitate-strengthened ferritic alloy (SPSFA)]

- All the microstructures aged at 973 K only contain a semi-coherent single $L2_1$-Ni_2TiAl precipitate with a high density of misfit dislocations, and no B2-NiAl phase inside the $L2_1$-precipitate is observed (a single precipitate structure).
- During aging at 973 K, the primary $L2_1$ precipitates gradually coarsen and change their morphology from polygonal to spherical shapes.
- The spatial arrangements gradually disappear as the precipitates coarsen.

- The coarsening behavior of the precipitate leads to a gradual decrease in the hardness value.

2. Fe-Ni-Al-Cr-Ti alloy with 2-wt.-% Ti

[Hierarchical-precipitate-strengthened ferritic alloy (HPSFA)]

- The early stage of aging treatments (≤ 100 hours) establishes a fine network of a B2-NiAl phase along the anti-phase boundaries within the primary $L2_1$-Ni_2TiAl precipitate (a hierarchical precipitate structure).
- The hierarchical precipitate retains the coherent interfaces and the spatial arrangements, while inducing a steep decrease in the hardness value.
- Longer aging treatments (> 100 hours) lead to the disappearance of the hierarchical structure and coalescence of the B2 phase within the precipitate.
- The disappearance of the hierarchical structure is accompanied with the occurrence of the coalescence of the primary precipitates and transition from the coherent to semi-coherent interfaces.
- Once the precipitate becomes semi-coherent, the hardness evolution during the further aging treatment shows a decent decrease, as observed in the 4-wt.-%-Ti alloy.

In addition to the primary precipitates, ultra-fine secondary precipitates with an approximate size less than 10 nm are observed in the Fe matrix for both alloys. The fine dispersion and no coarsening characteristics of the secondary precipitate during the aging treatments reflect that the secondary precipitate forms during the cooling process and is dissolved to the Fe matrix at the aging temperature (973 K).

CHAPTER 5 IN-SITU NEUTRON-DIFFRACTION STUDIES AT ELEVATED TEMPERATURES

5.1 Introduction

In the previous chapters, it was shown that the creep resistance of the hierarchical-precipitate and single-precipitate-strengthened ferritic alloys is significantly improved, as compared to the NiAl-strengthened ferritic alloys [76]. For instance, the secondary creep rates of these alloys at 973 K are significantly reduced by more than four orders of magnitude, as compared to a NiAl-strengthened ferritic alloy [53] and conventional ferritic steels [6, 7, 22, 124]. Moreover, HPSFA shows much better creep resistance than SPSFA with a higher volume fraction of the precipitates [76]. It was suggested that the elastic-strain field in the matrix created by misfitting precipitates of HPSFA plays a critical role in enhancing the elastic interaction between the precipitate and mobile dislocations, and, hence, the creep resistance.

5.2 Objective

In the present chapter, we studied the effect of the precipitate structures, such as the size and interface structures (coherent and semi-coherent) of the precipitates, on the deformation mechanisms and mechanical properties of the hierarchical-precipitate and single-precipitate-strengthened ferritic alloys at high temperatures. Systematic investigations have been carried out, using in-situ neutron-diffraction experiments in combination with the crystal-plasticity finite-element method (CPFEM). The in-situ

neutron-diffraction technique has been extensively utilized to understand the governing deformation mechanisms of engineering materials, such as the evolution of elastic strains and interactions (load-sharing) between constitutive phases/intergranular grains [9, 125-128]. Using this technique, the dynamic evolution of the elastic strain of the constitutive phases during tensile deformation at 973 K was derived for the above-mentioned HPSFA and SPSFA. Furthermore, a stress-relaxation experiment on SPSFA was conducted to study the effect of the diffusional flow along the inter-phase boundary on the load-sharing behavior. Here, the stress-relaxation test refers to the test where a sample subjected to a load at high temperatures is being held at a fixed displacement. The results of the in-situ tension experiments are compared by crystal-plasticity finite-element simulations, which support the load transfer between the constitutive phases. These results demonstrate that the coherent interface with a high level of the elastic-strain field in the matrix of HPSFA plays an important role in enhancing the load-transfer and strain-hardening capability, and, thus, improving the mechanical properties of the materials at elevated temperatures.

5.3 Experimental and Modeling Methods

5.3.1 In-situ Tension Neutron-Diffraction at 973 K

The nominal compositions of the alloys are Fe-6.5Al-10Cr-10Ni-xTi-3.4Mo-0.25Zr-0.005B with x = 2 and 4 in weight percent (wt. %). A plate ingot of the 2-wt.-%-Ti alloy with a dimension of 12.7 × 25.4 × 1.9 cm^3 and a rod ingot of the 4-wt.-%-Ti alloy with 2 Kg and a diameter of 5.08 cm were prepared by the Sophisticated Alloys, Inc., using the vacuum-induction-melting facility. Hot isostatic pressing (HIP) was

applied to the ingots at 1,473 K and 100 MPa for 4 hours in order to reduce defects formed during the casting and cooling processes. These alloys were homogenized at 1,473 K for 30 minutes, followed by air cooling and, then, aged at 973 K for 100 hours. The thin foils for conventional transmission-electron-microscopy (CTEM) observations were prepared by electropolishing, followed by ion milling at the ion energy of ~ 2 kV and an incident angle of ± 6 degree. The TEM specimens were cooled by liquid N_2 during ion milling. The TEM observations were conducted with a Zeiss Libra 200 MC TEM/STEM. The TEM images were acquired at an acceleration voltage of 200 kV.

The in-situ tension neutron-diffraction (ND) experiments on the 2-wt.-%-Ti and 4-wt.-%-Ti alloys were carried out on the Spectrometer for MAterials Research at Temperature and Stress (SMARTS) diffractometer of the Los Alamos Neutron Science Center (LANSCE) facility located at the Los Alamos National Laboratory, United States [72], and ENGIN-X facility located at the ISIS, United Kingdom [129], respectively. The ND instrument utilizes time-of-flight (TOF) measurements, in which the incident beam is polychromatic with a range of wave lengths, which allows for the ND measurements with a diffraction pattern covering a wide range of d spacings without the rotation of samples or detectors. Two detectors, which are fixed at an angle of 45° to the loading direction, were employed to collect the diffracted beams from polycrystalline grains with lattice planes parallel to the transverse and axial directions, respectively. Therefore, the lattice parameters of differently-oriented grains and each of the phases can be measured simultaneously both parallel and perpendicular to the loading directions [54, 125]. Screw-threaded cylindrical samples with a gage diameter of 6.35 mm and a gage length of 40

mm were machined for the in-situ loading experiments at LANSCE, while ones with a gage diameter of 8 mm and a gage length of 42 mm at ENGIN-X. The ND measurements were conducted at room and elevated temperatures up to 973 K. The ND data for 2- and 4-wt.-%-Ti alloys were collected for about 12 and 20 minutes, respectively. The in-situ tension experiment at LANSCE was carried out in vacuum at 973 K, while that at ENGIN-X was conducted in air. In addition to the in-situ tension experiments, a stress-relaxation test on SPSFA at 973 K was carried out at ENGIN-X. The screw-threaded cylindrical sample was loaded to 150 MPa at 973 K and held in a displacement-holding mode for about 4 hours. The macroscopic strain was measured using a high-temperature extensometer over a gauge length of 10 mm within a measureable strain range of 10 %.

5.3.2 In-situ Creep Neutron-Diffraction Experiments at 973 K

The in-situ creep ND experiments were carried out on the Spectrometer for MAterials Research at Temperature and Stress (SMARTS) diffractometer of the Los Alamos Neutron Science Center (LANSCE) facility located at the Los Alamos National Laboratory [72]. Screw-threaded cylindrical samples with a gage diameter of 6.35 mm and a gage length of 40 mm were machined for the in-situ creep experiments. In-situ creep tests were performed in vacuum at 973 K under constant load levels. Before the in-situ creep test, the lattice parameter was measured at elevated temperatures. The samples were studied by ND at high temperatures after the sample saturated within ± 1 K of the target temperature, and the sample displacement was equilibrated. The ND data were collected for 15 minutes. After the ND measurement at 973 K, in-situ creep experiments were performed under constant load levels, and the macroscopic strain was measured,

using a high-temperature extensometer over a gauge length of 25 mm within a measureable strain range of 10 %. The sample was subjected to constant stress levels of 100, 150, 190, 220, and 235 MPa. After the stress was increased to 235 MPa, the sample fractured in one hour. The ND data were collected in 10-minute increments. The total creep strain to final rupture was about 9 %, which is within the measureable strain range of the extensometer used.

5.3.3 Neutron-Data Analysis

A representative ND pattern measured at room temperature without loading (a reference state, 5 MPa) is presented in Figure 42, with the refined profile by the GSAS-Rietveld analysis. Due to the structural similarity among constituent phases (α-Fe, B2, and $L2_1$ structures), the fundamental reflections (e.g., 110, 200, 211, 220, and 310 peaks) are expected to be overlapped with each other, as observed in Figure 42. Besides the fundamental reflection, low-intensity superlattice reflections (e. g., 200, 222, and 420 peaks) are also observed, which are common to both B2 and $L2_1$ structures. However, the superlattice reflections exclusively unique to the $L2_1$ structure (111 and 311 peaks) are hardly observed, and this trend is believed to result from the limited intensity of the neutron.

Our ND analysis was conducted under an assumption that the diffraction intensity from the precipitate mainly originates from the $L2_1$-structure phase, and one from the low volume fraction of the B2-structure phase does not appreciably contribute to the diffraction intensity. The lattice parameters of the Fe and $L2_1$ phases were determined from a whole-pattern Rietveld refinement employing the GSAS program developed at the

Los Alamos National Laboratory [75]. The ND data during the heating and entire in-situ loading experiments can be successfully refined with the value of χ^2, fitting accuracy, ranging from 1 to 2, which gives a confidence on our analysis.

The averaged phase strain represents the volume-averaged lattice strain of the individual phases (α-Fe and Ni_2TiAl), which depends on the elastic and plastic anisotropy of the individual phases. The average phase strain is calculated, using Equation (1) [$\varepsilon = (a - a_0)/a_0$], where a is the lattice parameter of a given phase measured during heating and/or loading, and a_0 is the corresponding lattice parameter before loading (5 MPa at 973 K).

5.3.4 Finite-Element Crystal-Plasticity Model

The microstructure-based finite-element simulations use the crystal-plasticity model, which is implemented as a user material subroutine in the commercial software ABAQUS [130]. The constitutive relationship used in the simulations was defined through the Peirce-Asaro-Needleman power law, which relates the slip rate and the resolved shear stress on a given slip system by,

$$\dot{\gamma}^{(\alpha)} = \dot{\gamma}_0 \left| \frac{\tau^{(\alpha)}}{\tau^{(\alpha)}_{flow}} \right|^n sgn(\tau^{(\alpha)}) \tag{22}$$

The flow stress increases as a function of the cumulative slip strains,

$$\dot{\tau}^{(\alpha)}_{\text{flow}} = \sum_\beta h_{\alpha\beta} |\dot{\gamma}^{(\beta)}| \text{ where } h_{\alpha\beta} = h(\gamma)[q + (1-q)\delta_{\alpha\beta}], \text{ when } \alpha \neq \beta$$

However, for the self-hardening model, we use,

$$h_{\alpha\alpha} = h(\gamma)\, h_0 \,\text{sech}^2 \left| \frac{h_0 \gamma}{\tau_s - \tau_0} \right| \tag{23}$$

where h_0 is the initial hardening modulus, τ_0 is the initial slip strength, and τ_s is the saturated slip strength. $\dot{\gamma}_0^{(\alpha)}$ is the characteristic strain rate, n is the stress component, and $h_{\alpha\beta}$ is the latent hardening moduli. The terms, $\tau^{(\alpha)}$ and $\tau_{\text{flow}}^{(\alpha)}$, are the resolved shear stress and flow strength of the α-th slip system, respectively, and q is the latent-hardening coefficient in the same set of slip systems.

For the 2-wt.-%-Ti alloy with the hierarchical precipitate consisting of the B2 and $L2_1$ phases, a cubic model with $15 \times 15 \times 15$ elements was set up [Figure 43(a)], and divided into 125 grains with each of 27 elements making up a $3 \times 3 \times 3$ cubic grain. The 5 elements were randomly-selected and assumed to be the $L2_1$ precipitates in each grain. The volume fraction of the $L2_1$ precipitates, compared to the Fe matrix, was initially set to be 18.5 %. A second type of B2 precipitates was introduced with an element smaller in size embedded in the pre-existing $L2_1$ elements in each grain, as shown in Figure 43(b). The B2 elements were set to have a volume fraction of 50 %, compared to $L2_1$ elements, and 9.25 %, relative to the Fe matrix. In essence, each 27-element grain contains a total of 22 elements assigned to the Fe matrix crystal-plasticity parameters. Each of the remaining 5 elements contains 6 trapezoidal elements at the 6 faces of the cubic element with a smaller cubic elements attached at the center of these 5 elements. The trapezoidal elements were assumed to have the $L2_1$-precipitate properties, and the smaller cubic elements were assumed to have B2-precipitate properties. For the 4-wt.-%-Ti alloy with the single $L2_1$ precipitate, a total of 125 $(3 \times 3 \times 3)$ randomly-oriented cubic grains were used in the model. Each grain consists of 27 elements, and 6 of them were assigned to be $L2_1$-type precipitate.

The values of elastic constants (C_{11}, C_{12}, and C_{44}) of the Fe matrix, $L2_1$, and B2 phases at 973 K from References [55, 76] were initially employed, and further adjusted by comparing with experimental diffraction elastic constants. Precipitate elements were set to deform elastically, and, hence, the elastic constants of the precipitate are considered as only variables in the modeling parameters. Other parameters, such as h_0, τ_s, and τ_0, for the Fe matrix, which determine the plastic-deformation behavior, are only tuned so that the modelled stress vs. elastic phase-strain curves follow the experimental results. It is known that the slip strength (τ_0) is related to the macroscopic yield strength of a polycrystal by the Taylor factor, which is about 3 for a bcc material.

5.4 Results

5.4.1 In-situ Tension Neutron-Diffraction Experiments at 973 K

The transmission-electron microscopy (TEM) microstructures of the 4-wt.-%- and 2-wt.-%-Ti alloys aged at 973 K for 100 hours are displayed in Figure 44. The insets in Figures 44(a) and (b) exhibit the selected-area diffraction pattern of [101] and [100] zone axes, respectively. The [101] zone axis contains two types of super-lattice reflections; the (111) and (131)-type reflections are unique to the $L2_1$ structure, while (222) and (020)-type reflections are common to the $L2_1$ and B2 structure. By using the two-type of the super-lattice reflections to form dark-field (DF) TEM images, the B2 and $L2_1$ structures within the precipitate can be identified [60]. However, the [100] zone axis is only composed of a single-type of a superlattice reflection. With the coexistence of the B2 and $L2_1$ phases, the superlattice reflections of $(002)_{B2}$ and $(004)_{L21}$ are overlapped.

When imaging the overlapped $(001)_{B2}/(002)_{L21}$ reflections, the difference in the structural factor between the B2 and $L2_1$ structures gives rise to the image contrast in DF-TEM images [60], as observed in Figure 44(b). Since the $L2_1$-Ni_2TiAl phase has the lower structural factor than that of the B2-NiAl phase [60], the bright zones are the B2-NiAl phases, whereas the dark zones are the $L2_1$-Ni_2TiAl phases. Based on this DF-TEM image identification, the 2-wt.-%-Ti alloy consists of the parent $L2_1$ precipitate strengthened by the B2-NiAl zones (hierarchical precipitate-strengthened ferritic alloy; HPSFA), while the 4-wt.-%-Ti alloy is reinforced by the single $L2_1$-Ni_2TiAl precipitate in the Fe matrix (single precipitate-strengthened ferritic alloy; SPSFA). Both alloys often contain a small Fe inclusion within the precipitates, which was previously determined by energy-dispersive X-ray spectroscopy [76].

The precipitates in HPSFA and SPSFA show apparent microstructural differences in terms of the size, morphology, and interface structure of the precipitates in Figure 44. The single $L2_1$-type precipitate in SPSFA with an average size of 220 ± 46 nm [76] is decorated with a high density of interfacial (misfit) dislocations, which indicates the high level of the lattice mismatch between the Fe and $L2_1$ phases. The misfit dislocations are formed to release the elastic strain of the precipitate, which result in a change from cuboidal to spherical shapes. That is, with the elastic-strain energy being dominant, the precipitate shape tends to take a form that resembles the elastic stiffness anisotropy – being cuboidal in cubic crystals. In contrast, the hierarchical precipitate with an average width of 111 ± 27 nm [76] is free of the interfacial dislocation, which reflects the coherent interface, resulting from the relatively-small lattice mismatch between the

matrix and precipitate, as compared to that of SPSFA. Moreover, the cuboidal morphology of the hierarchical precipitate indicates the high level of the elastic strain of the precipitate. Based on the precipitate features, such as the morphology of the precipitates and coherent/semi-coherent interfaces in HPSFA and SPSFA, it is believed that the magnitude of the elastic-strain field in the matrix of HPSFA is greater than that of SPSFA.

Representative neutron-diffraction (ND) patterns measured at room temperature without loading (a reference state, 5 MPa) for SPSFA and HPSFA are presented in Figure 42, with the refined profile by the GSAS Rietveld analysis [75]. Both alloys show the fundamental reflections (110, 200, 211, and 220), and super-lattice reflections (111, 200, 222, and 420). The superlattice peaks of (111) and (222) are unique to the $L2_1$ structure, as compared to the B2 structure, which supports the formation of the $L2_1$ structure in both alloys. The enlarged patterns in the insets of Figures 42(a) and (b) clearly show the well-separated fundamental $110_{Fe}/220_{L21}$ peaks for SPSFA and overlapped peaks for HPSFA, respectively. This trend supports the TEM observation indicating that the lattice misfit between the α-Fe and $L2_1$ phases of SPSFA is greater than that of HPSFA. The averaged lattice parameters of the α-Fe and $L2_1$ phases, determined by the GSAS Rietveld analysis [75], and corresponding lattice misfit, defined as Eq. [8], for SPSFA and HPSFA at room temperature and 973 K are summarized in Table 12. As can be seen, the lattice misfit of SPSFA (1.32 %) is greater than that of HPSFA (0.77 %) at 973 K, and the larger lattice misfit causes the formation of the misfit dislocations at the interface between the Fe matrix and $L2_1$ precipitate for SPSFA [Figure 44(a)]. In contrast, the lower lattice misfit

of HPSFA leads to the retention of the coherent interface, as reflected by the TEM observations in Figure 44.

Figures 45(a) and (b) show the macroscopic stress versus strain curves for in-situ tension loading experiments on SPSFA and HPSFA at 973 K, respectively. The creep strain during the load-holding period is not significant when the stress is less than the macroscopic yield strength. Since the extensive creep strain occurs at stresses close to or higher than the yield strength [55], the displacement-holding mode was used to measure the ND data at the higher stresses. During yielding, both alloys exhibit a short hardening stage, and the hardening behavior of HPSFA seems to be more significant than that of SPSFA. The 0.2 % macroscopic yield strengths for SPSFA and HPSFA were estimated to be about 200 MPa and 230 MPa, respectively. Once the applied stress reaches the highest level (ultimate tensile stress; UTS), the stress softening, where the stress gradually decreases with increasing the plastic strain, occurs for both alloys. During the ND measurements in the plastic regimes (displacement holding), a decrease in the applied stress is observed (stress relaxation), and the amount of the stress decay seems to depend on the tested alloys.

Figure 46 shows the temporal evolution of the applied stress in the plastic deformation region where the ND measurements were carried out with the displacement holding mode. The averaged stress was estimated during each displacement-holding step, and marked as red squares in Figures 46(a) and (b). Note that the holding time (about 20 mins) of SPSFA for the ND measurements is longer than that of HPSFA (about 12 mins). This is because the holding time was required to obtain the statistically-reliable ND data

in each ND instrument. Figures 46(c) and (d) show the temporal evolution of the relative stress decay with different plastic strains. It can be seen that the total amount of the stress decay in each alloy is independent of the plastic strains considered. The stress-relaxation curve can be divided into three regimes, initial rapid decline, transition, and asymptotic regions, as observed in the stress-relaxation experiments at high temperatures [131, 132]. Figures 46(c) and (d) provide the insight into the efficiency of the stress relaxation varying with the tested alloys. For example, the total stress decay of SPSFA is greater than that of HPSFA. The magnitude of the stress decay of SPSFA for 700 seconds is about 70 MPa, which is about 20 MPa higher than that of HPSFA, as indicated by blue arrows in Figures 46(c) and (d). In addition, the residual stress ratio is introduced to characterize the stress relaxation resistance and relaxation efficiency. The residual stress ratio (ψ) is defined as follows [133],

$$\psi = \frac{\sigma}{\sigma_0} \tag{24}$$

where σ_0 and σ are the initial stress and residual stress at a certain time, respectively. The stress residual ratios of HPSFA and SPSFA are calculated using Eq. (24) and are 79.7 ± 0.3 % and 61.0 ± 3.6 % at 973 K, respectively. This trend suggests that the stress relaxation occurs more easily for SPSFA at 973 K, as compared to HPSFA.

The evolution of the average-phase elastic-strains of the matrix and precipitate as a function of average stress at 973 K are displayed in Figure 47. Note that the average stress estimated during each displacement-holding step in Figures 46(a) and (b) is employed in the curves. Similar to the macroscopic stress-strain curves, the elastic strain evolution for both alloys exhibits the two regimes; elastic and plastic regimes.

Specifically, the elastic region is characterized by the linear slope of the lattice strain with respective to the average stress. The onset of the plastic deformation is marked by the deviation from the linear response on the elastic strain-stress curves. For example, the slope of the elastic strain of the matrix is increased, relative to the linear-elastic response, which indicates that the matrix cannot assume the further elastic strain and begins to plastically deform [134]. Therefore, the yielding of the matrix leads to the plastic strain besides the elastic strain. In contrast, the reduced slope of the elastic strain of the precipitate reflects that the precipitate is still deforming elastically, and the additional plastic strain from the matrix is transferred to the precipitate [128], which induces the decrease in the slope of the elastic strain of the precipitate. The microscopic yielding occurs around the average stress of 150 MPa for SPSFA and 180 MPa for HPSFA, respectively. After the matrix is yielded, the elastic strain of the precipitate increases with the average stress. The maximum elastic strain of the precipitate of HPSFA (about 5,000 με) is greater than that of SPSFA (about 3,500 με), which indicates the effectiveness of the load carrying capability of the precipitate in HPSFA than SPSFA. However, once the average stress reaches the maximum value, the elastic strain of the precipitate for both alloys remains fairly unchanged, while that of the matrix gradually decreases. This feature corresponds to the softening behavior in macroscopic strain-stress curves (Figure 45), where the applied stress slightly decreases with increasing the plastic strain.

The evolution of the averaged elastic phase strain as a function of stress was simulated using crystal-plasticity finite-element modelling (CP-FEM) for SPSFA and HPSFA. Figure 48 shows the FEM results with the experimental measurements during

the in-situ loading tests at 973 K. The dashed lines in Figure 48 are the predictions, while the symbols are the experimental data. Note that both predicted and experimental data are the averaged phase strain determined from the Rietveld analysis. The FEM results are qualitatively consistent with the experimental data in terms of the elastic-plastic transition and subsequent load transfer from the matrix to precipitate. Specifically, once the matrix is yielded, the elastic strain of the matrix is saturated, and the additional load from the matrix is transferred to the precipitate, leading to the observed splitting of the lattice strain curves. For HPSFA, the modeled evolution of the elastic strain for the B2 and $L2_1$ phases within the precipitate is comparable to each other, and the B2 and $L2_1$ phases assume the additional load from the plastically deforming matrix, which is similar to the evolution of the single $L2_1$ precipitate in SPSFA. It seems that such a hierarchical structure within the precipitate has no considerable influence in terms of the microscopic load-transfer behavior. The strain hardening of HPSFA is observed to be more pronounced than that of SPSFA, as supported by the hardening parameters (h_0; 500 for HPSFA, and 100 for SPSFA) employed in the FEM simulations (Table 13). The hardening parameter is related to the strain-hardening capability of the matrix according to Eq. (23), which indicates that the HPSFA has more strain-hardening capability of the matrix, as compared to SPSFA.

The simulated elastic strain of the matrix and precipitate continue to increase with the applied stress in Figures 48(a) and (b), which is not consistent with the experimental results. This is because the strain-softening occurs at 973 K after the applied stress reaches UTS (Figure 45). Figures 48(c) and (d) show the simulated and

experimental evolution of the elastic strain as a function of plastic strain. The simulated evolution tends to show the strain-hardening behavior, as the plastic strain increases, while the experimental elastic-strain evolution remains fairly constant after the plastic strain of about 1.0 %. This discrepancy is believed to result from the diffusional process, such as the dislocation and diffusional creep, which is not considered in the FEM simulations, and will be discussed in Section 5.4.2 Stress-Relaxation Behavior at High Temperatures.

5.4.2 In-situ Creep Neutron-Diffraction Experiments at 973 K

- **Lattice-parameter evolution during heating**

The lattice parameters of the α-Fe and Ni_2TiAl phases at room and elevated temperatures up to 973 K were determined using the Rietveld refinement, as shown in Figure 49(a). Note that the lattice parameter of the $L2_1$ structure is about 2 times larger than that of the B2 structure, since the $L2_1$ structure consists of eight sub-lattices of a B2 structure [62]. The lattice parameters of the α-Fe and Ni_2TiAl phases at room temperature are 2.88941 Å and 5.82247 Å, respectively. Figure 49(a) shows that the lattice parameters for both phases gradually increase with temperature, as expected. The thermal strain of each phase was calculated using Eq. (1), and was plotted in Figure 49(b). The slope of the thermal strain curve vs. temperature is indicative of the coefficient of thermal expansion (CTE), and the calculated values of the linear CTE are 1.32×10^{-5} K^{-1} for α-Fe and 1.59×10^{-5} K^{-1} for Ni_2TiAl, respectively. The lattice misfit between the α-Fe and Ni_2TiAl phases was calculated using Eq. (2), and summarized in Table 14. The lattice misfit between two phases gradually increases from 0.7 % at room temperature to 0.9 % at 973 K. The

gradual increase of the lattice misfit is associated with the higher value of CTE of the Ni_2TiAl phase than that of α-Fe phase.

- **Mechanical-creep data**

Figure 50(a) exhibits the macroscopic creep strain as a function of time for step-loading creep experiments, and the applied stress levels were marked in the curve. However, based on the tension creep rupture results in Figure 20, the current alloy exhibits the well-defined and prolonged secondary creep regime, and, thus, the 100 and 150 MPa can be expected to be in the primary creep state. The strain-rate evolution at 190, 220, and 235 MPa is presented in Figure 50(b). Once the load was raised to 190 MPa, the deformation reaches the well-defined steady-state creep regime after 3 hours of the primary region. At the applied stress of 220 MPa, the short primary and secondary regions are observed, followed by the extended tertiary creep, as marked by a gradual increase in the strain rate, relative to the minimum strain rate.

- **Averaged lattice-strain evolution during the in-situ creep/tension experiments at 973 K**

The temporal evolution of average phase strains for α-Fe and Ni_2TiAl phases calculated using Eq. (1) in the axial and transverse directions is presented in Figure 51. Note that the creep deformation at 100 and 150 MPa is in the primary regime. Once the applied stress increases to 100 MPa in Figure 51(a), the axial strains of α-Fe and Ni_2TiAl phases are raised up to 670 με and 790 με, respectively, and seem to remain approximately constant at 100 MPa. Similarly, transverse strains of α-Fe and Ni_2TiAl phases upon the loading shift to - 220 με and - 390 με, respectively, and keep fairly

unchanged at 100 MPa. Similar phase-strain evolution during primary and secondary creep regimes has been reported in a NiAl-hardened ferritic alloy [54]. The diffraction elastic moduli ($E_{phase} = \sigma_{applied}/\varepsilon_{phase}$, where $\sigma_{applied}$ is the applied stress, and ε_{phase} is the average phase-lattice strain) of the individual-constrained phases are approximately estimated to be 149.2 GPa for the matrix and 126.5 GPa for the precipitate, respectively, using instantaneous lattice strains upon loading to 100 MPa, and these values will be used to calculate average phase stress of the matrix and precipitate during the entire creep ($\sigma_{applied} = E_{phase/matrix} \times \varepsilon_{phase}$). The average stresses of both phases remain constant close to the applied stress of 100 MPa. A further increase of the applied stress up to 150 MPa exhibits the similar trend, as observed at 100 MPa in Figure 51(a). The diffraction elastic moduli during loading to 150 MPa are more or less identical to that during loading to 100 MPa. This trend indicates that both phases are in the elastic regime, which is consistent with the macroscopic elastic response. Moreover, the average stresses of both phases during the creep remain fairly constant close to the applied stress of 150 MPa.

The lattice-strain evolution at 190 MPa is presented in Figure 51(b) with the corresponding strain-rate curve, which reflects that the deformation is mainly in secondary creep regime. Similar to 100 and 150 MPa, the transverse strains of α-Fe and Ni_2TiAl remain constant at 190 MPa. Interestingly, however, the axial strain of the precipitate apparently increases from 1,800 με to 2,140 με (an increase by 340 με), whereas that of the matrix slightly reduces from 1,180 με to 1,140 με (a reduction by 40 με). Note that an increase in the true stress (0.5 MPa) during the creep at 190 MPa is not too significant to induce such an increase in the lattice strain of the Ni_2TiAl precipitate.

Indeed, a 0.5-MPa increase in the true stress only amounts to a lattice strain of less than 10 με in Ni_2TiAl phase. The calculated average stresses are 183 MPa for the α-Fe phase and 228 MPa for the Ni_2TiAl phase at the true stress of 190.7 MPa, which corresponds to the creep time of 405 min and become 170 MPa and 270 MPa at the true stress of 191.2 MPa, corresponding to the creep time of 1,358 min. The average stress of the precipitate (228 MPa) is quite greater than the applied stress (190 MPa), indicating that the larger proportion of the load is subjected to the precipitate during loading from 150 to 190 MPa. Moreover, the gradual increase in the average stress of the precipitate (228 to 270 MPa) with time supports a load transfer to the precipitate during the creep. Similar phase strain evolution is observed during creep at 220 and 235 MPa, as presented in Figure 51(c). The lattice strain of the Ni_2TiAl phase in both the axial and transverse directions continues to increase with increasing the time, as observed at the applied stress of 190 MPa. The average stresses are 172 MPa (1,178 με) and 366 MPa (2,894 με) for the α-Fe and Ni_2TiAl phases at the beginning of the creep of 220 MPa, respectively. Moreover, the average stress of the precipitate significantly increases up to 450 MPa (3,562 με) at the end of 220 MPa-creep, relative to 366 MPa at the start of 220 MPa-creep. These elastic-strain evolutions at stresses higher than 190 MPa provide a strong evidence for the occurrence of the load transfer from the matrix to precipitate during creep. Interestingly, in addition to the increase of the Ni_2TiAl strain, the strain of the α-Fe phase in both directions gradually decrease from 1,178 με to 820 με (a decrease by 358 με) with increasing time. This strain decrease of the matrix phase corresponds to 50 MPa of the average stress (from 172 MPa to 122 MPa).

Figure 52 exhibits the constrained lattice misfit between α-Fe and Ni_2TiAl phases as a function of macroscopic strain along the axial and transverse directions during the entire step-loading creep tests at 973 K. At stresses below 150 MPa, lattice misfits along the axial and transverse directions remain almost unchanged with an averaged value of 0.00941 and 0.00854, respectively. However, at 190 MPa, the axial misfit gradually increases from 0.00982 to 0.01007 corresponding to the macroscopic strains of 0.23 % and 0.48 %, respectively, whereas the transverse misfit remains constant with an average value of 0.00843. Furthermore, the lattice misfit for both directions at 220 and 235 MPa exhibits an apparent increase up to 0.012 and decrease down to 0.006 for axial and transverse directions, respectively, as the creep deformation proceeds. This lattice-misfit evolution also supports the accumulation of the internal stress between the matrix and the precipitate at stresses higher than 190 MPa.

- **Temporal evolution of (hkl) plane-specific strain during the in-situ creep/tension experiments at 973 K**

The (hkl) plane-specific strain for differently-orientated grains to the axial direction during the in-situ creep experiment is presented in Figure 53. Below 190 MPa, all the (hkl) strains remain fairly constant regardless of creep deformation regions (primary and secondary creep regimes). There is no clear load transfer between the differently-orientated grains during the creep process. It has been observed that the (200) and (310) plane-specific lattice strains gradually increase in the primary creep regime, followed by constant evolution during the secondary and tertiary regimes for the NiAl-strengthened alloy [54]. It was explained by the fact that (200) and (310) grains pick up

the additional load arising from neighboring creeping grains [54]. However, (200) and (310) specific-plane strains are observed to remain constant during the primary and secondary creep regimes at 100, 150, and 190 MPa in the present study. This trend implies that during the creep deformation (primary and secondary regimes), a load transfer between the differently-orientated grains hardly occurs. Instead of the load transfer (gradual increase of the plane strains), a steady decrease in the all the (hkl) strains starts to occur at 220 MPa, which is in the secondary and tertiary regimes, as observed in Figure 53(b).

5.5 Discussions

5.5.1 Tensile-Deformation Mechanism at 973 K

The 2-wt.-%-Ti alloy is reinforced by the coherent precipitate with the hierarchical structure of the B2 and $L2_1$ phases. The estimated macroscopic yield strength of HPSFA at 973 K is about 230 MPa, which is higher than that (200 MPa) of the 4-wt.-%-Ti alloy strengthened by the semi-coherent single $L2_1$ precipitate. It is well known that the yield strength for coherent precipitate-reinforced materials is controlled by shearing or Orowan-dislocation-bypass mechanisms [92, 135]. It has been reported that the operational mechanisms are strongly dependent upon the size of the coherent/shearable precipitate [96, 136]. In general, the shearing mechanism is dominant when the precipitate is smaller than a critical size of the precipitate, while the Orowan-dislocation-bypass mechanism is operational at the larger size. The shearing mechanism involves

three strengthening contributions, such as, ordering strengthening ($\Delta\sigma_1$), coherency strengthening ($\Delta\sigma_2$), and modulus mismatch strengthening ($\Delta\sigma_3$) [137], and defined as,

$$\Delta\sigma_1 = 0.81M\frac{\gamma_{APB}}{2b}\ln\left(\frac{3\pi f}{8}\right)^{1/2} \quad (25)$$

$$\Delta\sigma_2 = M\alpha_\varepsilon(G\delta)^{3/2}\left(\frac{rf}{0.18Gb^2}\right)^{1/2} \quad (26)$$

$$\Delta\sigma_3 = 0.0055M(\Delta G)^{3/2}\left(\frac{2f}{Gb^2}\right)^{1/2} b\left(\frac{r}{b}\right)^{\frac{3m}{2}-1} \quad (27)$$

where M = 2.9 is the mean orientation factor for a bcc matrix [138], b = 0.250 nm is the magnitude of the matrix Burgers vector, determined by the current ND results, f is the volume fraction of the precipitates, G = 57.0 GPa is the shear modulus of polycrystalline α-Fe at 973 K [139], α_ε = 2.6 is a constant [137], δ is the constrained lattice parameter mismatch, r is the mean precipitate radius, m is a constant taken to be 0.85 [137], and ΔG is the shear modulus mismatch between the matrix and the precipitates. The strength increase from the shear mechanism ($\Delta\sigma_1$, $\Delta\sigma_2$, and $\Delta\sigma_3$) is mainly influenced by the anti-phase boundary (APB) energy and size and volume fraction of the coherent precipitate.

Assuming the presence of a coherent single-$L2_1$-precipitate, the dependence of the strength increase on the precipitate size has been evaluated, using Eqs. (25) – (27), as shown in Figure 54, based on APB energy (γ_{APB} = 0.058 J/m^2) of the $L2_1$-Ni_2TiAl for the (110) plane [140], ΔG = 22.0 GPa, which is determined by the elastic constants of the FEM modeling in Table 13, and δ = 0.0077 for HPSFA at 973 K, determined from the current ND experiments (Table 12). As can be seen, the strength increase from the shearing contributions increases with increasing the size of the precipitate. The strength increase of the shearing contributions from the current calculation is expected to be

under-estimated, since the precipitate of HPSFA is a two-phase coupled-structure of the B2 and $L2_1$. Furthermore, the APB energy of the B2 for the (110) plane is 0.5 J/m^2 [140], which is higher than that of the $L2_1$ phase. Therefore, the actual strength-increase curve of the shearing mechanism is believed to be higher than the calculated curve, which is much greater than the experimental value of the yield strengths of HPSFA and SPSFA. These trends indicate that the precipitate shearing is unlikely to happen in the current alloys.

Another feasible mechanism is the Orowan-dislocation-bypass mechanism [141, 142], which is defined as

$$\sigma_{OR} = \frac{0.81G\boldsymbol{b}}{\pi\lambda_s(1-v)^{1/2}} \ln\left(\frac{1.63r}{\boldsymbol{b}}\right) \tag{28}$$

$$\lambda_s = 0.82 \times \left[\left(\frac{\pi}{f}\right)^{1/2} - 2\right] r \tag{29}$$

where λ_s is the square lattice spacing, and v = 0.3 is the Poisson's ratio. Based on the volume fractions of the precipitate for the studied alloys (f = 16 % for HPSFA and 22 % for SPSFA [76]), two curves of the Orowan-strength contribution with respective to the precipitate size were calculated using Eqs. (28) – (29) and also included in Figure 54. Good agreement is observed between the experimental and theoretical values. Generally, in Orowan-bowing mechanism, dislocations pass through the inter-particle region, and dislocation loops are created around precipitates. It can be inferred that the observed increase of the precipitate strain in Figure 47 is caused by the dislocation array around the precipitates, which accommodate the lattice misfit between the matrix and precipitate.

Therefore, it is concluded that the Orowan dislocation bypass is the dominant mechanism for HPSFA and SPSFA at 973 K.

5.5.2 Stress-Relaxation Behavior at High Temperatures

The evolution of the elastic strain of constitutive phases in HPSFA and SPSFA shows the qualitative agreement with the macroscopic stress-strain behavior, and can provide an in-depth understanding of the deformation mechanisms of the current alloys at high temperatures. The beginning of the load transfer from the matrix to precipitate is indicative of the onset of the macroscopic yielding behavior. The strain-hardening behavior is also accompanied by the increase in elastic strain of (or the load carried by) the precipitate, which reflects the significance of the load-transfer effectiveness of the precipitate on the mechanical properties of the current alloys at high temperatures. Furthermore, HPSFA with the coherent precipitate shows the greater load-transfer capability, such as the maximum value of the elastic strain of the precipitates, and strain-hardening capability of the matrix, than SPSFA with the semi-coherent precipitate. Therefore, the interface structures of the precipitates are believed to play a critical role in improving the load-transfer capability, and, thus, the mechanical properties at high temperatures.

During the ND data measurement at 973 K, a certain amount of stress relaxation occurs for both alloys. The stress relaxation at high temperatures has been studied to understand deformation mechanisms at high temperatures, such as creep mechanisms [131, 132]. The kinetics of this stress relaxation is known to be largely governed by dislocation processes and possibly grain-boundary sliding in materials [131]. In the

present alloys, the grain sizes of HPSFA and SPSFA are estimated to be larger than 200 μm, and, thus, the stress relaxation caused by the grain-boundary sliding is not expected to be significant. Instead, the phase interface between the matrix and precipitate could play an important role in the stress relaxation, and, hence, the load transfer between the constitutive phases at high temperatures. To verify this hypothesis, we conducted a stress-relaxation test on SPSFA at 973 K. The sample was loaded to 150 MPa at 973 K and held in a displacement-holding mode for about 4 hours. The ND data was collected in every 20 mins, and the ND data was analyzed, using the Rietveld whole-peak fitting using the GSAS program developed at the Los Alamos National Laboratory [75] to obtain the averaged lattice parameters of the Fe and $L2_1$ phases. The temporal evolution of the stress relaxation and the elastic strain at 973 K for SPSFA are displayed in Figure 55.

As observed in Figure 46, the macroscopic stress-relaxation curve in Figure 55(a) exhibits the logarithmic decay of the stress. The stress decreases from 150 MPa to 80 MPa, as the relaxation time increases. Similarly, the evolution of the elastic strain of the precipitate is well consistent with that of the macroscopic stress relaxation, while the elastic strain of the matrix shows the slight decrease. Due to the huge grain size, the slight decreases of the Fe matrix lattice strain with increasing the relaxation time is not expected to result from the grain-boundary sliding or diffusion, at the given relatively-low homologous temperature and high stresses. The decrease of the Fe matrix strain may be due to a combination of dislocation and diffusional creep [76]. More importantly, as the relaxation time increases, the elastic strain of the precipitate is rapidly reduced, and becomes comparable to that of the Fe matrix until there is no load transferred to the

precipitate from the plastically-deforming matrix. These results strongly support that the elastic strain of the precipitate, or equivalently the load transferred to the precipitate, is released by the diffusional process along the interface between the matrix and precipitate. It can be inferred that dislocations are pinned around the precipitates (such as Orowan-dislocation loops), which accommodates the lattice misfit created by plastic-elastic strain anisotropy between the matrix and precipitate. During the holding period, the pinned dislocations can be annihilated via the diffusional flow or bypass the precipitate via the dislocation-climb mechanism. It has been reported that the deformation of the initial and transitional regimes of the stress relaxation is dominated by the dislocation climb bypassing mechanism [132]. Therefore, in the current study, it is believed that the stress relaxation is mainly affected by the diffusional process (annihilation or bypass of dislocations) along the interface between the matrix and precipitate.

The efficiency of the load transfer from the matrix and precipitate as a function of temperature has been investigated, using in-situ ND experiments for the NiAl-strengthened ferritic alloy [55]. It was reported that at 973 K, no load transfer was observed between the Fe matrix and NiAl precipitate. It was explained by the fact that at 973 K, diffusional flows along the matrix–precipitate interface can relax the interphase strain, leading to the ineffective load transfer from the matrix to the precipitate phases. Moreover, it was reported that the coherency strain in the Fe matrix of HPSFA, caused by the lattice mismatch between the matrix and precipitate, plays an important role in enhancing the interaction between the precipitate and mobile dislocations at high temperatures. Hence, it is believed that the coherency strain improves the creep resistance

of HPSFA [95, 96, 143]. In contrast, the precipitate in SPSFA contains a high density of misfit dislocations that can reduce the elastic strain in the Fe matrix. The misfit dislocations, which could allow the pipe diffusion and the reduced strain in the Fe matrix, can reduce the interaction between the precipitate and dislocations at high temperatures. Similarly, in the current study, the coherent hierarchical precipitate of HPSFA with a lattice misfit of 0.77 % exhibits the more pronounced load-transfer and strain-hardening capability than the semi-coherent single precipitate of SPSFA, which reflects the effectiveness of the coherent precipitate with the high elastic strain. The coherency strain field in the Fe matrix created by the lattice misfit between the matrix and precipitate could be effective in enhancing the matrix-hardening capability via the strong interaction between the precipitate and mobile dislocations, and, thus, the strain-hardening and strengthening behavior of HPSFA at high temperatures. Therefore, it is suggested that the coherent precipitate with the high level of the misfit strain of HPSFA is effective in improving the load transfer from the matrix to the precipitate at 973 K, and, thus, the mechanical properties at high temperatures.

5.5.3 Load Transfer

As a comparison, our earlier work investigated the evolution of interphase and intergranular lattice strains of FBB8 during in-situ tension and creep experiments up to 973 K, using ND [54, 55]. In this case, no clear load transfer from the matrix to the B2 precipitate was observed, owing to the diffusional flow along the matrix-precipitate interface [144], which leads to the ineffective load transfer [55]. Thus, the B2 precipitate alone was not an effective reinforcing media at elevated temperatures. The ND results in

the present study demonstrate that the hierarchical NiAl/Ni_2TiAl precipitates can effectively assume the load from the Fe matrix during loading and creep deformation (Figure 56), which indicates that the diffusional flow along the matrix-precipitate interface is less significant in HPSFA, relative to the FBB8, resulting in the superior creep resistance of HPSFA. Besides dislocation climb and glide, the high-temperature deformation can occur via by the diffusional flow accommodated by grain boundary sliding, this latter mechanism depending on grain size [145-149]. Because the grain size of the present HPSFA is large (estimated > 200 μm), the grain-boundary sliding and diffusional flow are not expected to be dominant, as compared to the dislocation creep, especially given the relatively low homologous temperature and high stresses. However, we cannot exclude that slight decreases of the Fe matrix lattice strain with increasing creep time at 190 MPa (Figure 51) may be due to a combination of dislocation and diffusional creep. Future experiments where the grain size is changed systematically (e.g., by grain growth during homogenization) will be able to shed light on this issue.

5.5.4 Comparison between CP-FEM and Experimental Results

The lattice strain versus stress relationship Figure 56 provides key features in understanding the governing deformation mechanisms. Qualitatively, the splitting of lattice strains (Figure 56) indicates load sharing between the hard and soft material phases [150]. To investigate this load transfer further, a microstructure-based finite-element crystal-plasticity model was employed [130]. Details of the hardening law and other constitutive parameters can be found in the Table 16. The grains are randomly oriented, while the precipitates have the same orientations as the matrix. A subset of <hkl>

grains/phases are selected, with orientations parallel to the diffraction vector: The average Rietveld strains of the <hkl> subsets of all three phases were also taken and plotted in the same diagram to show agreement with the experimental results [Figure 56(c)]. The actual calculations use a tolerance of ± 5° in angle, and 1 ~ 2 % of all the grains were chosen to ensure a statistically-meaningful number [130]. A uniaxial compressive stress of 260 MPa was applied on the top surface of the cubic model at 973 K. Figure 56(c) shows that the matrix yields at around 200 MPa, and the matrix-lattice strain starts to decrease. While the matrix yields, the $L2_1$ and B2 precipitates absorb the applied stress and continue increasing their lattice strains, as the applied stress increases. These predictions [Figure 56(c)] are in good agreement with the experimental results [Figure 56(a)]. This trend implies that the Fe matrix has reached its yield stress, while the two precipitates remains elastic at this stress level. In Figure 56(c), two <hkl> peaks were randomly chosen for each phase to be plotted in order to demonstrate the lattice-strain differences under the same loading conditions during the elastic-plastic behavior. The average lattice-strain values of <hkl> peaks were also taken and plotted in the figure for each phase to demonstrate the agreement of the simulation results with the experimental data [Figures 56(a) and (c)]. From this observation, it can be inferred that during loading to 190 MPa, the matrix starts to plastically deform, whereas the precipitate elastically deforms, and the load arising from the elastic/plastic misfit between the matrix and the precipitate is transferred to the precipitate that continues to carry strains, as experimentally verified in Figure 56(a). Similarly, as the creep time increases, the load from the creeping matrix is believed to be transferred to the elastically-deforming precipitate with increasing strains

during creep at 190 MPa [Figure 56(b)]. The consideration of the initial thermal residual stress demonstrates the same trend in Figure 56(d).

5.6 Summary

The deformation behavior of the Fe-Cr-Ni-Al-Ti alloys strengthened by the hierarchical Ni_2TiAl/NiAl and single Ni_2TiAl precipitates has been studied at 973 K. The hierarchical precipitate-strengthened alloy with 2 weight percent (wt. %) Ti contains a coherent hierarchical precipitate with a two-phase coupled structure of the B2-NiAl and $L2_1$-Ni_2TiAl phases, while the single precipitate-strengthened alloy with 4-wt.-% Ti is reinforced by a semi-coherent single-$L2_1$-Ni_2TiAl precipitate with a high density of misfit dislocations. Both alloys are subjected to the aging treatment at 973 K for 100 hours following the solution-treatment at 1,473 K for 0.5 hour, which result in the average size of 111 ± 27 nm for the hierarchical precipitate and 220 ± 46 nm for the single precipitate, respectively.

The in-situ tension neutron-diffraction (ND) experiments on both alloys at 973 K were conducted to study the evolution of lattice strains on phase levels in combination with the crystal-plasticity finite-element model. The macroscopic stress-strain behavior is qualitatively consistent with the evolution of the phase strains, showing the interphase load transfer from the matrix to precipitate in the plastic regime. The macroscopic yield-strength at 973 K is in quantitative agreement with the stress values evaluated by the classical dispersion-strengthening theory, suggesting the Orowan dislocation bypass to be the governing deformation mechanism for both alloys at 973 K. The crystal-plasticity finite-element model shows the qualitative agreement with the experimental results until

softening occurs where the flow stress gradually decreases with increasing plastic strain, reflecting the significance of the diffusional process on the deformation behavior at 973 K. A relaxation test on the 4-wt.-%-Ti alloy at 973 K was carried out with in-situ neutron diffraction. These results revealed the gradual decrease in the precipitate strain transferred from the plastically-deforming matrix, as the relaxation time increases, which supports that the load-transfer capability at high temperatures is strongly affected by the diffusional flow along the interface between the matrix and precipitate. The in-situ tension tests at 973 K shows the higher level of the stress relaxation for the 4-wt.-%-Ti alloy during the ND measurements than that for the 2-wt.-%-Ti alloy, indicating the insufficient diffusional flow in the 2-wt.-%-Ti alloy with the coherent precipitate structure, relative to the 4-wt.-%-alloy with the semi-coherent precipitate. The load-transfer capability of the 2-and 4-wt.-%-Ti alloys is found to be related to the precipitate interface structures, such as the coherent strain field in the matrix, created by the lattice misfit between the matrix and precipitate. The coherent strain field in the matrix of the 2-wt.-%-Ti alloy plays an important role in enhancing the interaction between the precipitate and mobile dislocations, and, thus, the load-transfer capability and strengthening behavior of the material at high temperatures. Moreover, from the micromechanical modeling of the lattice strain, the load-partitioning mechanism is found to be load transferring from the Fe matrix to the hard precipitate during the in-situ creep deformation, which indicates the insufficient diffusional flow along the matrix/precipitate interface and a strong interaction between the matrix and mobile dislocations. This trend is in sharp contrast to the behavior of FBB8 at 973 K. These results could provide a new

alloy-design strategy, accelerate the advance in the development of elevated-temperature engineering materials, and broaden the applications of ferritic alloys at higher temperatures.

CHAPTER 6 SUMMARY AND CONCLUSIONS

The integrated experimental and theoretical techniques have been employed to investigate the structure-property relationships and deformation mechanisms of newly-designed ferritic alloys. The alloys are strengthened by either a single $L2_1$-Ni_2TiAl precipitate or hierarchical $L2_1$-Ni_2TiAl/B2-NiAl precipitate, and exhibit the superior creep resistance, relative to a NiAl-strengthened ferritic alloy (denoted as FBB8 in this study) and conventional ferritic steels at 973 K, which makes it ideal for high-temperature applications.

Systematic microstructural investigations were conducted on the hierarchical or single-precipitate-strengthened ferritic alloys, which are aged at 973 K for 100 hours after the solution treatment at 1,473 K for 0.5 hour, using transmission-electron microscopy (TEM), in-situ neutron-diffraction (ND), and atom-probe tomography (APT). Novel hierarchical or single-precipitate-strengthened ferritic alloys were developed by adding Ti into the NiAl-strengthened ferritic alloy. The addition of the 2-wt.-% Ti leads to the coherent hierarchical precipitate consisting of the parent $L2_1$-Ni_2TiAl phase, which is reinforced by the narrow B2-NiAl zones, whereas the addition of the 4-wt.-% Ti results in the semi-coherent single $L2_1$-Ni_2TiAl precipitates. These precipitates are embedded in the Fe matrix. The ND results reveal that the hierarchical structure gives rise to coherent interfaces between the Fe and precipitate phases with optimized misfit strains, which leads to the excellent creep resistance at 973 K. Moreover, the TEM results from the crept sample of the hierarchical-precipitate-strengthened ferritic alloy exhibit a strong interaction between the matrix and mobile dislocations.

The microstructural evolution of the hierarchical or single-precipitate-strengthened ferritic alloys was studied during aging treatments at 973 K following the solution treatment at 1,473 K. The detailed microstructures were characterized, using TEM, scanning-electron microscopy (SEM), and APT. Moreover, Vickers-hardness tests were conducted to study the effect of the microstructural evolution on the strengthening behavior of the materials. Both alloys contain a single $L2_1$-Ni_2TiAl phase as a primary precipitate with the different morphology, sizes, and inter-phase structures in the solution-treated state. The 2-wt.-%-Ti alloy consists of a coherent and cuboidal precipitate, which is reinforced by narrow anti-phase boundaries with an approximate width of ~ 10 nm within the precipitate. In contrast, the addition of the 4-wt.-% Ti content gives rise to a semi-coherent and irregular/polygonal-shaped precipitate, and the precipitate is decorated with misfit dislocations at the interface between the matrix and precipitate. During the subsequent aging treatments at 973 K, both alloys show different microstructural evolutions in terms of the internal structure, interface structure, and spatial arrangements of the precipitates (the alignment of the interface and small inter-separation of the precipitates), which are closely associated with the coherency strain.

The deformation behavior of the hierarchical or single-precipitate-strengthened ferritic alloys has been studied, using in-situ tension/relaxation/creep neutron-diffraction experiments. The in-situ tension ND experiments on both alloys at 973 K were conducted to study the evolution of lattice strains on phase levels in combination with the crystal-plasticity finite-element model. The macroscopic stress-strain behavior shows the qualitative agreement with the evolution of the phase strains. Specifically, the clear

interphase load-transfer from the matrix to precipitate in plastic regime is observed. The macroscopic yield-strength at 973 K is in quantitative agreement with stress values evaluated by the classical dispersion-strengthening theory, suggesting Orowan dislocation bypass to be the governing deformation mechanism for both alloys at 973 K. A relaxation test on the 4-wt.-%-Ti alloy at 973 K was conducted with the in-situ neutron diffraction. These results revealed the gradual decrease in the precipitate strain transferred from the plastically-deforming matrix, as the relaxation time increases, which supports that the diffusional flow occurs along the interface between the matrix and precipitate, which strongly affects the load-transfer capability at high temperatures. It was observed that the level of the stress relaxation for the 4-wt.-%-Ti alloy is higher than that for the 2-wt.-%-Ti alloy during the in-situ tension experiment, reflecting the insufficient diffusional flow in the 2-wt.-%-Ti alloy with the coherent precipitate structure, relative to the 4-wt.-%-Ti alloy with the semi-coherent precipitate. Moreover, from the micromechanical modeling of the lattice strain, the load-partitioning mechanism is found to be load-transferring from the Fe matrix to the hard precipitate during the in-situ creep/tension deformation, which indicates the insufficient diffusional flow along the matrix/precipitate interface and a strong interaction between the matrix and mobile dislocations. This trend is in sharp contrast to the behavior of FBB8 at 973 K.

CHAPTER 7 FUTURE WORK

The following topics will be suggested as the future work to expedite the potential structural application of ferritic alloys at elevated temperatures. Successful completion of the proposed research will help achieve an in-depth understanding of the structure-property relationships and broaden the application of ferritic alloys at higher temperatures.

(1) The current study has mainly focused on the mechanical properties at 973 K. Since the target temperature of the present materials is at and above 1,033 K, the optimization of heat-treatment conditions (solution/aging temperatures and times) requires a systematic microstructural study on these alloys at or above 1,033 K.

(2) Mechanical properties (creep, tension, and thermal fatigue) above 973 K, especially the creep property at stress levels close to 35 MPa and temperatures at or above 1,033 K are needed to be studied.

(3) Future experiments where the grain size is changed systematically (e.g., by grain growth during homogenization) can shed light on the diffusional flow accommodated by grain-boundary sliding.

(4) Detailed microstructures and dislocations need to be characterized using TEM in the creep-deformed samples as a function of temperature, stress, and creep time;

(5) The development of a creep model needs to be established, which incorporates the temporal evolution of microstructures that affect the creep resistance (e.g.,

precipitate coarsening) to quantitatively predict the long-term creep behavior at low stresses;

(6) Modeling efforts are necessary, which needs to confirm the magnitude of elastic mismatch strains, and can open the door to a prediction of the optimal concentration of Ti in these alloys.

(7) The detailed microstructural characterizations of the interface structure between the phases within the hierarchical precipitate using high-resolution TEM have to be conducted.

(8) The application of secondary processes, such as rolling or forging, is needed to reduce the grain size, which could improve the room-temperature ductility, and investigate the effect of the secondary processes on the microstructures and mechanical properties at room and elevated temperatures.

(9) The investigation of oxidation and steam corrosion resistance at and above 973 K has to be performed.

LIST OF REFERENCES

[1] Viswanathan R., Bakker W. Materials for ultrasupercritical coal power plants - boiler materials: part 1, Journal of Materials Engineering and Performance 10 (2001) 81.

[2] Viswanathan R. Materials technology for coal-fired power plants, Advanced Materials & Processes 162 (2004) 73.

[3] Ennis P.J., Czyrska-Filemonowicz A. Recent advances in creep-resistant steels for power plant applications, Sadhana 28 (2003) 709.

[4] Allen N.P. Creep of metals, Nature 157 (1946) 469.

[5] Allen N.P. Creep-resisting alloys for gas turbines, Nature 167 (1951) 836.

[6] Taneike M., Abe F., Sawada K. Creep-strengthening of steel at high temperatures using nano-sized carbonitride dispersions, Nature 424 (2003) 294.

[7] Yamamoto Y., Brady M.P., Lu Z.P., Maziasz P.J., Liu C.T., Pint B.A., More K.L., Meyer H., Payzant E.A. Creep-resistant, Al_2O_3-forming austenitic stainless steels, Science 316 (2007) 433.

[8] Hirata A., Fujita T., Wen Y.R., Schneibel J.H., Liu C.T., Chen M.W. Atomic structure of nanoclusters in oxide-dispersion-strengthened steels, Nature Materials 10 (2011) 922.

[9] Stoica G.M., Stoica A.D., Miller M.K., Ma D. Temperature-dependent elastic anisotropy and mesoscale deformation in a nanostructured ferritic alloy, Nature Communications 5 (2014) 1.

[10] Viswanathan R., Coleman K., Rao U. Materials for ultra-supercritical coal-fired power plant boilers, International Journal of Pressure Vessels and Piping 83

(2006) 778.

[11] Bhadeshia H. Design of ferritic creep-resistant steels, ISIJ International 41 (2001) 626.

[12] Viswanathan R., Henry J., Tanzosh J., Stanko G., Shingledecker J., Vitalis B., Purgert R. U.S. program on materials technology for ultra-supercritical coal power plants, Journal of Materials Engineering and Performance 14 (2005) 281.

[13] Goodstine S.L., Nava D.C. Use of surface modification of alloys for ultrasupercritical coal-fired boilers. Proc. 4th International Conference on Advances in Materials Technology for Fossil Power Plants, 2004.

[14] Kostka A., Tak K.G., Hellmig R.J., Estrin Y., Eggeler G. On the contribution of carbides and micrograin boundaries to the creep strength of tempered martensite ferritic steels, Acta Materialia 55 (2007) 539.

[15] Masuyama F., Viswanathan R., Nutting J. Advanced heat resistant steels for power generation, The Institute of Materials, London (1999) 33.

[16] Viswanathan R., Bakker W. Materials for ultrasupercritical coal power plants—Boiler materials: Part 1, Journal of Materials Engineering and Performance 10 (2001) 81.

[17] Schinkel J.W., Rademakers P.L.F., Drenth B.R., Scheepens C.P. Heat treatment, aging effects, and microstructure of 12 Pct Cr steels, Journal of Heat Treating 3 (1984) 237.

[18] Abe F., Nakazawa S., Araki H., Noda T. The role of microstructural instability on creep behavior of a martensitic 9Cr-2W steel, Metallurgical Transactions A 23

(1992) 469.

[19] Klueh R.L. Elevated temperature ferritic and martensitic steels and their application to future nuclear reactors, International Materials Reviews 50 (2005) 287.

[20] Eggeler G. The effect of long-term creep on particle coarsening in tempered martensite ferritic steels, Acta Metallurgica 37 (1989) 3225.

[21] Orlová A., Buršík J., Kuchařová K., Sklenička V. Microstructural development during high temperature creep of 9% Cr steel, Materials Science and Engineering: A 245 (1998) 39.

[22] Yoshizawa M., Igarashi M., Moriguchi K., Iseda A., Armaki H.G., Maruyama K. Effect of precipitates on long-term creep deformation properties of P92 and P122 type advanced ferritic steels for USC power plants, Materials Science and Engineering: A 510–511 (2009) 162.

[23] Ennis P.J., Zielinska-Lipiec A., Wachter O., Czyrska-Filemonowicz A. Microstructural stability and creep rupture strength of the martensitic steel P92 for advanced power plant, Acta Materialia 45 (1997) 4901.

[24] Strang A., Vodarek V. Z phase formation in martensitic 12CrMoVNb steel, Materials Science and Technology 12 (1996) 552.

[25] Teng Z.K., Miller M.K., Ghosh G., Liu C.T., Huang S., Russell K.F., Fine M.E., Liaw P.K. Characterization of nanoscale NiAl-type precipitates in a ferritic steel by electron microscopy and atom probe tomography, Scripta Materialia 63 (2010) 61.

[26] Teng Z.K., Ghosh, G. Miller, M. K. Huang, S., Clausen, B., Brown, D. W., Liaw, P. K. Neutron-diffraction study and modeling of the lattice parameters of a NiAl-precipitate-strengthened Fe-based alloy, Acta Materialia 60 (2012) 5362.

[27] Zhu S.M., Tjong S.C., Lai J.K.L. Creep behavior of a β′ (NiAl) precipitation strengthened ferritic Fe–Cr–Ni–Al alloy, Acta Materialia 46 (1998) 2969.

[28] Stallybrass C., Schneider A., Sauthoff G. The strengthening effect of (Ni,Fe)Al precipitates on the mechanical properties at high temperatures of ferritic Fe–Al–Ni–Cr alloys, Intermetallics 13 (2005) 1263.

[29] Stallybrass C., Sauthoff G. Ferritic Fe–Al–Ni–Cr alloys with coherent precipitates for high-temperature applications, Materials Science and Engineering: A 387-389 (2004) 985.

[30] Teng Z.K., Liu C.T., Ghosh G., Liaw P.K., Fine M.E. Effects of Al on the microstructure and ductility of NiAl-strengthened ferritic steels at room temperature, Intermetallics 18 (2010) 1437.

[31] Calderon H., Fine M.E. Coarsening kinetics of coherent NiAl-type precipitates in Fe-Ni-Al and Fe-Ni-Al-Mo alloys, Materials Science and Engineering 63 (1984) 197.

[32] Teng Z.K., Zhang F., Miller M.K., Liu C.T., Huang S., Chou Y.T., Tien R.H., Chang Y.A., Liaw P.K. New NiAl-strengthened ferritic steels with balanced creep resistance and ductility designed by coupling thermodynamic calculations with focused experiments, Intermetallics 29 (2012) 110.

[33] Teng Z.K., Liu C.T., Miller M.K., Ghosh G., Kenik E.A., Huang S., Liaw P.K.

Room temperature ductility of NiAl-strengthened ferritic steels: Effects of precipitate microstructure, Materials Science and Engineering: A 541 (2012) 22.

[34] Huang S., Ghosh G., Li X., Ilavsky J., Teng Z., Liaw P. Effect of Al on the NiAl-type B2 precipitates in ferritic superalloys, Metallurgical and Materials Transactions A 43 (2012) 3423.

[35] Taillard R., Pineau A., Thomas B.J. The precipitation of the intermetallic compound NiAl in Fe-19wt.%Cr alloys, Materials Science and Engineering 54 (1982) 209.

[36] Edahiro T., Kouzai K., Yasuda H.Y. Mechanical properties and hardening mechanism of Fe–Al–Ni single crystals containing NiAl precipitates, Acta Materialia 61 (2013) 1716.

[37] Kapoor M., Isheim D., Ghosh G., Vaynman S., Fine M.E., Chung Y.-W. Aging characteristics and mechanical properties of 1600 MPa body-centered cubic Cu and B2-NiAl precipitation-strengthened ferritic steel, Acta Materialia 73 (2014) 56.

[38] Villars P., Calvert L.D. Pearson's Handbook of crystallographics data for intermetallic phases., Metal Park, OH: ASM international (1985).

[39] Sims C.T., Hagel W.C. The superalloys, John Wiley, New York (1972) 64.

[40] Reed R.C. The superalloys: fundamentals and applications, Cambridge university press, 2006.

[41] Yukawa N., Mizutani M., Saka H. Effect of aluminum upon phase changes and age-hardening behaviors in 17-7 ph strainless steel, Transactions of the Iron Steel

Institute of Japan 9 (1969) 245.

[42] Seetharaman V., Sundararaman M., Krishnan R. Precipitation hardening in a PH 13-8 Mo stainless steel, Materials Science and Engineering 47 (1981) 1.

[43] Blavette D., Martin C., Gallot J. Atomic probe analysis of precipitates in a FeCr20Ni2Al2 alloy, Scripta Metallurgica 16 (1982) 59.

[44] Miller M.K., Hetherington M.G. Atom probe analysis of β' precipitation in a model iron-based Fe-Ni-Al-Mo superalloy, Le Journal de Physique Colloques 50 (1989) C8.

[45] Teng Z.K., Zhang F., Miller M.K., Liu C.T., Huang S., Chou Y.T., Tien R.H., Chang Y.A., Liaw P.K. Thermodynamic modeling and experimental validation of the Fe-Al-Ni-Cr-Mo alloy system, Materials Letters 71 (2012) 36.

[46] Calderon H., Fine M., Weertman J. Coarsening and morphology of β′ particles in Fe-Ni-Al-Mo ferritic alloys, Metallurgical and Materials Transactions A 19 (1988) 1135.

[47] Muñoz-Morris M.A., Calderon N., Morris D.G. Coarsening kinetics of metastable nanoprecipitates in a Fe–Ni–Al alloy, Journal of Materials Science 43 (2008) 3674.

[48] Calderon H., Fine M., Weertman J. Coarsening and morphology of β′ particles in Fe-Ni-Al-Mo ferritic alloys, Metallurgical Transactions A 19 (1988) 1135.

[49] Calderon H., Weertman J., Fine M. Effect of cyclic plastic deformation on elevated temperature Ostwald ripening of an alloy with coherent precipitates, Scripta Metallurgica 18 (1984) 587.

[50] Sun Z., Song G., Ilavsky J., Ghosh G., Liaw P.K. Nano-sized precipitate stability and its controlling factors in a NiAl-strengthened ferritic alloy, Scientific Reports 5 (2015) 16081.

[51] Jung I., Sauthoff G. Dependence of creep on the distribution of strengthening precipitates, Strength of Metals and Alloys. 1 (1985) 731.

[52] Jung I., Sauthoff G. The effect of ordered precipitates on creep in ferritic Fe--Ni--Al alloys, Creep and Fracture of Engineering Materials and Structures (1987) 257.

[53] Vo N.Q., Liebscher C.H., Rawlings M.J., Asta M., Dunand D.C. Creep properties and microstructure of a precipitation-strengthened ferritic Fe–Al–Ni–Cr alloy, Acta Materialia 71 (2014) 89.

[54] Huang S., Brown D., Clausen B., Teng Z., Gao Y., Liaw P.K. In situ neutron-diffraction studies on the creep behavior of a ferritic superalloy, Metallurgical and Materials Transactions A 43 (2011) 1497.

[55] Huang S., Gao Y., An K., Zheng L., Wu W., Teng Z., Liaw P.K. Deformation mechanisms in a precipitation-strengthened ferritic superalloy revealed by in situ neutron diffraction studies at elevated temperatures, Acta Materialia 83 (2015) 137.

[56] Miracle D.B. Overview No. 104 The physical and mechanical properties of NiAl, Acta Metallurgica et Materialia 41 (1993) 649.

[57] Darolia R. NiAl alloys for high-temperature structural applications, Journal of the Minerals 43 (1991) 44.

[58] Bei H., George E.P., Brown D.W., Pharr G.M., Choo H., Porter W.D., Bourke M.A.M. Thermal-expansion behavior of a directionally solidified NiAl–Mo composite investigated by neutron diffraction and dilatometry, Journal of Applied Physics 97 (2005) 123503.

[59] Sun Z., Liebscher C.H., Huang S., Teng Z., Song G., Wang G., Asta M., Rawlings M., Fine M.E., Liaw P.K. New design aspects of creep-resistant NiAl-strengthened ferritic alloys, Scripta Materialia 68 (2013) 384.

[60] Liebscher C.H., Radmilovic V., Dahmen U., Asta M., Ghosh G. On the formation of hierarchically structured $L2_1$-Ni_2TiAl type precipitates in a ferritic alloy, Journal of Materials Science 48 (2013) 2067.

[61] Liebscher C.H., Radmilović V.R., Dahmen U., Vo N.Q., Dunand D.C., Asta M., Ghosh G. A hierarchical microstructure due to chemical ordering in the bcc lattice: Early stages of formation in a ferritic Fe–Al–Cr–Ni–Ti alloy, Acta Materialia 92 (2015) 220.

[62] Strutt P., Polvani R., Ingram J. Creep behavior of the heusler type structure alloy Ni_2AlTi, Metallurgical and Materials Transactions A 7 (1976) 23.

[63] Polvani R., Tzeng W.-S., Strutt P. High temperature creep in a semi-coherent NiAl-Ni_2AlTi alloy, Metallurgical and Materials Transactions A 7 (1976) 33.

[64] Bendersky L.A., Voorhees P.W., Boettinger W.J., Johnson W.C. The role of elastic energy in the morphological development of a NiTiAl alloy, Scripta Metallurgica 22 (1988) 1029.

[65] Matsumura S., Oyama H., Oki K. Dynamical behavior of ordering with phase

separation in off-stoichiometric Fe_3Si alloys, Materials Transactions JIM 30 (1989) 695.

[66] Allen S.M., Cahn J.W. Mechanisms of phase transformations within the miscibility gap of Fe-rich Fe-Al alloys, Acta Metallurgica 24 (1976) 425.

[67] Swann P., Grånäs L., Lehtinen B. The B2 and DO3 ordering reactions in iron–slicon alloys in the vicinity of the curie temperature, Metal Science 9 (1975) 90.

[68] Voorhees P.W., McFadden G.B., Johnson W.C. On the morphological development of second-phase particles in elastically-stressed solids, Acta Metallurgica et Materialia 40 (1992) 2979.

[69] Millán J., Sandlöbes S., Al-Zubi A., Hickel T., Choi P., Neugebauer J., Ponge D., Raabe D. Designing Heusler nanoprecipitates by elastic misfit stabilization in Fe–Mn maraging steels, Acta Materialia 76 (2014) 94.

[70] Raabe D., Ponge D., Dmitrieva O., Sander B. Designing ultrahigh strength steels with good ductility by combining transformation induced plasticity and martensite aging, Advanced Engineering Materials 11 (2009) 547.

[71] Schneider C.A., Rasband W.S., Eliceiri K.W. NIH Image to ImageJ: 25 years of image analysis, Nature Methods 9 (2012) 671.

[72] Bourke M.A.M., Dunand D.C., Ustundag E. SMARTS – a spectrometer for strain measurement in engineering materials, Applied Physics A 74 (2002) s1707.

[73] Hirsch P.B., Howie A., Nicholson R.B., Pashley D.W., Whelan M.J. Electron microscopy of thin crystals, Plenum Press, New York (1965).

[74] Kakehi K. Effect of primary and secondary precipitates on creep strength of Ni-

base superalloy single crystals, Materials Science and Engineering: A 278 (2000) 135.

[75] Larson A.C., Von Dreele R.B., General Structure Analysis System (GSAS). Los Alamos National Laboratory Report LAUR (1994) 86.

[76] Song G., Sun Z., Li L., Xu X., Rawlings M., Liebscher C.H., Clausen B., Poplawsky J., Leonard D.N., Huang S., Teng Z., Liu C.T., Asta M.D., Gao Y., Dunand D.C., Ghosh G., Chen M., Fine M.E., Liaw P.K. Ferritic alloy with extreme creep resistance via coherent hierarchical precipitates, Scientific Reports 5 (2015) 16327.

[77] Haynes, W.M., Lide, D. R., Property of solids. CRC handbook of chemistry and physics. 91st ed. Section 12, Internet version; (2011).

[78] Yan X., Grytsiv A., Rogl P., Pomjakushin V., Palm M. The Heusler phase $Ti_{25}(Fe_{50-x}Ni_x)Al_{25}$ $(0 \leq x \leq 50)$; structure and constitution, Journal of Phase Equilibria and Diffusion 29 (2008) 500.

[79] Sawada K., Kubo K., Abe F. Creep behavior and stability of MX precipitates at high temperature in 9Cr–0.5Mo–1.8W–VNb steel, Materials Science and Engineering: A 319–321 (2001) 784.

[80] Masuyama F., Komai N. Evaluation of long-term creep rupture strength of tungsten-strengthened advanced 9-12% Cr steels, Key Engineering Materials 171 (2000) 179.

[81] Kimura K., Sawada K., Kushima H., Toda Y. Long-term creep strength of creep strength enhanced ferritic steels. in: Cen K, Chi Y, Wang F, (Eds.). Challenges of

Power Engineering and Environment. Springer Berlin Heidelberg, 2007. pp. 1059.

[82] Henderson P. Dislocations at γ/γ′ interfaces during the creep of nickel-base superalloys, Scripta Metallurgica 22 (1988) 1103.

[83] Tjong S.C., Zhang J.S. Abnormal creep behavior of ferritic Fe-24Cr-4Al stainless steel, Scripta Metallurgica et Materialia 30 (1994) 1397.

[84] Gibeling J.C., Nix W.D. The description of elevated temperature deformation in terms of threshold stresses and back stresses: A review, Materials Science and Engineering 45 (1980) 123.

[85] Zhang Z.W., Liu C.T., Wang X.L., Littrell K.C., Miller M.K., An K., Chin B.A. From embryos to precipitates: A study of nucleation and growth in a multicomponent ferritic steel, Physical Review B 84 (2011) 174114.

[86] Srinivasan R., Banerjee R., Hwang J.Y., Viswanathan G.B., Tiley J., Dimiduk D.M., Fraser H.L. Atomic scale structure and chemical composition across order-disorder interfaces, Physical Review Letters 102 (2009) 086101.

[87] Stone H.J., Holden T.M., Reed R.C. Determination of the plane specific elastic constants of waspaloy using neutron diffraction, Scripta Materialia 40 (1999) 353.

[88] Sears V.F. Neutron scattering lengths and cross sections, Neutron News 3 (1992) 26.

[89] Kubaschewski O. Iron-binary phase diagrams, (1982).

[90] Nathal M.V., Mackay R.A., Garlick R.G. Temperature dependence of γ-γ' lattice mismatch in Nickel-base superalloys, Materials Science and Engineering 75 (1985) 195.

[91] Mitchell B.S. An introduction to materials engineering and science for chemical and materials engineers, Hoboken, NJ : John Wiley (2004).

[92] Kelly A., Nicholson R.B. Precipitation hardening, Progress in Materials Science 10 (1963) 151.

[93] Johnson W., Cahn J. Elastically induced shape bifurcations of inclusions, Acta Metallurgica 32 (1984) 1925.

[94] Calderon H.A., Kostorz G., Qu Y.Y., Dorantes H.J., Cruz J.J., Cabanas-Moreno J.G. Coarsening kinetics of coherent precipitates in Ni-Al-Mo and Fe-Ni-Al alloys, Materials Science and Engineering: A 238 (1997) 13.

[95] Marquis E.A., Dunand D.C. Model for creep threshold stress in precipitation-strengthened alloys with coherent particles, Scripta Materialia 47 (2002) 503.

[96] Seidman D.N., Marquis E.A., Dunand D.C. Precipitation strengthening at ambient and elevated temperatures of heat-treatable Al(Sc) alloys, Acta Materialia 50 (2002) 4021.

[97] Krug M.E., Dunand D.C. Modeling the creep threshold stress due to climb of a dislocation in the stress field of a misfitting precipitate, Acta Materialia 59 (2011) 5125.

[98] Grose D.A., Ansell G.S. The influence of coherency strain on the elevated temperature tensile behavior of Ni-15Cr-AI-Ti-Mo alloys, Metallurgical Transactions A 12 (1981) 1631.

[99] Van Sluytman J.S., Pollock T.M. Optimal precipitate shapes in nickel-base γ–γ′ alloys, Acta Materialia 60 (2012) 1771.

[100] Ricks R.A., Porter A.J., Ecob R.C. The growth of γ′ precipitates in nickel-base superalloys, Acta Metallurgica 31 (1983) 43.

[101] Larson F.R., Miller J. A time-temperature relationship for rupture and creep stresses, Transactions of the American Society of Mechanical Engineers 74 (1952) 765.

[102] Ardell A.J., Nicholson R.B. The coarsening of γ' in Ni-Al alloys, Journal of Physics and Chemistry of Solids 27 (1966) 1793.

[103] MacKay R.A., Nathal M.V. γ′ coarsening in high volume fraction nickel-base alloys, Acta Metallurgica et Materialia 38 (1990) 993.

[104] Yeom S.J., Yoon D.Y., Henry M.F. The morphological changes of γ′ precipitates in a Ni-8Al (wt pct) alloy during their coarsening, Metallurgical Transactions A 24 (1993) 1975.

[105] Meher S., Nag S., Tiley J., Goel A., Banerjee R. Coarsening kinetics of γ′ precipitates in cobalt-base alloys, Acta Materialia 61 (2013) 4266.

[106] Royer A., Bastie P., Veron M. In situ determination of γ′ phase volume fraction and of relations between lattice parameters and precipitate morphology in Ni-based single crystal superalloy, Acta Materialia 46 (1998) 5357.

[107] Miyazaki T., Nakamura K., Mori H. Experimental and theoretical investigations on morphological changes of γ′ precipitates in Ni -Al single crystals during uniaxial stress-annealing, Journal of Materials Science 14 (1979) 1827.

[108] Stevens R.A., Flewitt P.E.J. The effects of γ′ precipitate coarsening during isothermal aging and creep of the nickel-base superalloy IN-738, Materials

Science and Engineering 37 (1979) 237.

[109] Cliff G., Lorimer G.W. The quantitative analysis of thin specimens, Journal of Microscopy 103 (1975) 203.

[110] Larson D.J., Prosa T.J., Ulfig R.M., Geiser B.P., Kelly T.F. Local electrode atom probe tomography, Springer, New York, 2013.

[111] Thompson K., Lawrence D., Larson D., Olson J., Kelly T., Gorman B. In situ site-specific specimen preparation for atom probe tomography, Ultramicroscopy 107 (2007) 131.

[112] Sun Z., Song G., Ilavsky J., Liaw P.K. Duplex precipitates and their effects on the room-temperature fracture behaviour of a NiAl-strengthened ferritic alloy, Materials Research Letters 3 (2015) 128.

[113] Wusatowska-Sarnek A.M., Ghosh G., Olson G.B., Blackburn M.J., Aindow M. Characterization of the microstructure and phase equilibria calculations for the powder metallurgy superalloy IN100, Journal of Materials Research 18 (2003) 2653.

[114] Phillips R. Crystals, defects and microstructures: modeling across scales, Cambridge University Press, 2001.

[115] Gao Y., Lu W., Suo Z. A mesophase transition in a binary monolayer on a solid surface, Acta Materialia 50 (2002) 2297.

[116] Gao Y., Suo Z. Domain dynamics in a ferroelastic epilayer on a paraelastic substrate, Journal of applied mechanics 69 (2002) 419.

[117] Eshelby J.D. The determination of the elastic field of an ellipsoidal inclusion, and

related problems. Proceedings of the Royal Society of London A: Mathematical, Physical and Engineering Sciences, vol. 241: The Royal Society, 1957. p.376.

[118] Ardell A.J., Nicholson R.B. On the modulated structure of aged Ni-Al alloys: with an appendix on the elastic interaction between inclusions by J. D. Eshelby, Acta Metallurgica 14 (1966) 1295.

[119] Calliari I., Magrini M., Dabalà M. Microstructural evolution of udimet 720 superalloy, Journal of Materials Engineering and Performance 8 (1999) 111.

[120] Porter D.A., Easterling K.E., Sherif M. Phase transformations in metals and alloys, (Revised Reprint), CRC press, 2011.

[121] Su C.H., Voorhees P.W. The dynamics of precipitate evolution in elastically stressed solids—II. Particle alignment, Acta Materialia 44 (1996) 2001.

[122] Gao Y., Suo Z. The orientation of the self-assembled monolayer stripes on a crystalline substrate, Journal of the Mechanics and Physics of Solids 51 (2003) 147.

[123] Gao Y., Larson B.C. Displacement fields and self-energies of circular and polygonal dislocation loops in homogeneous and layered anisotropic solids, Journal of the Mechanics and Physics of Solids 83 (2015) 104.

[124] Kim S.-H., Kim H., Kim N.J. Brittle intermetallic compound makes ultrastrong low-density steel with large ductility, Nature 518 (2015) 77.

[125] Wang Y.-D., Tian H., Stoica A.D., Wang X.-L., Liaw P.K., Richardson J.W. The development of grain-orientation-dependent residual stressess in a cyclically deformed alloy, Nature Materials 2 (2003) 101.

[126] Daymond M.R., Preuss M., Clausen B. Evidence of variation in slip mode in a polycrystalline nickel-base superalloy with change in temperature from neutron diffraction strain measurements, Acta Materialia 55 (2007) 3089.

[127] Daymond M.R., Priesmeyer H.G. Elastoplastic deformation of ferritic steel and cementite studied by neutron diffraction and self-consistent modelling, Acta Materialia 50 (2002) 1613.

[128] Grant B.M.B., Francis E.M., Quinta da Fonseca J., Daymond M.R., Preuss M. Deformation behaviour of an advanced nickel-based superalloy studied by neutron diffraction and electron microscopy, Acta Materialia 60 (2012) 6829.

[129] Santisteban J., Daymond M., James J., Edwards L. ENGIN-X: a third-generation neutron strain scanner, Journal of Applied Crystallography 39 (2006) 812.

[130] Zheng L.L., Gao Y.F., Lee S.Y., Barabash R.I., Lee J.H., Liaw P.K. Intergranular strain evolution near fatigue crack tips in polycrystalline metals, Journal of the Mechanics and Physics of Solids 59 (2011) 2307.

[131] Jeong C.Y., Nam S.W., Ginsztler J. Activation processes of stress relaxation during hold time in 1Cr–Mo–V steel, Materials Science and Engineering: A 264 (1999) 188.

[132] Chen J.F., Jiang J.T., Zhen L., Shao W.Z. Stress relaxation behavior of an Al–Zn–Mg–Cu alloy in simulated age-forming process, Journal of Materials Processing Technology 214 (2014) 775.

[133] Yong L., Jingchuan Z. Effects of triple heat treatment on stress relaxation resistance of BT20 alloy, Mechanics of Materials 40 (2008) 792.

[134] Ma S., Rangaswamy P., Majumdar B.S. Microstress evolution during in situ loading of a superalloy containing high volume fraction of γ′ phase, Scripta Materialia 48 (2003) 525.

[135] Nembach E. Particle strengthening of metals and alloys, Wiley, New York, 1997.

[136] Jeon S., Park J. Precipitation strengthening behavior of Al-Li single crystals, Acta Materialia 44 (1996) 1449.

[137] Ardell A. Precipitation hardening, Metallurgical Transactions A 16 (1985) 2131.

[138] Kocks U.F. The relation between polycrystal deformation and single-crystal deformation, Metallurgical and Materials Transactions 1 (1970) 1121.

[139] Ghosh G., Olson G.B. The isotropic shear modulus of multicomponent Fe-base solid solutions, Acta Materialia 50 (2002) 2655.

[140] Noebe R.D., Bowman R.R., Nathal M.V. Physical and mechanical properties of the B2 compound NiAl, International Materials Reviews 38 (1993) 193.

[141] Kassner M.E., Perez-Prado M.T. Fundamentals of Creep in Metals and Alloys, Elsevier (2004) pp. 151.

[142] Martin J.W. Micromechanisms in particle-hardened alloys, CUP Archive, 1980.

[143] Marquis E.A., Seidman D.N., Dunand D.C. Effect of Mg addition on the creep and yield behavior of an Al–Sc alloy, Acta Materialia 51 (2003) 4751.

[144] Chen Y., Schuh C.A. Geometric considerations for diffusion in polycrystalline solids, Journal of Applied Physics 101 (2007) 063524.

[145] Schiøtz J., Tolla F.D.D., Jacobsen K.W. Softening of nanocrystalline metals at very small grain sizes Nature 391 (1998) 561.

[146] Yip S. The strongest size, Nature 391 (1998) 532.

[147] Lasalmonie A., Strudel J.L. Influence of grain size on the mechanical behaviour of some high strength materials, Journal of Materials Science 21 (1986) 1837.

[148] Wei Y., Bower A.F., Gao H. Recoverable creep deformation due to heterogeneous grain-boundary diffusion and sliding, Scripta Materialia 57 (2007) 933.

[149] Wei Y., Bower A.F., Gao H. Enhanced strain-rate sensitivity in fcc nanocrystals due to grain-boundary diffusion and sliding, Acta Materialia 56 (2008) 1741.

[150] Francis E.M., Grant B.M.B., Fonseca J.Q.d., Phillips P.J., Mills M.J., Daymond M.R., Preuss M. High-temperature deformation mechanisms in a polycrystalline nickel-base superalloy studied by neutron diffraction and electron microscopy, Acta Materialia 74 (2014) 18.

[151] Haynes W.M., Lide D.R. Property of solids, CRC handbook of chemistry and physics. 91st ed. Section 12, Internet version (2011).

APPENDIX: TABLES AND FIGURES

Table 1. Evolution of four generations of ferritic steels (The compositions are summarized in Table 2) [15].

Generation	Years	Alloy modifications	Strength 10^5 h creep rupture achieved (MPa)	Example alloys	Maximum metal use temperature. K
1	1960-1970	Addition of Mo, Nb, or V to simple 12Cr and 9Cr Mo steels	60	EM12, HCM9M, HT9, Tempaloy F9, HT91	939
2	1970-1985	Optimization of C, Nb, and V	100	HCM12, T91, HCM2S	866
3	1985-1995	Partial substitution of W for Mo	140	P-92, P-122 (NF616, HCM12A)	893
4	Emerging	Increase of W and addition of Co	180	NF12, SAVE12	923

Table 2. Nominal chemical compositions of ferritic steels for boilers [1]. ([*]American Society of Mechanical Engineers, [#]Japanese Industrial Standards)

Steels		Specification		Chemical Composition (mass%)												
		[*]ASME	[#]JIS	C	Si	Mn	Cr	Mo	W	Co	V	Nb	B	N	Others	Manufacturers
1-1/4 Cr	T11	T11	-	0.15	0.5	0.45	1.25	0.5	-	-	-	-	-	-	-	-
	NFIH		-	0.12			1.25	1.0	-	-	0.2	0.07	-	-	-	Nippon Steel
2Cr	T22	T22	STBA24J	0.12	0.3	0.45	2.25	1.0	-	-	-	-	-	-	-	-
	HCM2S	T23	STBA24J1	0.06	0.2	0.45	2.25	0.1	1.6	-	0.25	0.05	0.003	-	-	Sumitomo
	Tempaloy F-2W	-	-	-	-	-	2.0	0.6	1.0	-	0.25	0.05	-	-	-	NKK
9Cr	T9	T9	STBA26	0.12	0.6	0.45	9.0	1.0	-	-	-	-	-	-	-	Vallourec Mannesman
	HCM9M	-	STBA27	0.07	0.3	0.45	9.0	2.0	-	-	-	-	-	-	-	Sumitomo
	T91	T91	STBA28	0.10	0.4	0.45	9.0	1.0	-	-	0.2	0.08	-	0.05	0.8Ni	Vallourec Mannesman
	E911	-	-	0.12	0.2	0.51	9.0	0.94	0.9	-	0.2	0.06	-	0.06	0.25Ni	Sumitomo
	NF616	T92	STBA29	0.07	0.06	0.45	9.0	0.5	1.8	-	0.2	0.05	0.004	0.06	-	Nippon Steel
12Cr	HT91	(DIN × 20CrMoV121)		0.20	0.4	0.60	12.0	1.0	-	-	0.25	-	-	-	0.5Ni	Vallourec Mannesman
	HT9	(DIN × 20CrMoWV121)		0.20	0.4	0.60	12.0	1.0	0.5	-	0.25	-	-	-	0.5Ni	Vallourec Mannesman
	Tempaloy F12M	-	-	-	-	-	12.0	0.7	0.7	-	-	-	-	0.03	-	NKK
	HCM12	-	-	0.10	0.3	0.55	12.0	1.0	1.0	-	0.25	0.05	-	0.05	-	-
	TB12	-	SUS410J2TB	0.08	0.05	0.50	12.0	0.5	1.8	-	0.2	0.05	0.30	0.06	0.1Ni	-
	HCM12A	T122	SUS410J3TB	0.11	0.1	0.60	12.0	0.4	2.0	-	0.2	0.05	0.003	0.05	1.0Cu	Sumitomo
	NF12	-	-	0.08	0.2	0.50	11.0	0.2	2.6	2.5	0.2	0.07	0.004	0.04	-	Nippon Steel
	SAVE12	-	-	0.10	0.3	0.20	11.0	-	3.0	3.0	0.2	0.07	-	-	0.07Ta, 0.04Nd	Sumitomo

Table 3. Chemical compositions of phases in a Fe-12.6Al-10.1Cr-8.9Ni-2.2Ti-1.8Mo (at. %) alloy obtained, using the chemical analysis (bulk) and APT. (C_o; bulk composition, C_{L21}; $L2_1$ composition, C_{B2}; B2 composition, C_m; Fe matrix composition, $C_{S.P}$; secondary precipitate composition, C'_m; combined compositions of the secondary precipitates and matrix, C_{po}; primary precipitate compositions)

Composition	Material	Phase	Al	Fe	Ni	Ti	Mo	Cr
Experimental	Bulk	(C_o)	12.518	64.243	8.977	2.157	1.834	10.134
	Primary precipitate	$L2_1$ (C_{L21})	29.253 ± 0.230	18.057 ± 0.188	36.235 ± 0.209	15.399 ± 0.188	0.466 ± 0.037	0.591 ± 0.048
		B2 (C_{B2})	38.206 ± 0.039	14.030 ± 0.028	42.826 ± 0.037	4.428 ± 0.015	0.075 ± 0.003	0.432 ± 0.005
	Matrix	Fe (C_m)	7.096 ± 0.018	75.859 ± 0.033	1.548 ± 0.009	0.407 ± 0.005	2.283 ± 0.010	12.807 ± 0.026
	Secondary precipitate	B2 ($C_{S.P}$)	34.449 ± 1.109	17.788 ± 0.939	41.580 ± 1.260	3.105 ± 0.437	0.698 ± 0.241	2.376 ± 0.372
Calculated	Combining matrix	Fe (C'_m)	7.858 ± 0.044	74.242 ± 0.036	2.663 ± 0.032	0.482 ± 0.162	2.239 ± 0.152	12.517 ± 0.044
	Primary precipitate	$L2_1$ + B2 (C_{po})	34.795 ± 0.044	16.445 ± 0.036	39.160 ± 0.032	10.163 ± 0.162	-0.101 ± 0.152	-1.255 ± 0.044

Table 4. Chemical composition: Chemical compositions (in atomic percent) of the bulk sample, derived from chemical analyses, and the constitutive phases in the Ni_2TiAl-strengthened ferritic alloy, obtained from the transmission-electron-microscopy energy-dispersive X-ray spectroscopy (TEM-EDS) analysis. The uncertainties for the EDS results are represented by the standard deviation from the measurement series.

Phase	*Fe*	*Cr*	*Al*	*Ni*	*Ti*	*Mo*	*Zr*
Bulk	61.6	10.1	12.8	8.9	4.5	1.9	0.1
Fe	74.9 ± 0.5	12.8 ± 0.2	7.0 ± 0.4	2.1 ± 0.2	1.0 ± 0.1	2.0 ± 0.2	0.2 ± 0.1
$L2_1$	22.9 ± 3.7	1.0 ± 0.7	25.0 ± 2.0	33.8 ± 1.9	16.5 ± 0.9	0.1 ± 0.1	0.5 ± 0.3

Table 5. Lattice parameters and misfits: Average lattice parameters of the Fe and $L2_1$ phases and corresponding misfits as a function of temperature.

Temperature (K)	Rietveld refinement		
	Fe (Å)	$L2_1$ (Å)	Misfit (%)
300	2.88643 ± 0.00002	5.85376 ± 0.00023	1.391 ± 0.288
845	2.90663 ± 0.00003	5.89786 ± 0.00027	1.445 ± 0.326
973	2.91322 ± 0.00003	5.91085 ± 0.00024	1.436 ± 0.293

Table 6. Thermal expansion: Coefficients of thermal expansion (CTEs) of the Fe and Ni_2TiAl phases in the Ni_2TiAl-strengthened ferritic alloy. For comparison, the CTEs of the Fe and Fe_2TiAl phases from the previous reports are included.

Phase	CTE ($\times 10^{-5}$ K^{-1})	
Fe	1.34 ± 0.08	Present study
Fe	1.18	[151]
Ni_2TiAl	1.42 ± 0.04	Present study
Fe_2TiAl	1.45	[78]

Table 7. Composition estimation by structure factor: Ratio of the square of the structure factor (F) and intensity (I) between different $L2_1$ compounds with varying Ti and Fe contents, and the resulting volume fraction (V_f) of the $L2_1$ phase.

Composition (at. %)	$(F_{L21})^2/(F_{Fe})^2$	I_{L21}/I_{Fe}	V_f (%)
	$(220)_{L21}/(110)_{Fe}$		
$(Ni_{35}Fe_{15})(Al_{25})(Ti_{17.5}Fe_{7.5})$	0.738 ± 9.3×10^{-5}	0.178 ± 0.009	19.471 ± 0.007
$(Ni_{35}Fe_{15})(Al_{25})(Ti_{20}Fe_{5})$	0.608 ± 9.3×10^{-5}	0.178 ± 0.009	22.698 ± 0.011
$(Ni_{35}Fe_{15})(Al_{25})(Ti_{22.5}Fe_{2.5})$	0.490 ± 9.3×10^{-5}	0.178 ± 0.009	26.693 ± 0.015
$(Ni_{35}Fe_{15})(Al_{25})(Ti_{25})$	0.385 ± 9.3×10^{-5}	0.178 ± 0.009	31.668 ± 0.023

Table 8. Volume-fraction calculation: Intensity ratio of $(220)_{L21}/(110)_{Fe}$ as a function of temperature with a composition of $(Ni_{35}Fe_{15})(Al_{25})(Ti_{20}Fe_5)$ of the $L2_1$ phase, and the resulting volume fraction (V_f) of the $L2_1$ phase.

Phase	Room temperature		845 K		973 K	
	Neutron intensities	I_{L21}/I_{Fe}	Neutron intensities	I_{L21}/I_{Fe}	Neutron intensities	I_{L21}/I_{Fe}
$(220)_{L21}/(110)_{Fe}$						
Fe	188.2 ± 0.5	0.178 ± 0.009	128.0 ± 0.3	0.179 ± 0.009	151.7 ± 0.4	0.184 ± 0.010
$L2_1$	33.6 ± 0.3		22.9 ± 0.2		28.3 ± 0.3	
V_f	22.69 ± 0.03		22.73 ± 0.03		23.47 ± 0.05	

Table 9. A summary of mechanical properties at elevated temperatures of HPSFA, SPSFA, and FBB8, such as tension-yield strength/ductility at 973 K, and creep strength for 100,000 hours at 923 and 973 K. The creep strengths of 0.002C and T122 steels are also included for comparison. All the tension and creep samples of HPSFA, SPSFA, and FBB8 at 973 K were aged at 973 K for 100 hours, while the HPSFA specimens for creep tests at 1,033 K were aged at 1,073 K for 5 hours.

Temperature / Materials	973 K		923 K	973 K
Alloys	Yield strength (MPa)	Ductility (%)	Creep strength (MPa)	Creep strength (MPa)
HPSFA	280	19	164	89
SPSFA	270	23	144	-
FBB8 [55]	120	16	71	-
T122 [81]	-	-	66	18
0.002C [6]	-	-	100	-

Table 10. APT compositions of HPSFA in the solution-treated state. Chemical compositions (in at. %) of constitutive phases in the HPSFA sample solution-treated at 1,473 K for 0.5 hour, followed by air cooling, determined using APT. The uncertainties for APT represent the statistical counting scatter.

Phase	Al	Fe	Ni	Ti	Mo	Cr
$L2_1$	33.95 ± 0.20	18.26 ± 0.20	36.81 ± 0.23	9.75 ± 0.15	0.37 ± 0.01	0.65 ± 0.04
Fe	6.34 ± 0.06	77.20 ± 0.18	1.34 ± 0.04	0.33 ± 0.02	2.26 ± 0.04	12.49 ± 0.12
Secondary precipitate	36.84 ± 0.91	13.34 ± 0.77	42.45 ± 1.08	6.90 ± 0.58	0.09 ± 0.05	0.35 ± 0.13

Table 11. APT compositions of HPSFA in the aged state. Chemical compositions (in at. %) of constitutive phases in the HPSFA sample aged at 973 K for 500 hours after the solution treatment at 1,473 K for 0.5 hour, determined using APT. The uncertainties for APT represent the statistical counting scatter.

Material	Phase	Al	Fe	Ni	Ti	Mo	Cr
Primary precipitate	$L2_1$	30.46 ± 0.37	18.33 ± 0.34	35.25 ± 0.41	14.71 ± 0.31	0.40 ± 0.02	0.55 ± 0.06
	B2	39.88 ± 1.31	14.16 ± 1.00	41.53 ± 1.43	3.59 ± 0.53	0.30 ± 0.09	0.49 ± 0.19
Matrix	Fe	6.94 ± 0.07	76.00 ± 0.17	2.16 ± 0.05	0.43 ± 0.02	1.65 ± 0.03	12.78 ± 0.12
Secondary precipitate	B2	25.61 ± 1.72	42.83 ± 2.26	22.57 ± 1.85	3.09 ± 0.79	0.43 ± 0.06	6.51 ± 1.08

Table 12. Lattice parameters and misfits. Summary of lattice parameters and misfits between the Fe matrix and $L2_1$ phases for the 2-and 4-wt.-%-Ti alloys at room temperature and 973 K.

Temperature (K)	4-wt.-%-Ti alloy			2-wt.-%-Ti alloy		
	α-Fe (Å)	$L2_1$ (Å)	Misfit (%)	α-Fe (Å)	$L2_1$ (Å)	Misfit (%)
300	2.88950 ± 0.000044	5.85269 ± 0.000182	1.26 ± 0.30	2.88851 ± 0.000027	5.80566 ± 0.000591	0.49 ± 0.19
973	2.91921 ± 0.000044	5.91624 ± 0.000182	1.32 ± 0.31	2.91507 ± 0.000037	5.87570 ± 0.000682	0.77 ± 0.28

Table 13. Summary of parameters employed in the elastic-plastic constitutive law. C_{11}, C_{12}, and C_{44}: Elastic constants, n: stress component, q: latent-hardening coefficient in the same set of slip systems, h_0: initial hardening modulus, τ_s: saturated slip strength, and τ_0: initial slip strength.

Material	Phase	C_{11} (MPa)	C_{12} (MPa)	C_{44} (MPa)	τ_0 (MPa)	τ_s (MPa)	n	h_0	q
4-wt. %	Fe	160,000	128,000	92,000	35	157	10	100	1
	$L2_1$	120,000	97,000	56,000	> 200	-	-	-	-
2-wt. %	Fe	160,000	128,000	92,000	50	157	10	500	1
	$L2_1$	120,000	97,000	56,000	> 200	-	-	-	-
	B2	130,000	106,000	70,000	> 200	-	-	-	-

Table 14. Summary of lattice parameters and misfits between the Fe matrix and $L2_1$ phases for the 2-wt.-%-Ti alloy at room temperature up to 973 K.

	Rietveld refinement		
Temperature (K)	α-Fe (Å)	$L2_1$ (Å)	Misfit (%)
300	2.88941	5.82247	0.753
647	2.90151	5.8507	0.818
747	2.90557	5.86175	0.867
847	2.90957	5.87100	0.887
898	2.91193	5.87655	0.901
973	2.91608	5.88631	0.924

Table 15. Step-loading conditions (applied stress, time duration, and accumulated macroscopic strain) of the in-situ tension-creep experiment and Young's modulus calculated from the macroscopic stress-strain curve during each loading.

Stress level (MPa)	Time duration (hours)	Minimum strain rate (sec^{-1})	Accumulated strain (%)	Young's modulus (GPa)
100	2	5.09×10^{-9}	0.10	110.5
150	4	9.11×10^{-9}	0.18	111.1
190	15	2.42×10^{-8}	0.48	100.0
220	10	3.41×10^{-7}	2.5	83.3
235	1	-	8.8 (fracture)	46.9

Table 16. Summary of parameters employed in the elastic-plastic constitutive law. C_{11}, C_{12}, and C_{44}: Elastic constants, n: stress component, q: latent-hardening coefficient in the same set of slip systems, h_0: initial hardening modulus, τ_s: saturated slip strength, τ_0: initial slip strength, and α: slip-system number.

Parameter / Phase	C_{11} **(MPa)**	C_{12} **(MPa)**	C_{44} **(MPa)**	**n**	**q**	h_0 **(MPa)**	τ_s **(MPa)**	τ_0 **(MPa)**	α **(/°c)**
Fe	113,800	96,000	51,100	10	1.0	100	157	120	1.66 e-6
NiAl	166,700	124,900	111,500	10	1.0	100	1,300	1,000	3.56 e-6
Ni_2TiAl	152,000	103,900	94,000	10	1.0	10	1,400	1,100	3.79 e-6

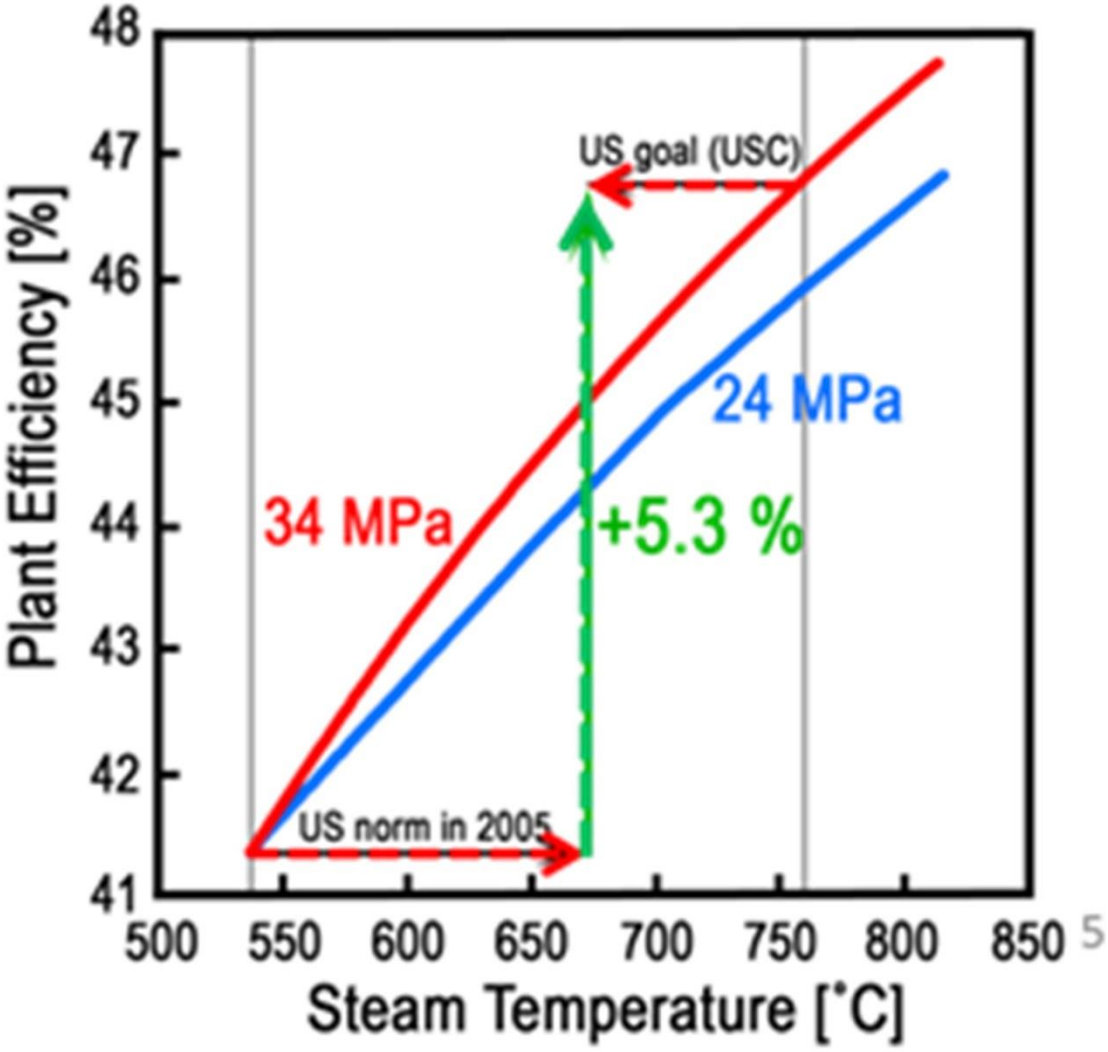

Figure 1. A graph showing the improvements in the plant efficiency achieved by increasing the steam temperature and pressure.

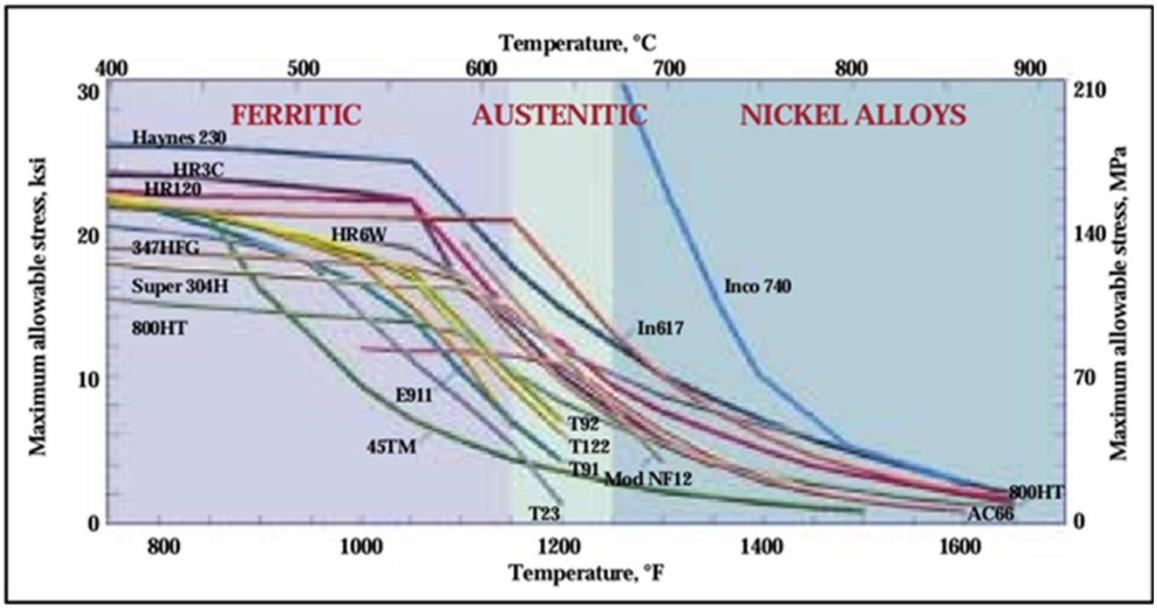

Figure 2. Allowable stresses for various classes of alloys [13].

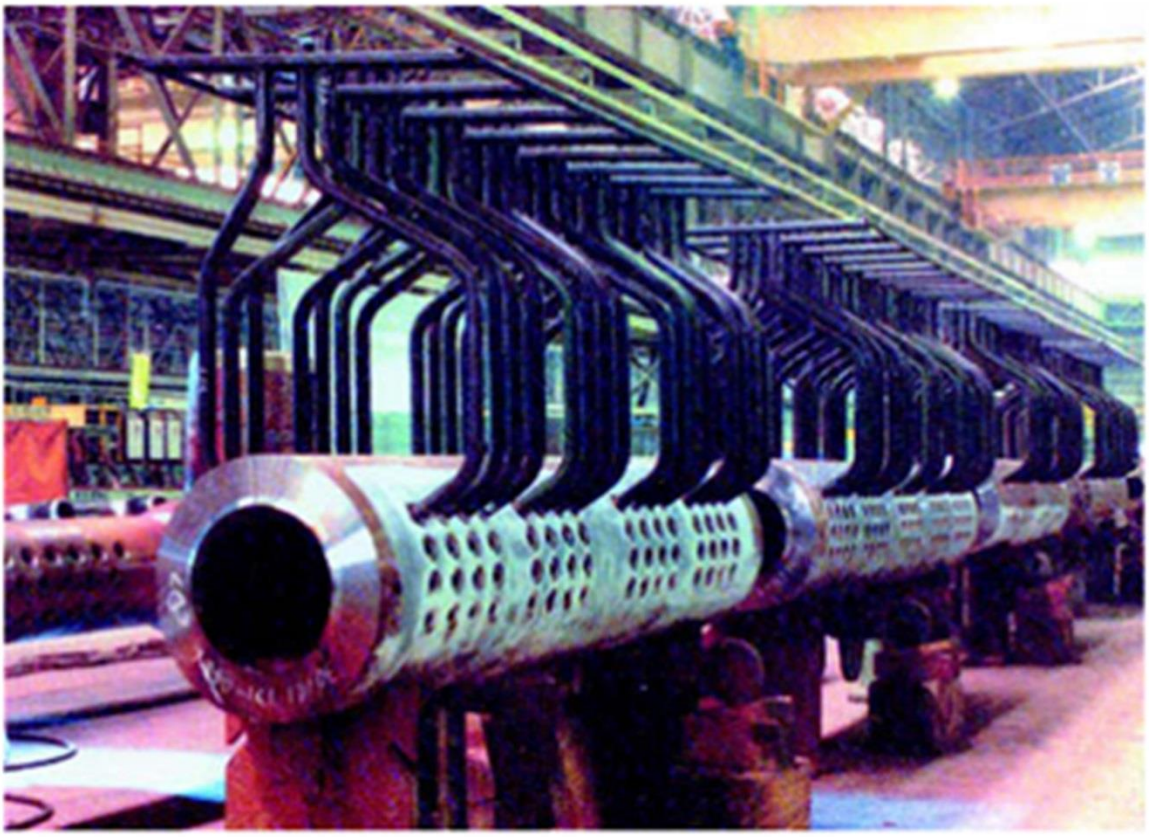

Figure 3. Illustration of a header [12].

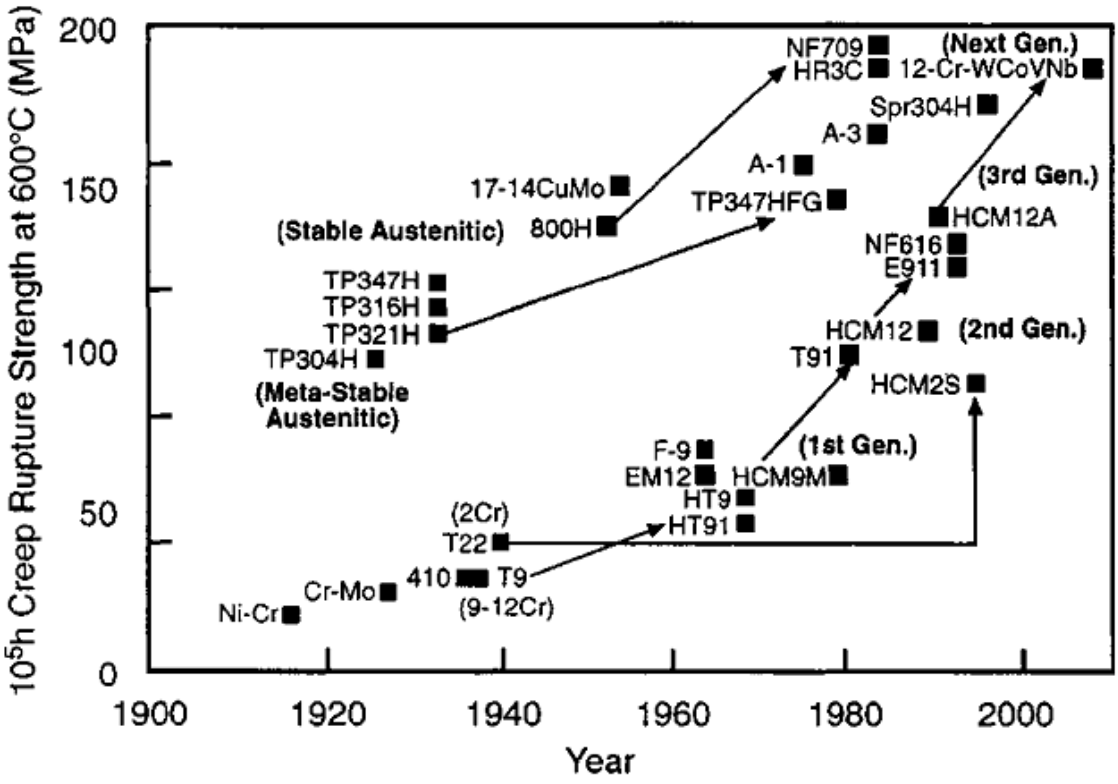

Figure 4. Historic evolution of materials in terms of increasing creep-rupture strength [15].

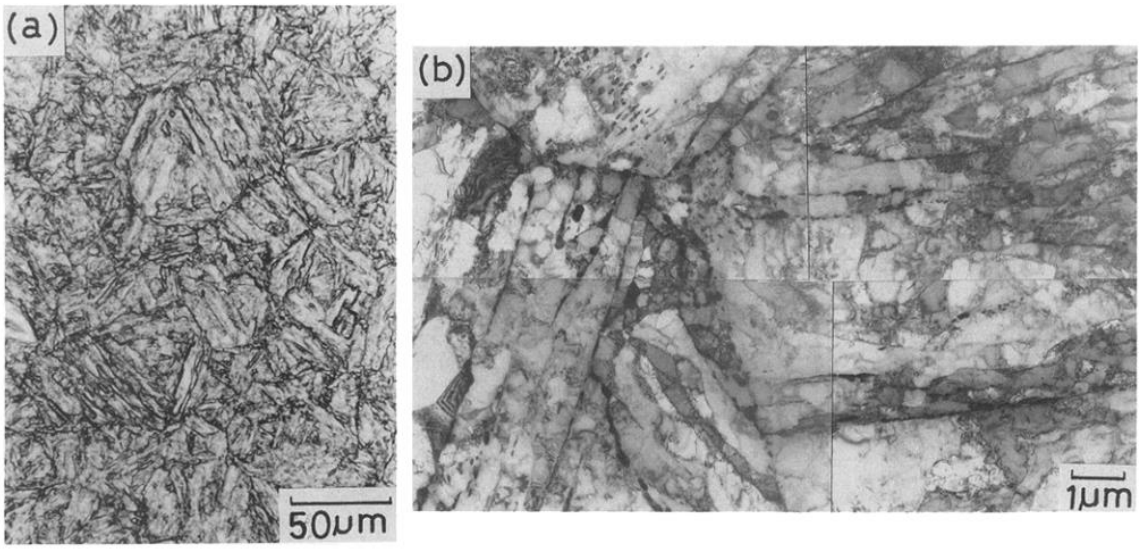

Figure 5. Microstructures of 9Cr-2W (weight percent) steel after tempering: (a) optical and (b) transmission-electron micrographs [18].

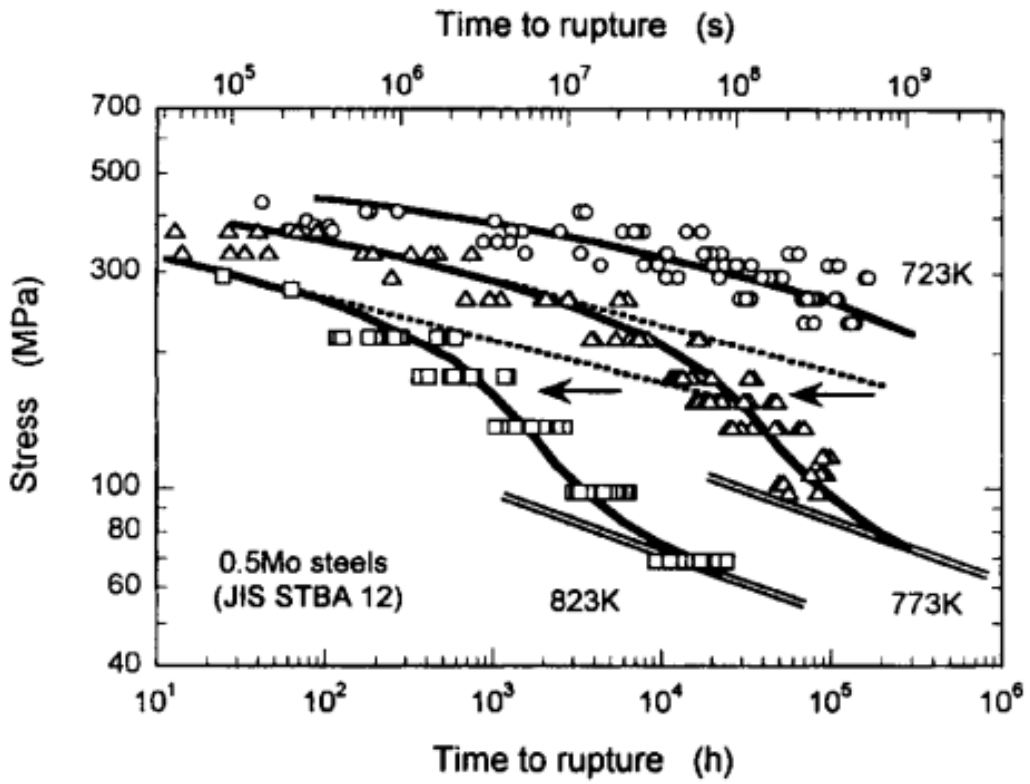

Figure 6. Creep-rupture curves for 0.5Mo steels showing sigmoidal shape of curves [19].

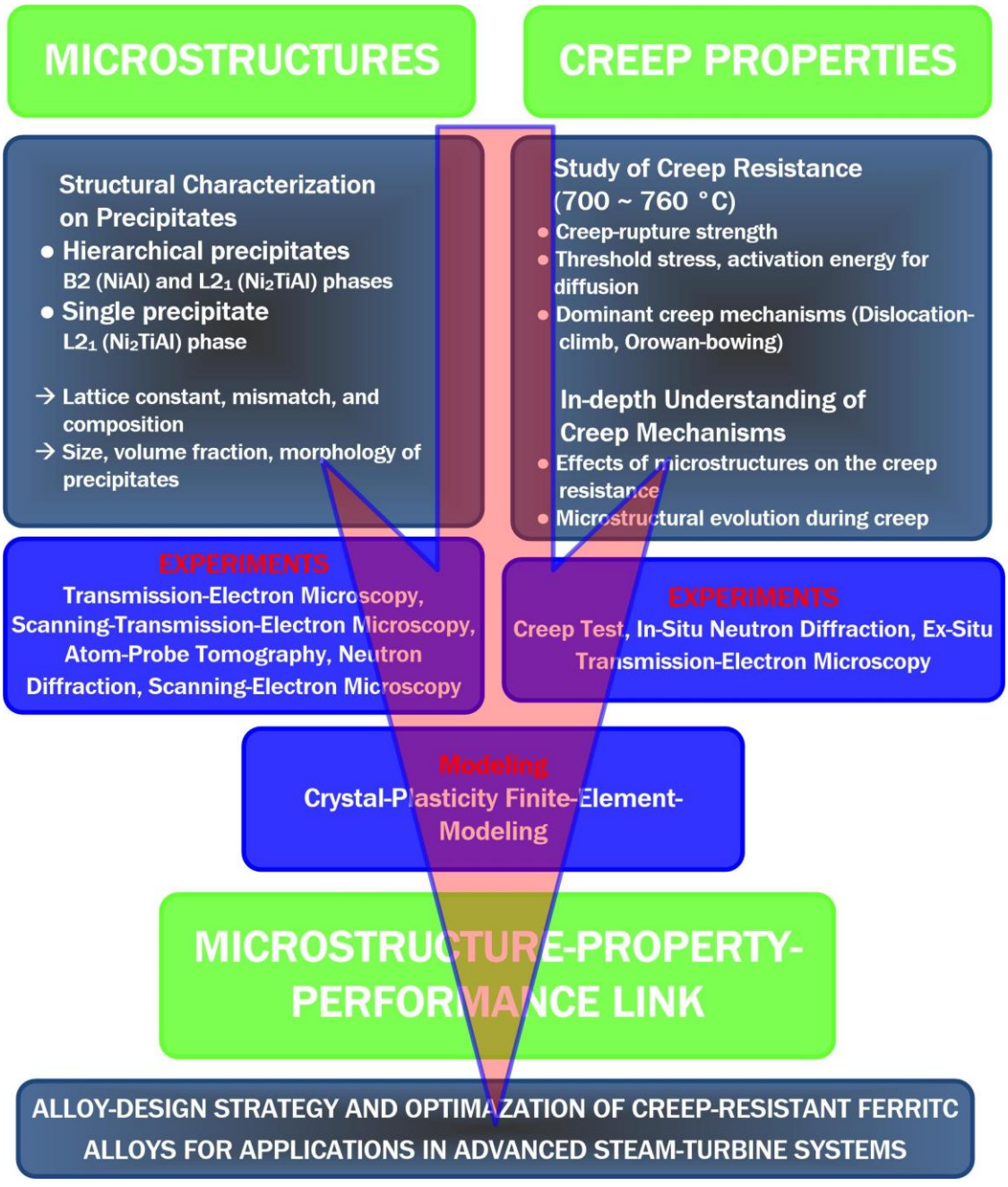

Figure 7. A schematic illustration of the proposed research.

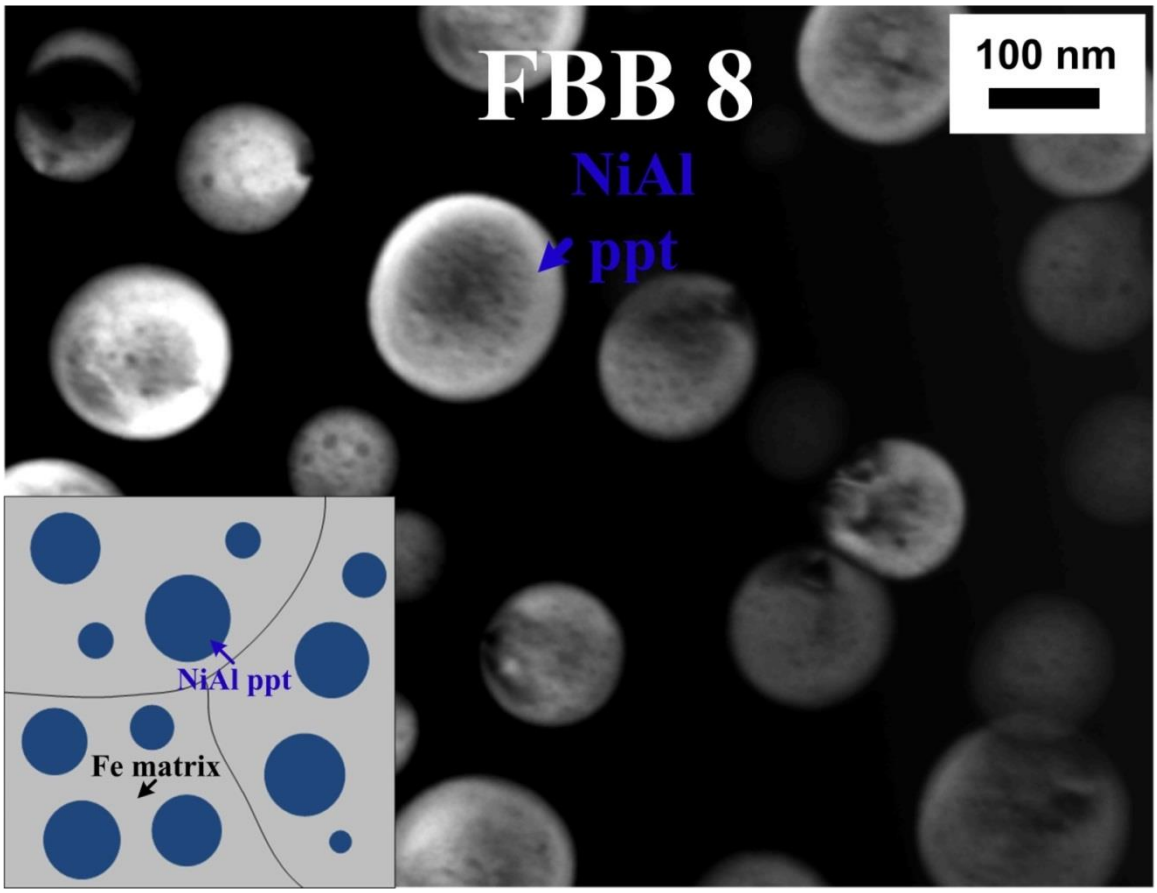

Figure 8. Dark-field (DF) transmission-electron-microscopy (TEM) images showing the microstructures of FBB8 and a schematic in the inset illustrating the microstructures of FBB8.

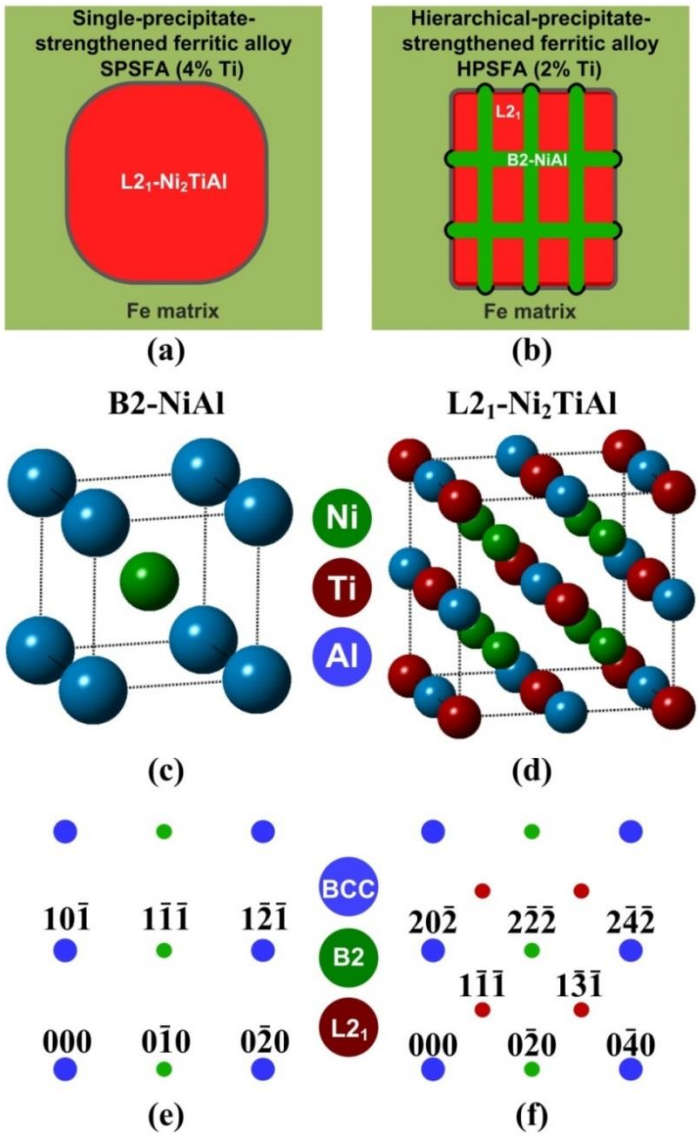

Figure 9. Schematic illustration of the microstructures of SPSFA and HPSFA and electron-diffraction patterns of B2 and $L2_1$ phases. Schematic illustrations of (a) the single-phase $L2_1$-Ni_2TiAl-precipitate and (b) two-phase hierarchical B2-NiAl/$L2_1$-Ni_2TiAl-precipitate structures. Crystal structures for (c) the B2-NiAl and (d) $L2_1$-Ni_2TiAl, and Ni atoms are colored in green, Al atoms in blue, and Ti atoms in red. Corresponding electron-diffraction patterns along the [101] zone axis for (e) the B2-NiAl and (f) $L2_1$-Ni_2TiAl.

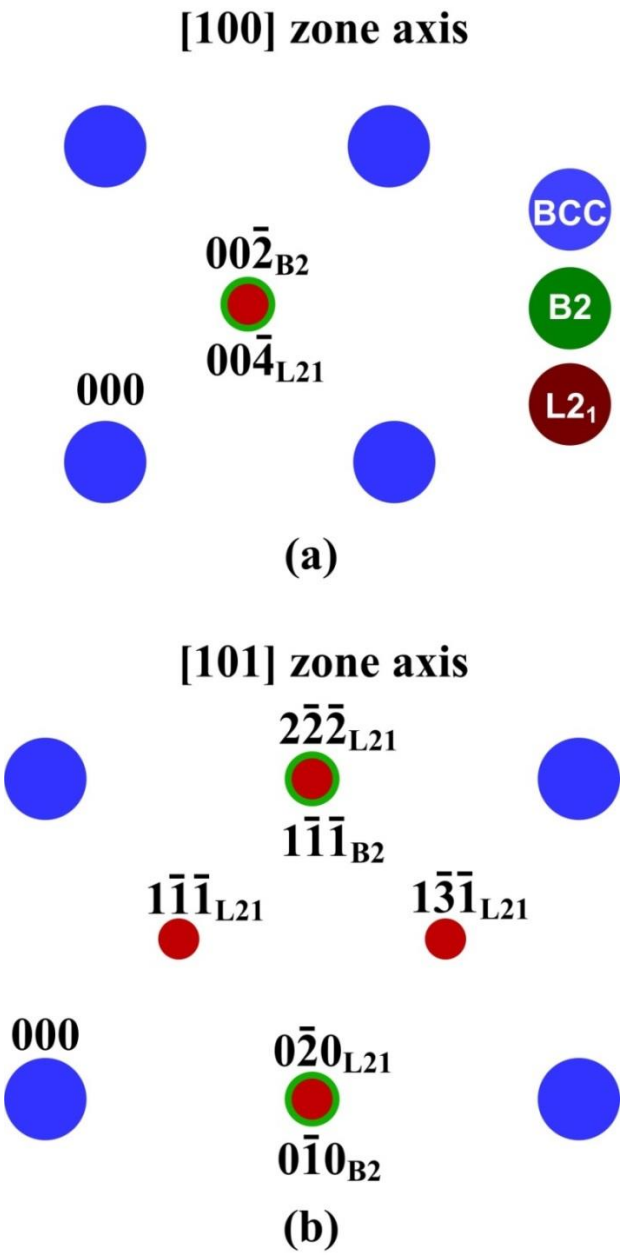

Figure 10. Schematic illustration of electron-diffraction patterns of B2 and $L2_1$ phases. Electron-diffraction patterns based on the coexistence of both B2-NiAl and $L2_1$-Ni_2TiAl phases along (a) the [100] and (b) [101] zone axes. Blue, green, and red spots represent the fundamental, B2-, and $L2_1$-superlattice reflections, respectively. Note that the larger size of the superlattice spot indicates the higher intensity (contrast) of the reflections.

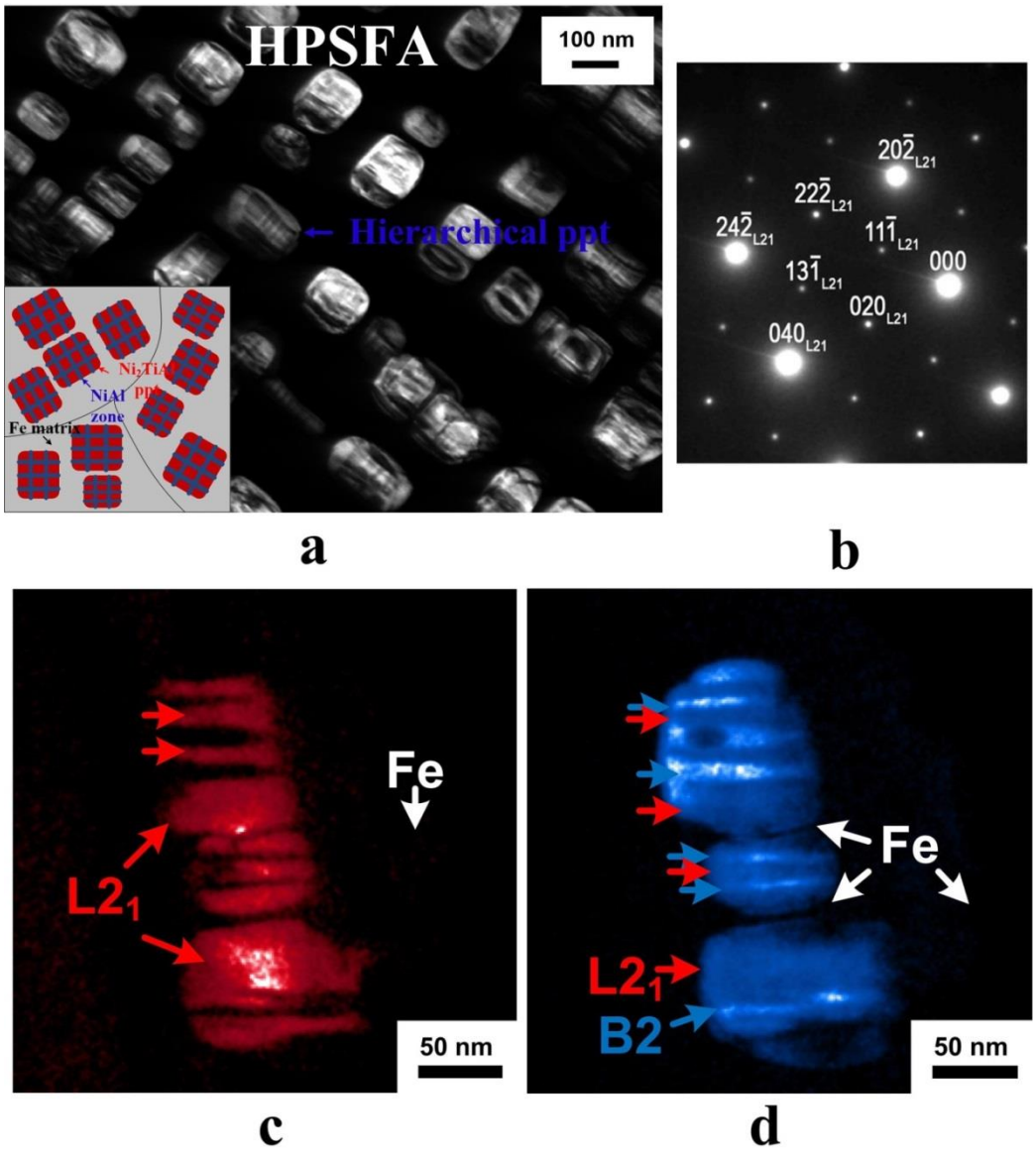

Figure 11. (a) Dark-field (DF) transmission-electron-microscopy (TEM) images showing the microstructures of HPSFA, (b) a selected-area-diffraction-pattern, (c) and (d) false color dark-field (DF)-TEM images acquired along the [101] zone axis from the same region, using (c) <111> and (d) <020> super-lattice reflections, respectively, for the HPSFA alloy subjected to the solution treatment at 1,473 K for 30 minutes, followed by aging at 973 K for 100 hours.

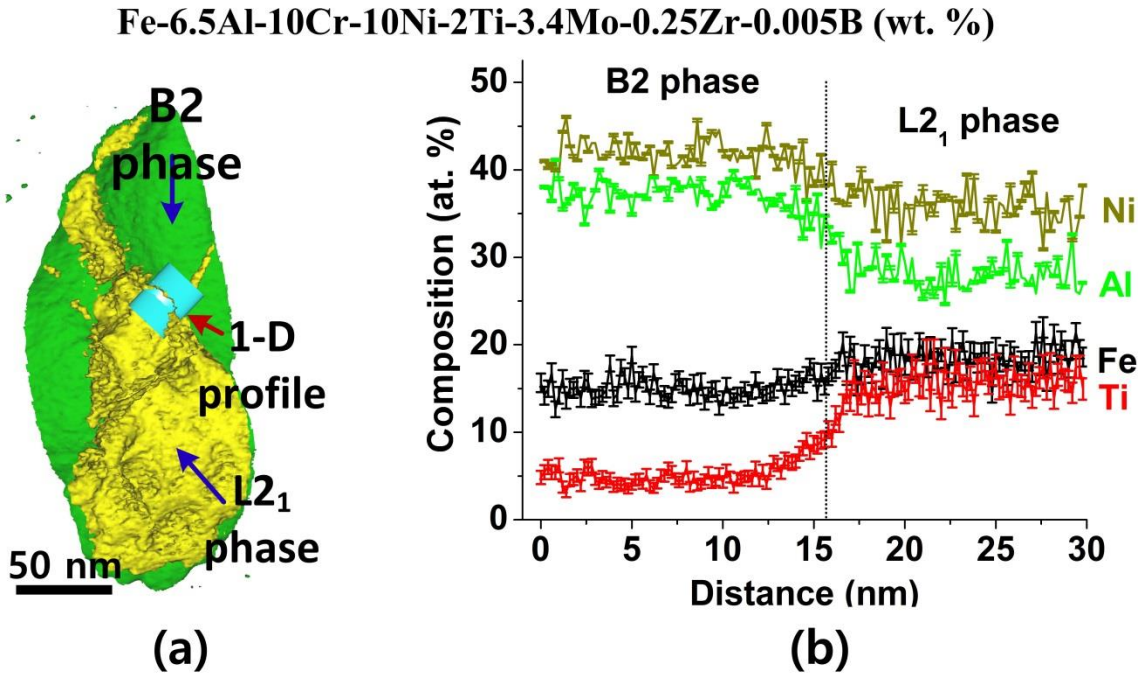

Figure 12. Atom-probe-tomography (APT) results of the B2 and $L2_1$ phases in the primary precipitate, (a) iso-concentration surfaces of 10-at.-% Ti (yellow) and 10-at.-% Ni (green), and (b) a composition profile of the B2 and $L2_1$ phases along the 1-D profile in (a)

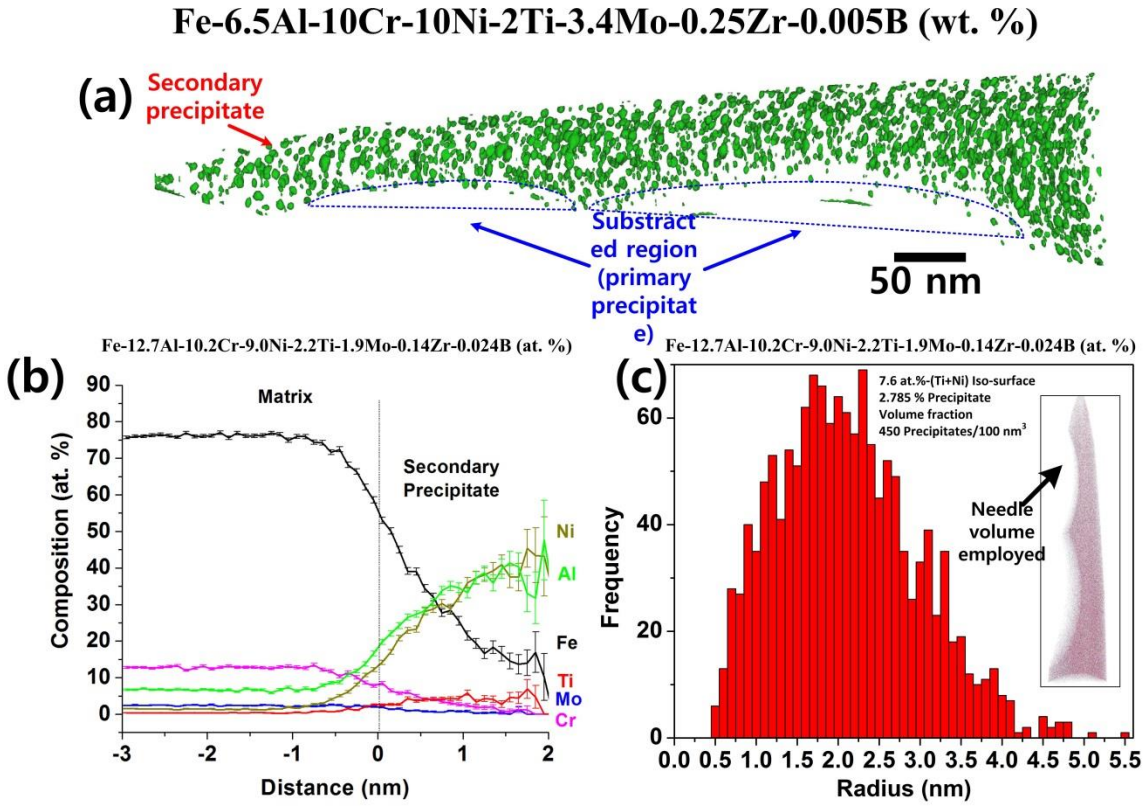

Figure 13. APT results from the secondary precipitates: (a) a 7.6-at.-% (Ni + Ti) iso-concentration surface (green), (b) composition profile between the matrix and secondary precipitate, and (c) histogram for the size distribution of the secondary precipitates with an inset of the needle volume employed to acquire the size distribution.

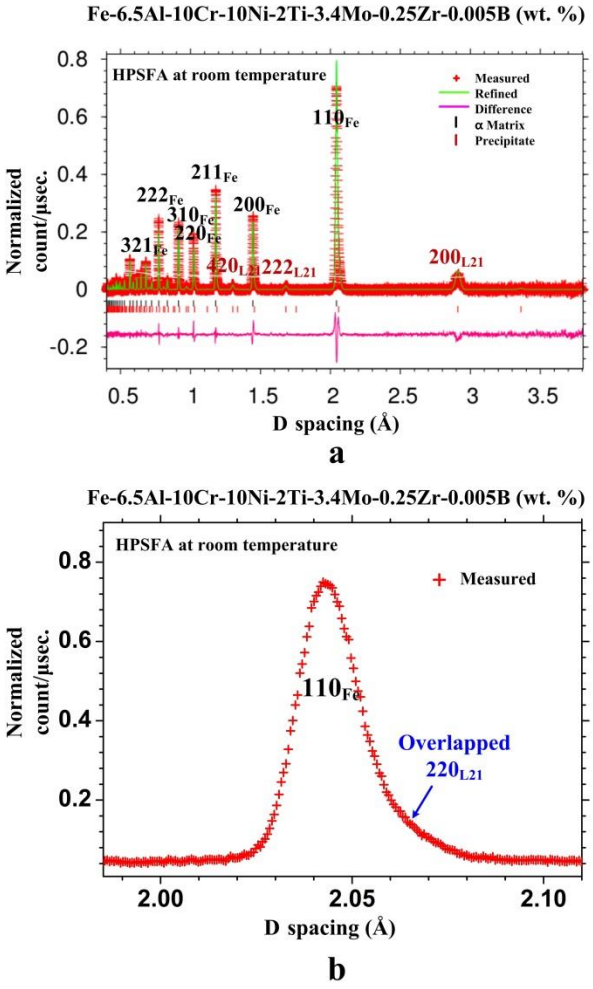

Figure 14. Representative neutron-diffraction patterns (intensity vs. D spacing; plane distance) of HPSFA measured at room temperature without loading. (b) Enlarged pattern clearly exhibits overlapped fundamental (110)Fe and (220)$L2_1$ peaks for HPSFA. The red cross represents the measured data. The green curve is the fitted profile using the General Structure Analysis System (GSAS) Rietveld analysis. The pink curve presents the difference between the fitted profile and measured data. The red and black toggles below the patterns represent the peak positions of the $L2_1$ and BCC-Fe phases, which are determined by the phase information in the GSAS program, such as the space group and lattice parameter, respectively.

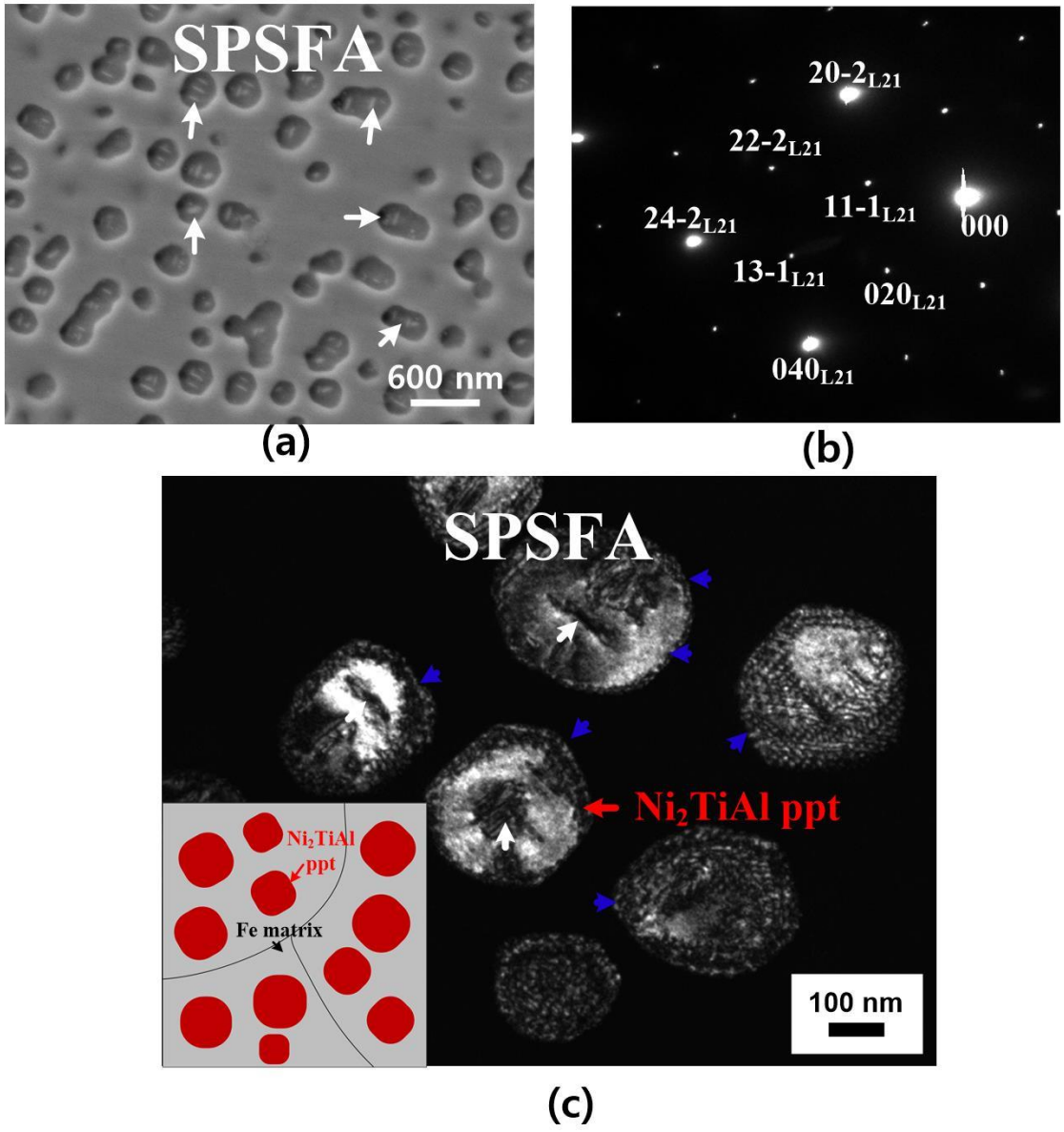

Figure 15. (a) Secondary-electron microscopy (SEM), (b) a selected-area-diffraction-pattern (SADP) of the [110] zone axis, and (c) dark-field transmission-electron microscopy (DF-TEM) images of the Ni_2TiAl-strengthened ferritic alloy aged at 973 K for 100 hours after the solution treatment at 1,473 K for 0.5 hour.

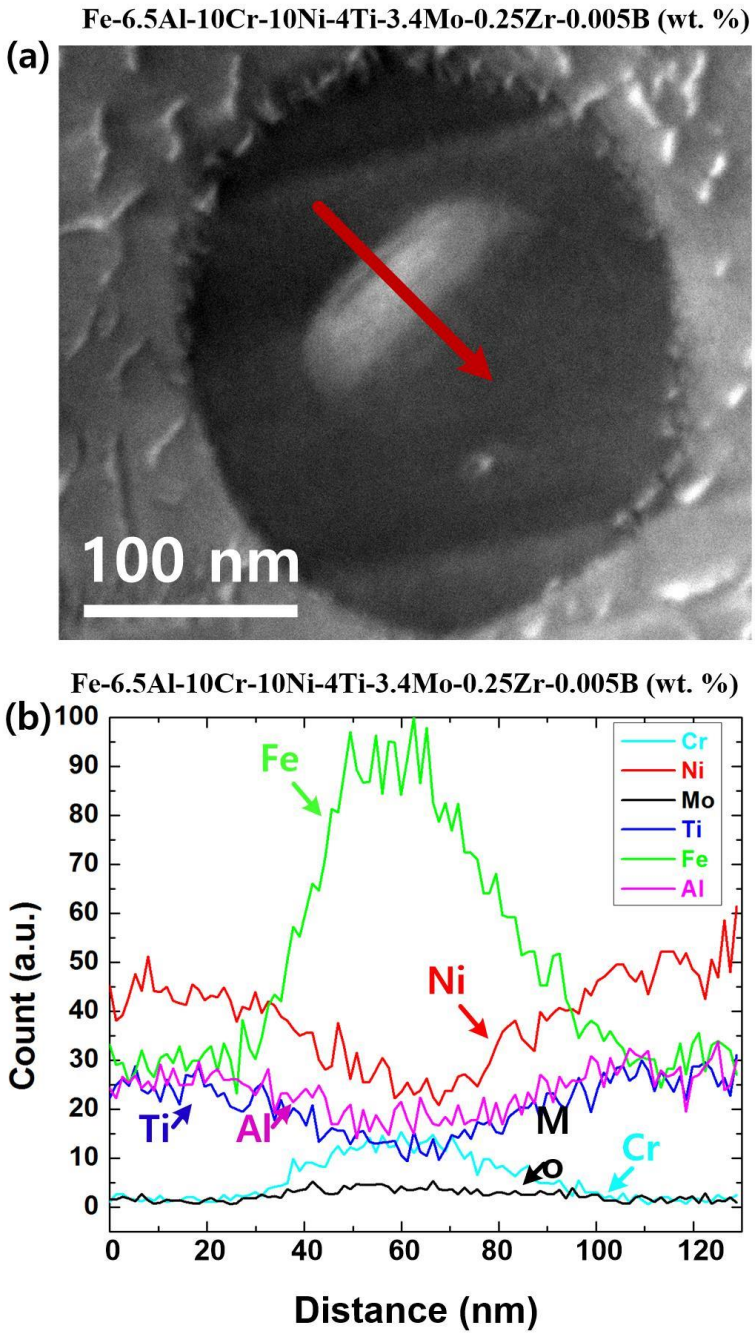

Figure 16. (a) A high-angle annual dark-field (HAADF) scanning-transmission-electron micrograph (STEM) of the Ni_2TiAl-strengthened ferritic alloy, taken along the [110] zone axis, and (b) an energy-dispersive X-ray spectroscopy (EDS) line profile of constitutive elements along the red line in Figure 16(a).

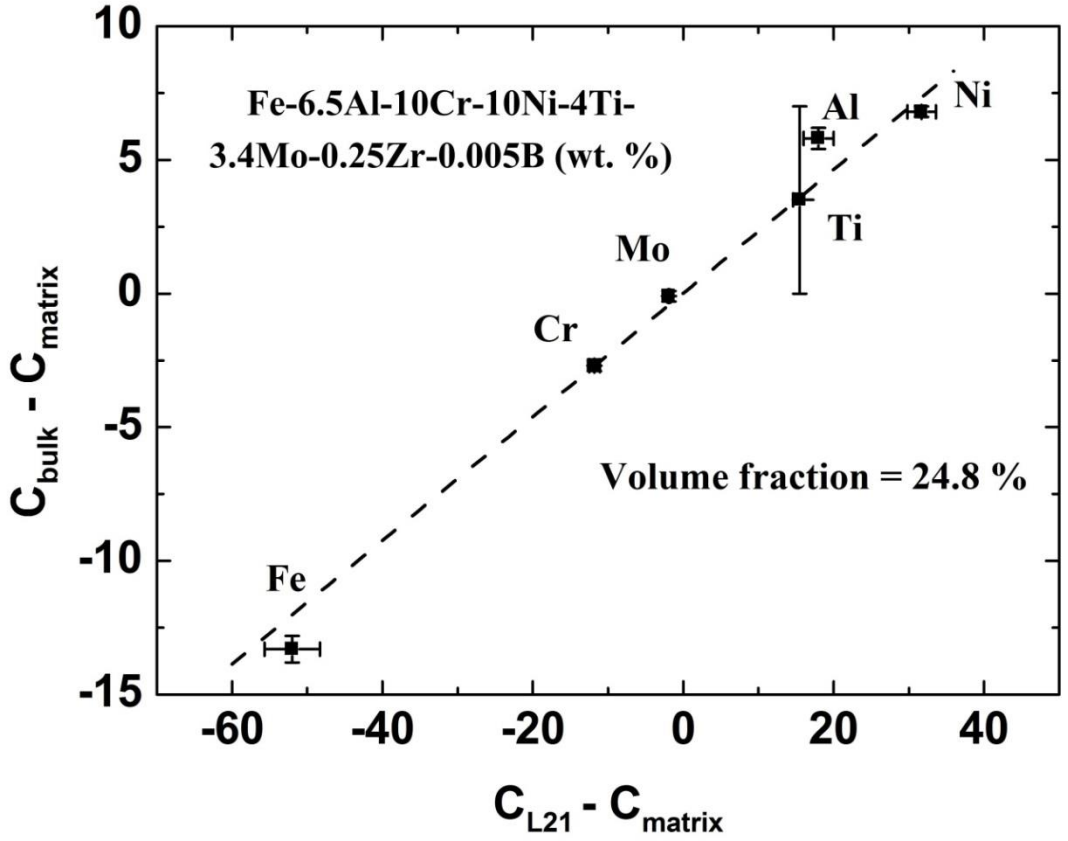

Figure 17. A plot of ($C_{bulk} - C_{matrix}$) vs. ($C_{L21} - C_{matrix}$) to calculate the volume fraction of the $L2_1$-type precipitate, based on the transmission-electron-microscopy energy-dispersive X-ray spectroscopy (TEM-EDS) analysis in Table 4.

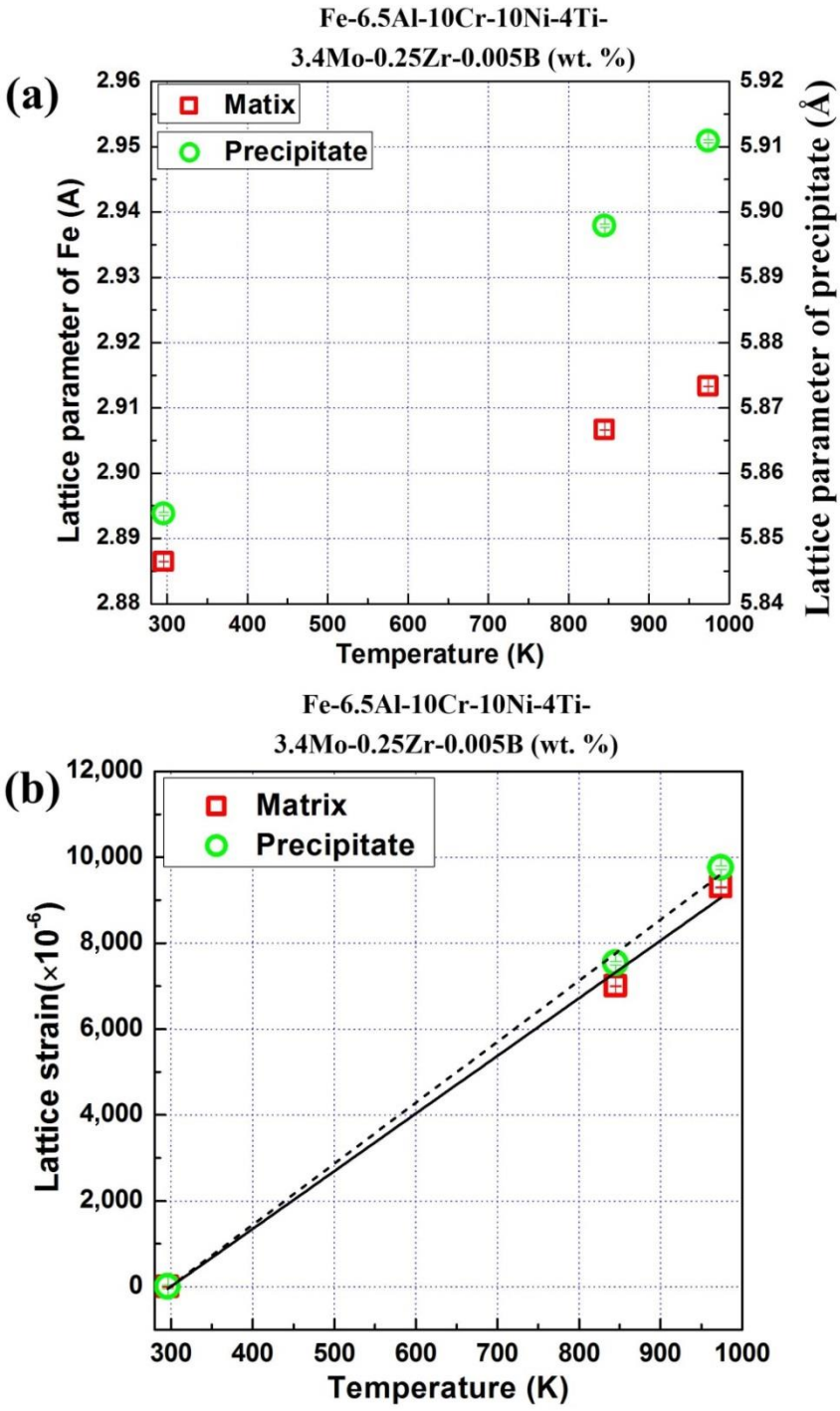

Figure 18. Plots of (a) lattice parameters and (b) thermal lattice strains of the Fe matrix and Ni_2TiAl precipitate as a function of temperature.

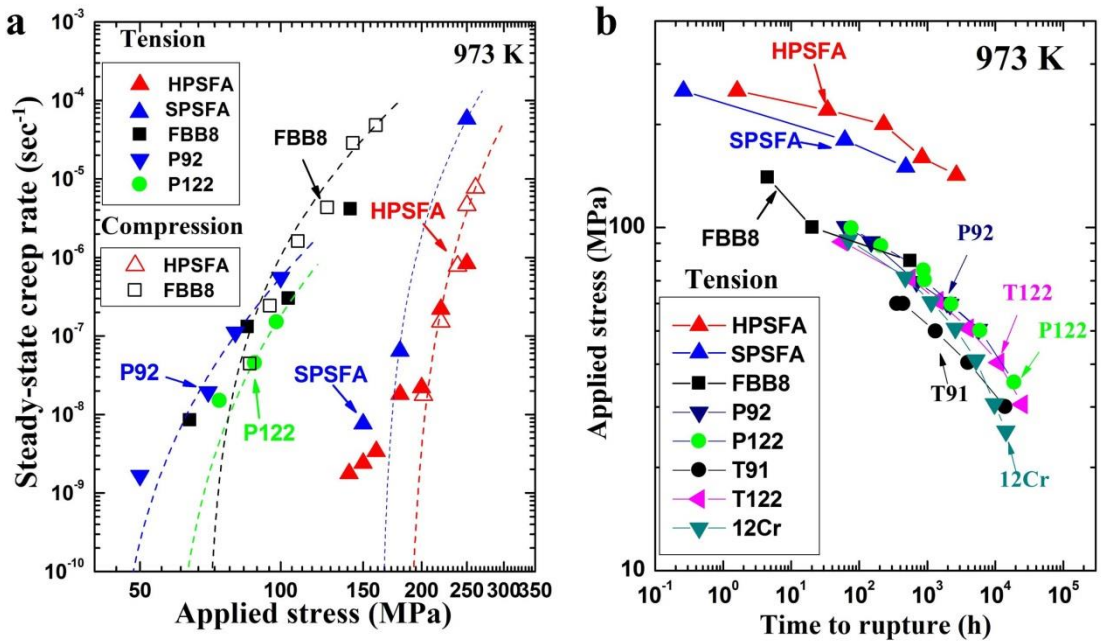

Figure 19. Comparison of the creep resistance of the precipitates-strengthened ferritic alloys. (a) A plot of the steady-state creep rate versus applied stress for HPSFA, SPSFA, FBB8, and commercial ferritic steels (P92 and P122) from compression and tension creep tests at 973 K, and best-fit curves obtained from a linear least-squares regression of $\dot{\varepsilon}^{1/n}$ vs. $\sigma_a - \sigma_{th}$ with n = 4 are also indicated. (b) A plot of the applied stress versus time to rupture at 973 K on the log-log basis for HPSFA, SPSFA, FBB8, and commercial ferritic steels (P92, P122, T91, T122, and 12Cr).

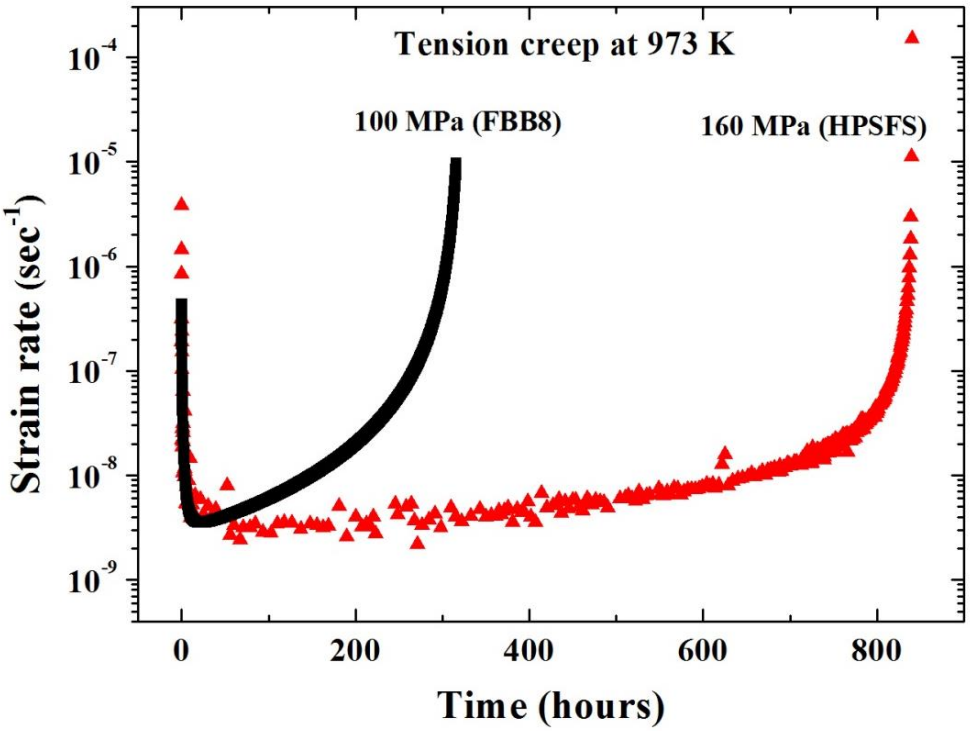

Figure 20. Comparison of the creep behavior between FBB8 and HPSFA. Creep-strain-rate versus time at 973 K, 100 MPa for FBB8 and 160 MPa for HPSFA, respectively. It can be observed that the creep-deformation process of HPSFA is composed of the well-defined secondary-creep region, while an extended tertiary creep accounts for much of the creep life in FBB8 after the primary creep where the creep rate gradually decreases.

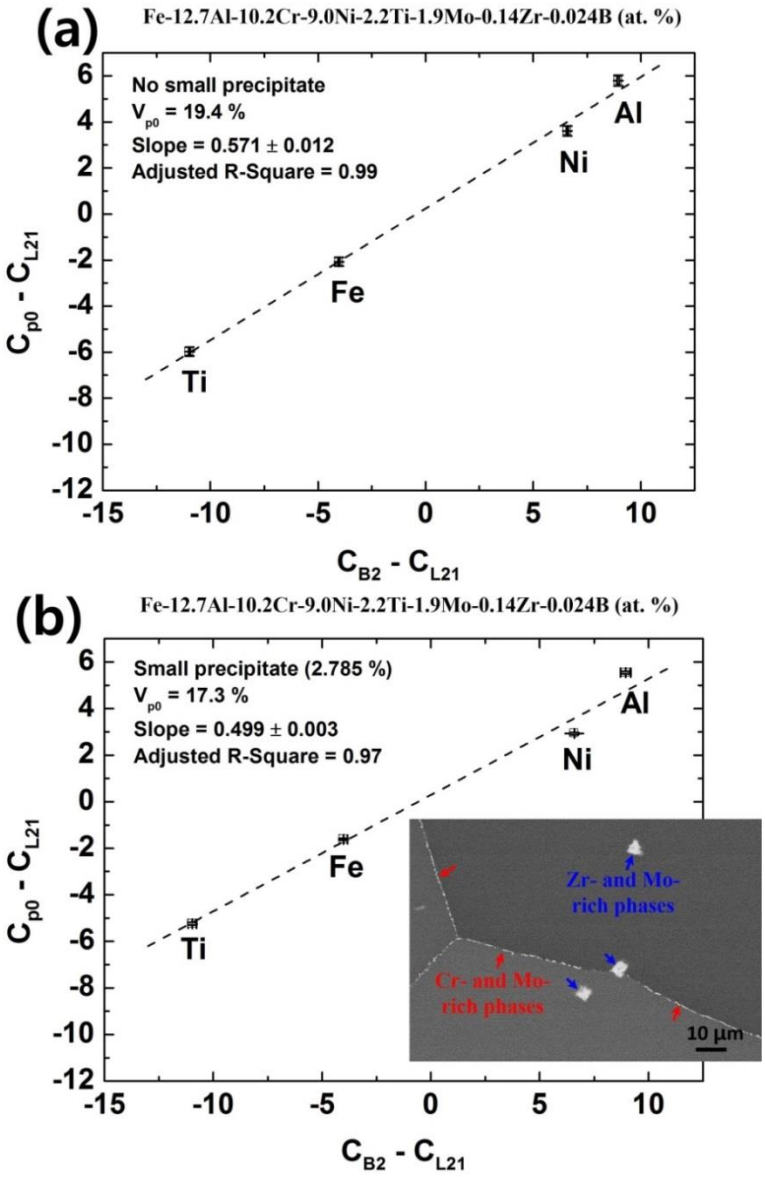

Figure 21. A plot of (C_{po} - C_{L21}) vs. (C_{B2} - C_{L21}) used to calculate the volume fractions of B2 and $L2_1$ phases within the primary precipitate by (a) ignoring the secondary precipitate and (b) considering the secondary precipitate. The volume fraction of the primary precipitate (V_{po}), which gives the best linear fit, is indicated on each plot. An inset scanning-electron-microscopy (SEM) image in (b) shows Mo-, Cr-, and Zr-rich phases.

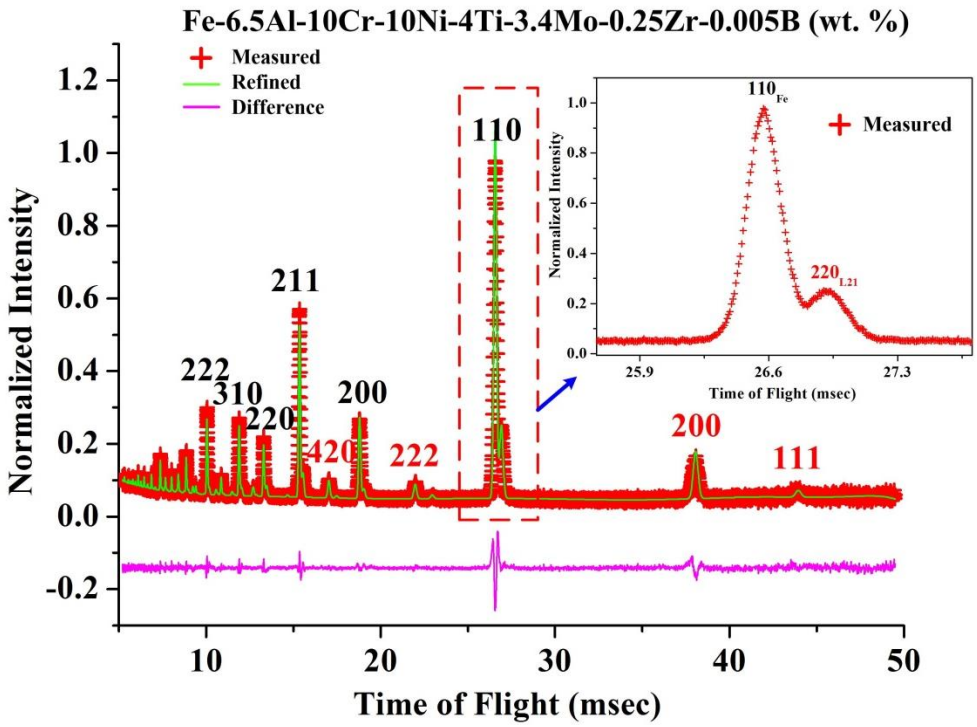

Figure 22. Representative neutron-diffraction pattern of SPSFA measured at room temperature without loading. An enlarged pattern in the inset clearly exhibits well-separated $(110)_{Fe}$ and $(220)_{L21}$ peaks. The red cross represents the measured data. The green curve is the fitted profile, using the General Structure Analysis System (GSAS) Rietveld analysis. The pink curve presents the difference between the fitted profile and measured data.

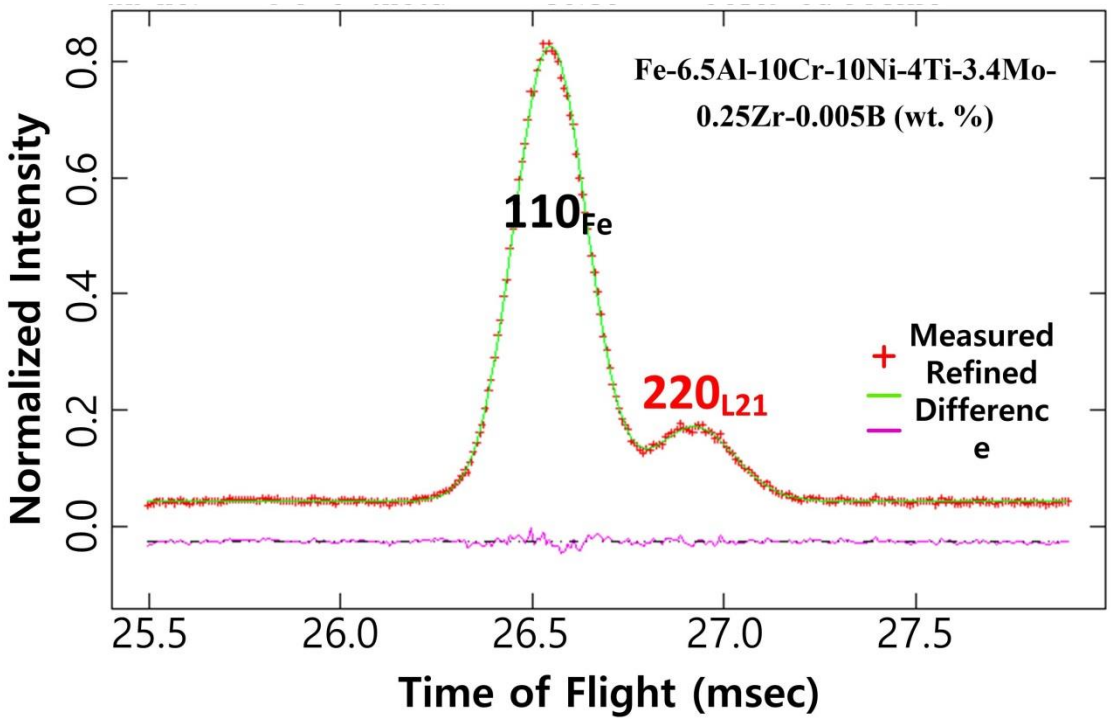

Figure 23. Single-peak-fitting (SPF) result on a partially-overlapped $(110)_{Fe}/(220)_{L21}$ peaks at room temperature. The red cross represents the measured data. The green curve is the fitted profile, using the General Structure Analysis System (GSAS). The pink curve presents the difference between the fitted profile and measured data.

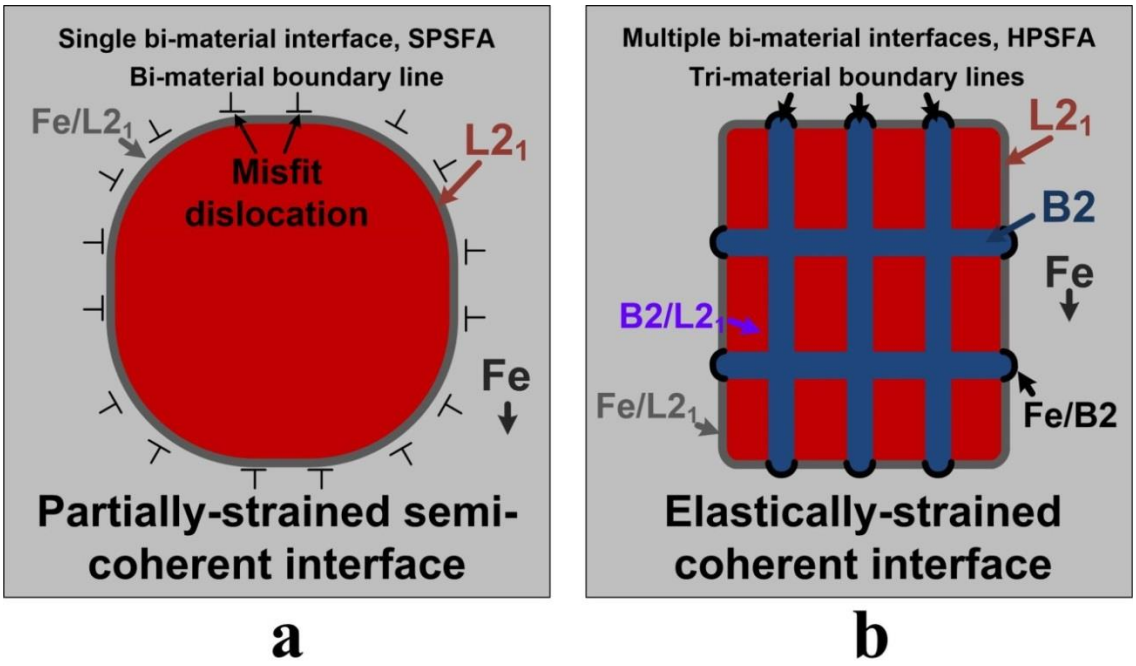

Figure 24. Schematics illustrating the distinct strain fields of the as-aged microstructure before creep deformation, depending on the interface structures of the precipitates. (a) A single bi-material precipitate-matrix interface of SPSFA. (b) Multiple tri-material interfaces within the precipitate and between the precipitate and matrix of HPSFA.

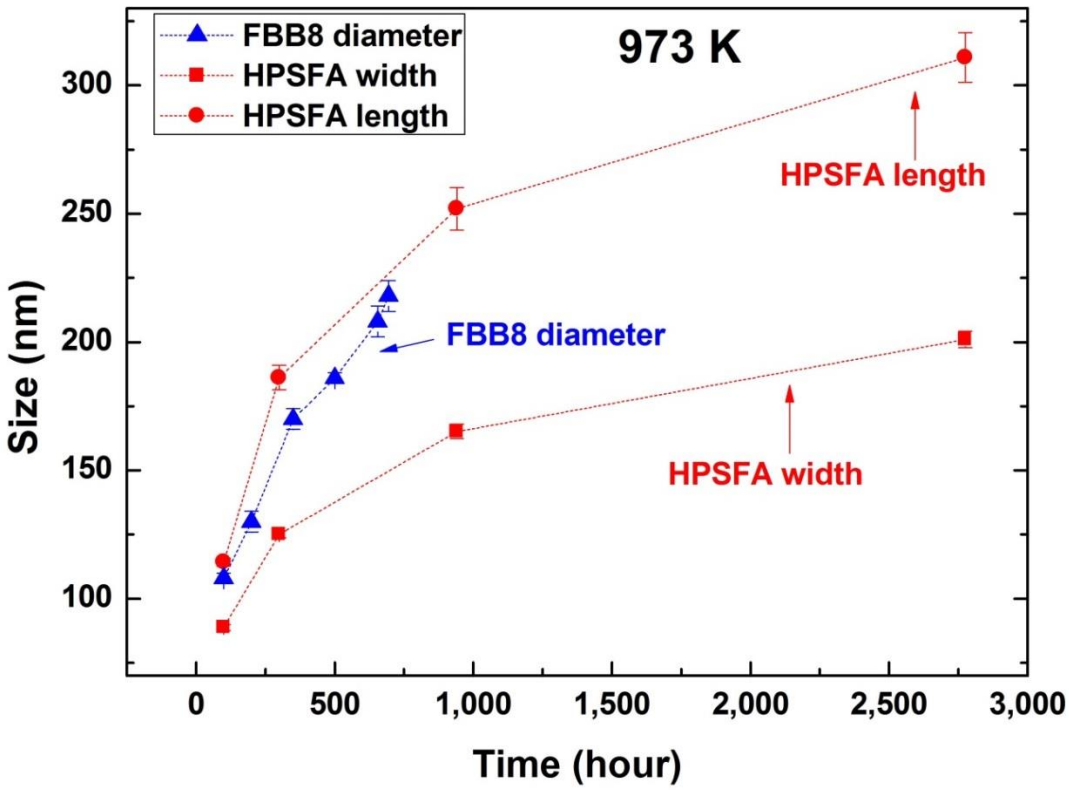

Figure 25. Temporal evolution of the precipitate sizes of HPSFA and FBB8 at 973 K. Note that the HPSFA specimens were aged at 973 K for 100 hours, followed by creep tests, and the precipitate sizes of HPSFA were derived from the grip sections of the crept samples at 973 K (no stress). The FBB8 specimens were aged at 973 K as a function of time. Since the precipitate of HPSFA is of an elongated shape, the width and length of the precipitate were separately determined. In contrast, since the precipitate of FBB8 has a spherical morphology, the diameter of the precipitate was employed.

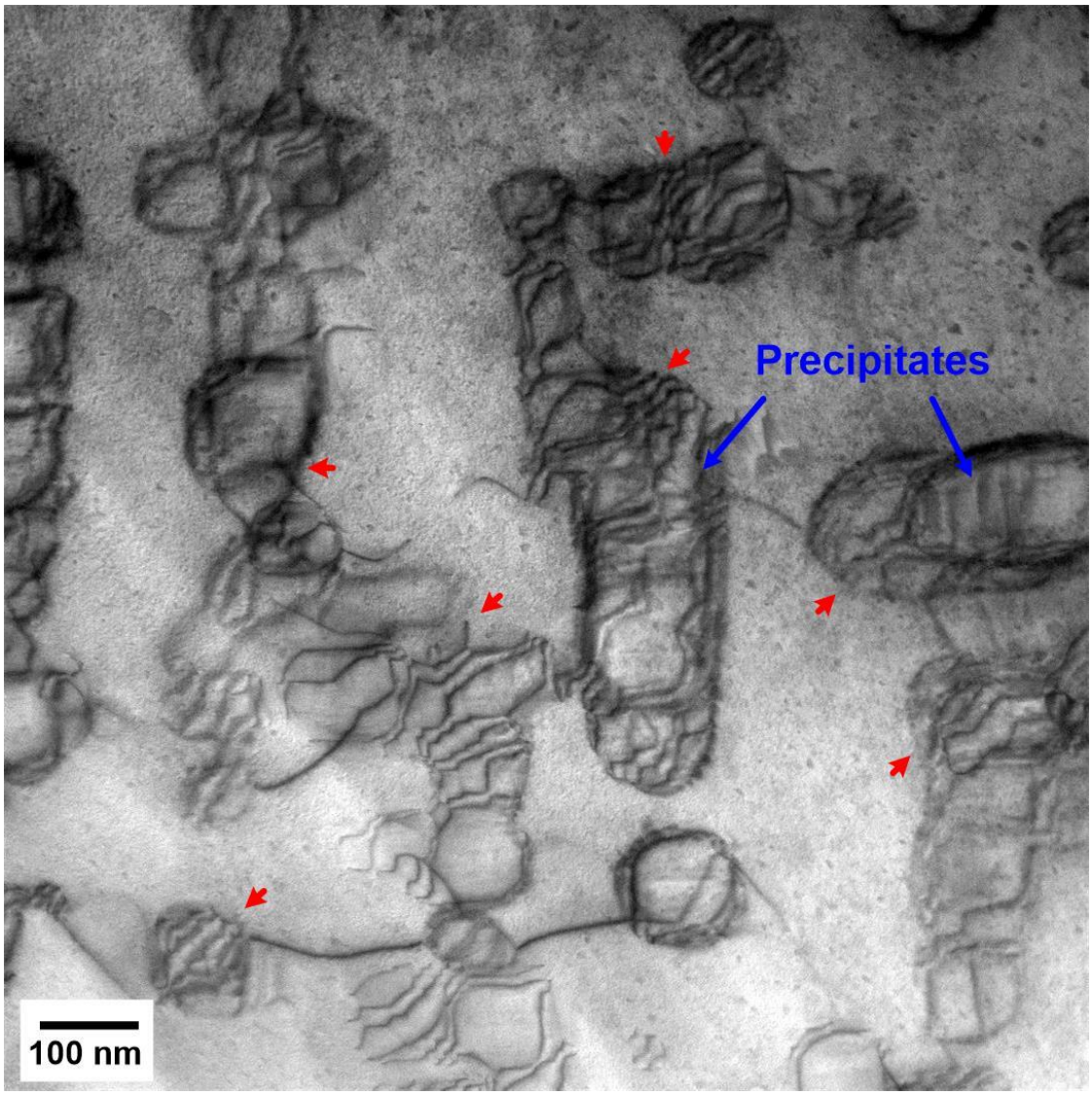

Figure 26. STEM image on the crept HPSFA. A bright-field (BF) scanning-transmission-electron-microscopy (STEM) image of an HPSFA sample crept at 140 MPa and 973 K, which was interrupted by cooling down to room temperature under the applied stress at the creep time of 200 hours (red arrows: dislocations, blue arrows: precipitates).

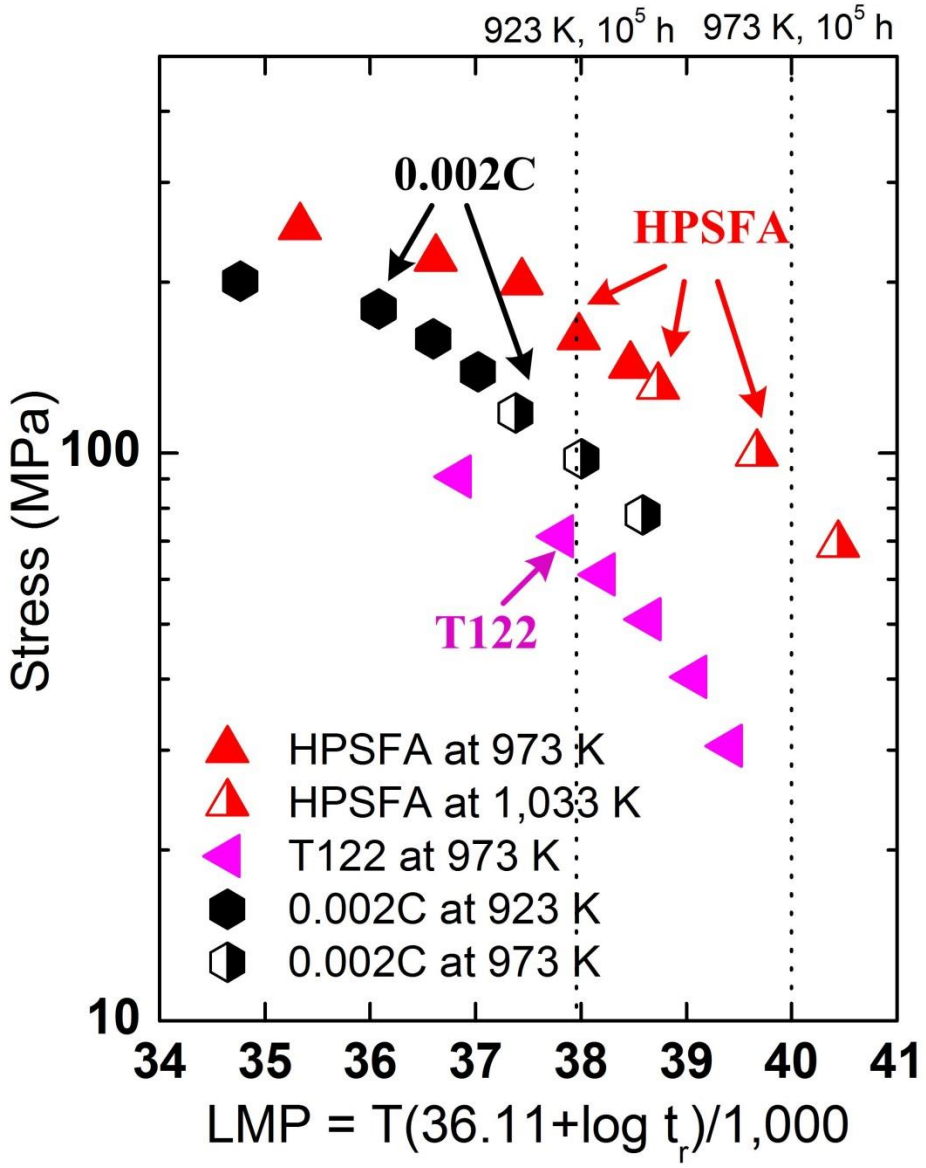

Figure 27. The determination of creep strengths with Larson-Miller parameter. Larson-Miller plot for HPSFA, T122, and 0.002C steels, the LMP values at 923 and 973 K for 100,000 hours are indicated by dotted lines in the plot. (T122: Fe-10.65Cr-1.87W-0.86Cu-0.6Mn-0.33Mo-0.31Si-0.36Ni-0.19V-0.13C-0.057N-0.05Nb-0.007Al-0.0024B, and 0.002C: Fe-9.0Cr-3.0W-3.0Co-0.2V-0.06Nb-0.002C in weight percent)

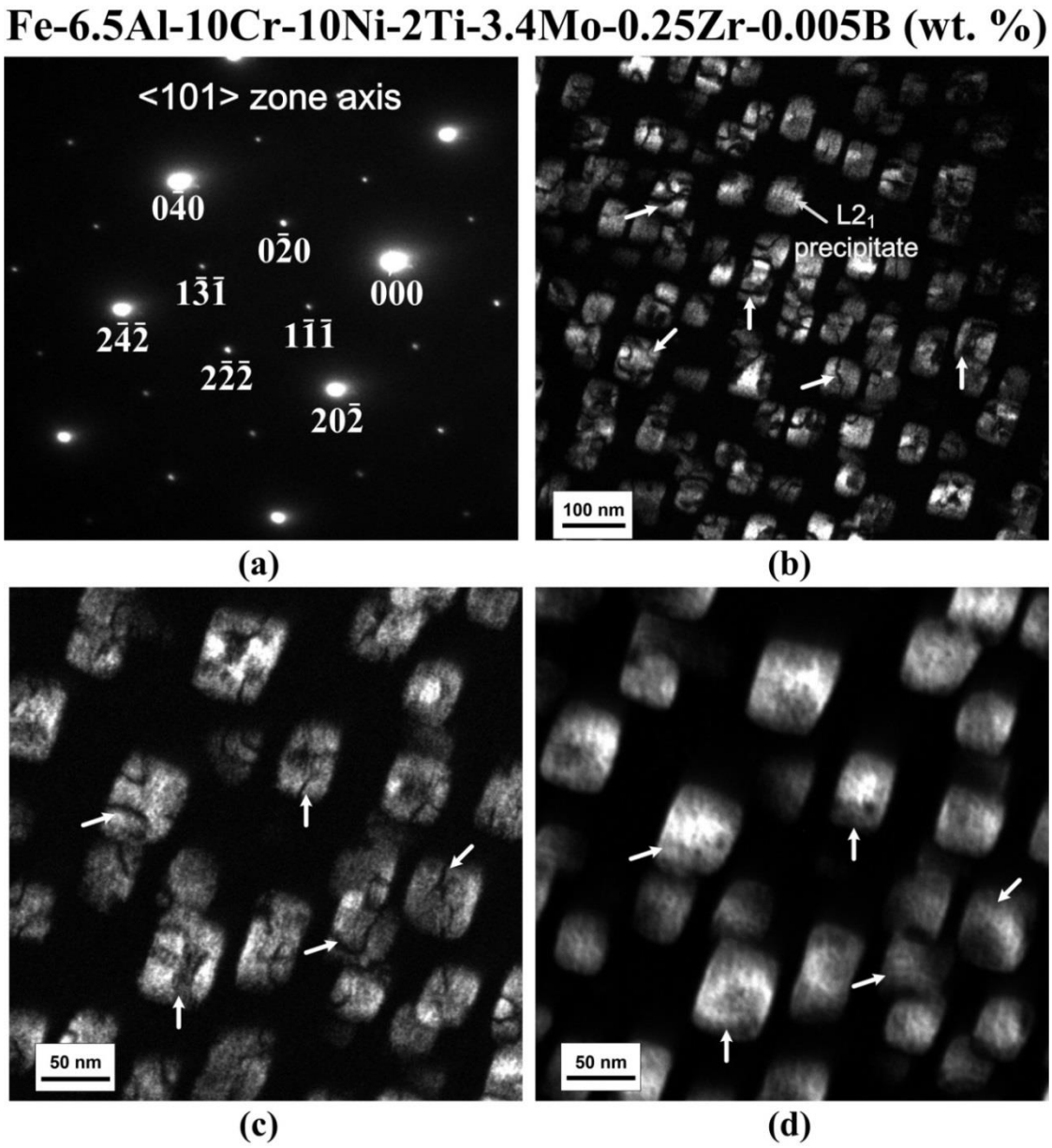

Figure 28. The microstructure of the 2-wt.-%-Ti alloy solution treated sample at 1,473 K for 0.5 hour, followed by air-cooling. (a) Selected area diffraction pattern along the (101) zone axis, (b)-(d) dark-field (DF) transmission-electron microscopy (TEM) images using (b)-(c) the <111> reflection and (d) the <222> reflection.

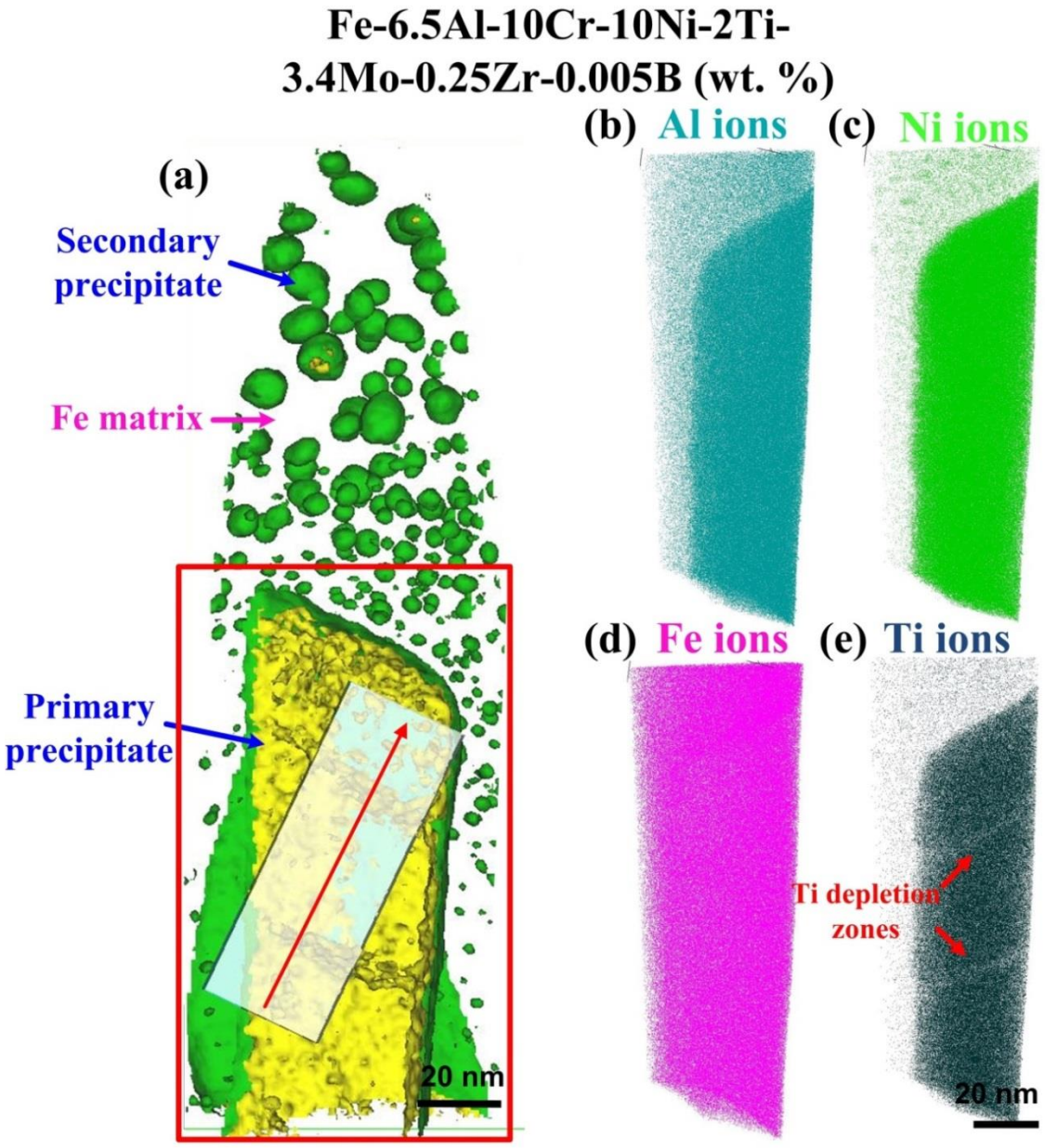

Figure 29. Atom-probe-tomography (APT) characterization of HPSFA solution-treated at 1,473 K for 0.5 hour (no aging) (a) iso-concentration surface of 5-at.-% Ni (green) and 5-at.-% Ti (yellow), and atom maps (b) Al, (c) Ni, (d) Fe, and (e) Ti.

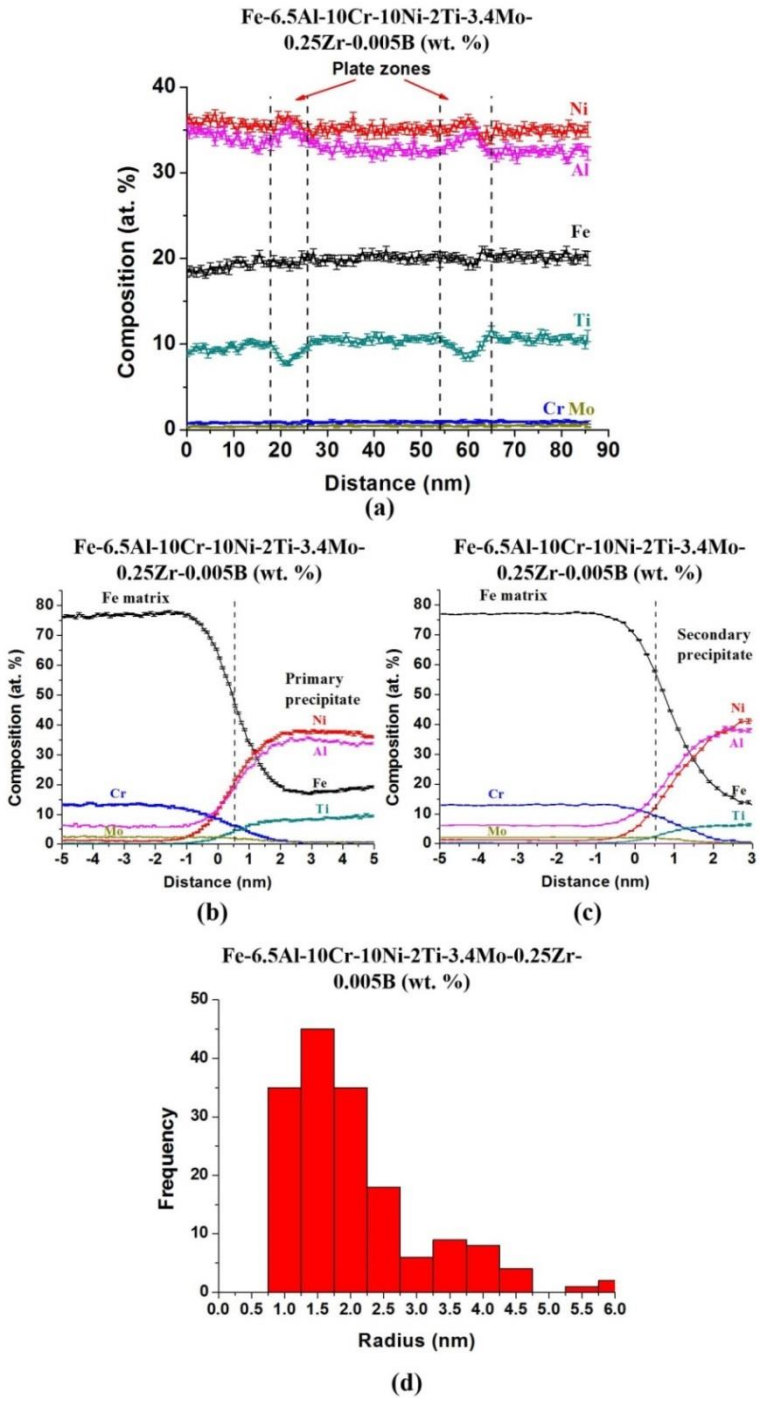

Figure 30. Composition profiles (a) along the red arrow in Figure 29(a), (b) between the Fe matrix and primary $L2_1$ precipitate, and (c) between the Fe matrix and secondary precipitate.

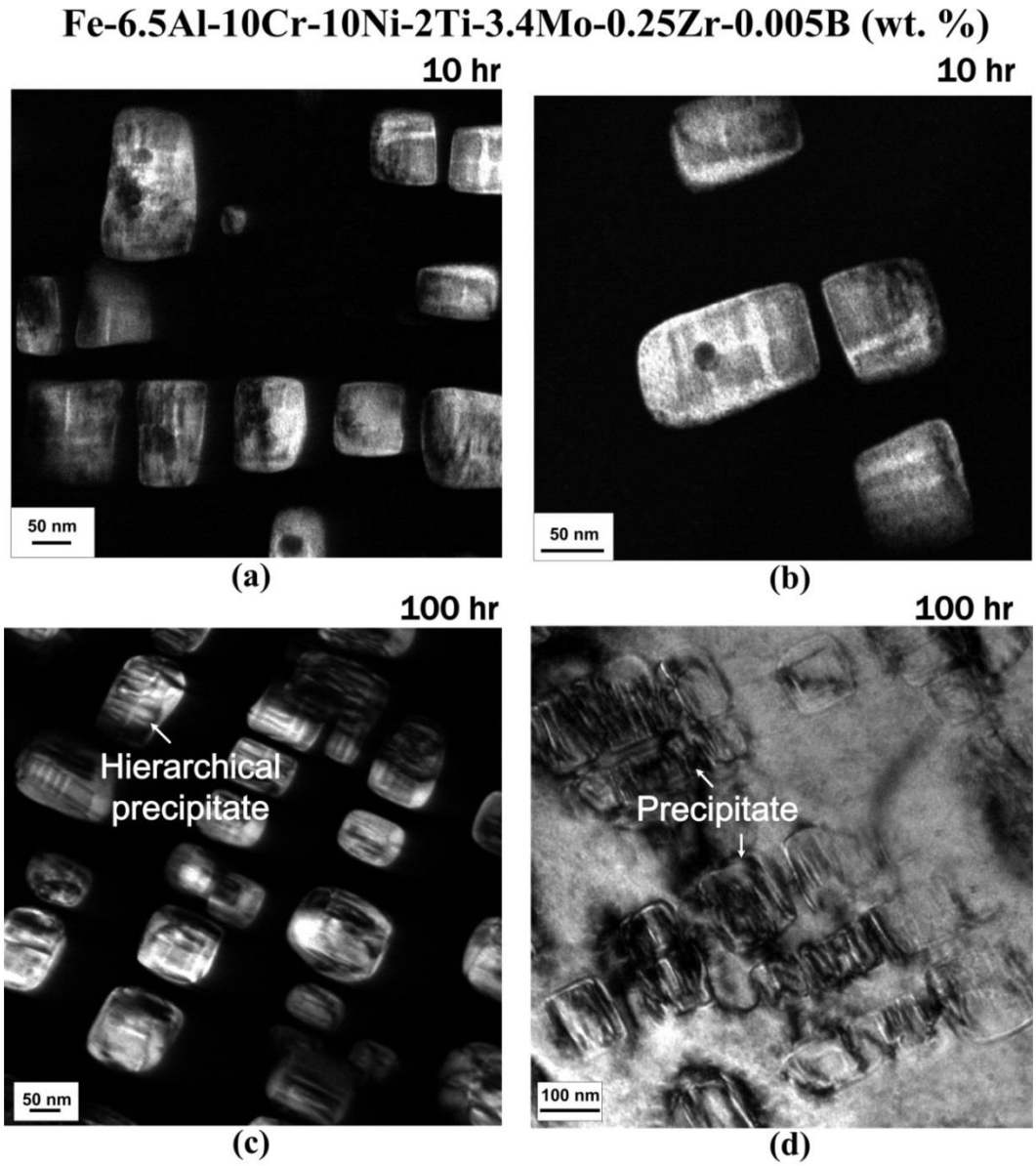

Figure 31. The microstructure of the 2-wt.-%-Ti alloy aged at 973 K for (a)-(b) 10 hours and (c)-(d) 100 hours. (a)-(b) Dark-field (DF) transmission-electron microscopy (TEM) images acquired along the (101) zone axis, using the <111> and <222> reflections, respectively. (c) A DF-TEM image along the [100] zone axis using the <002> reflection, and (d) bright-field (BF) TEM image.

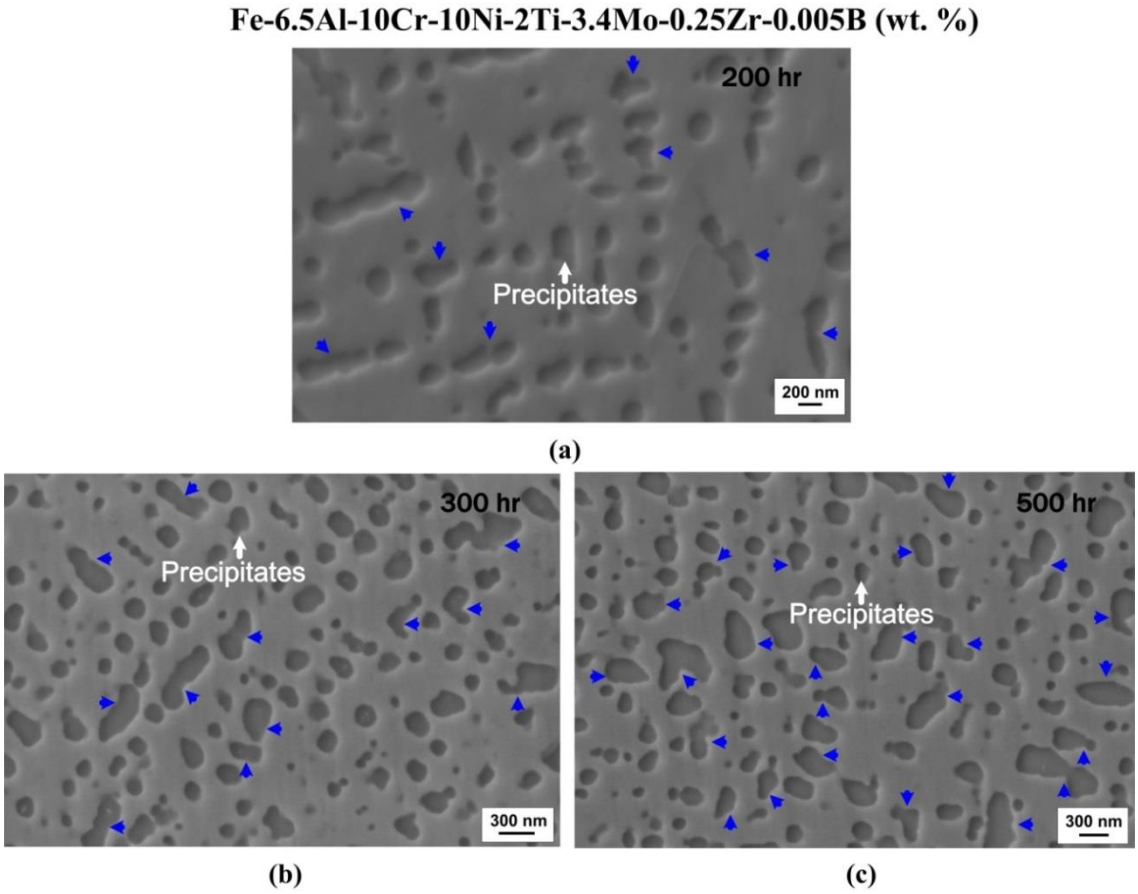

Figure 32. Scanning-electron microscopy (SEM) images of the 2-wt.-%-Ti samples subjected to the solution treatment at 1,473 K for 0.5 hour, followed by aging at 973 K for (a) 200 hours, (b) 300 hours, and (c) 500 hours.

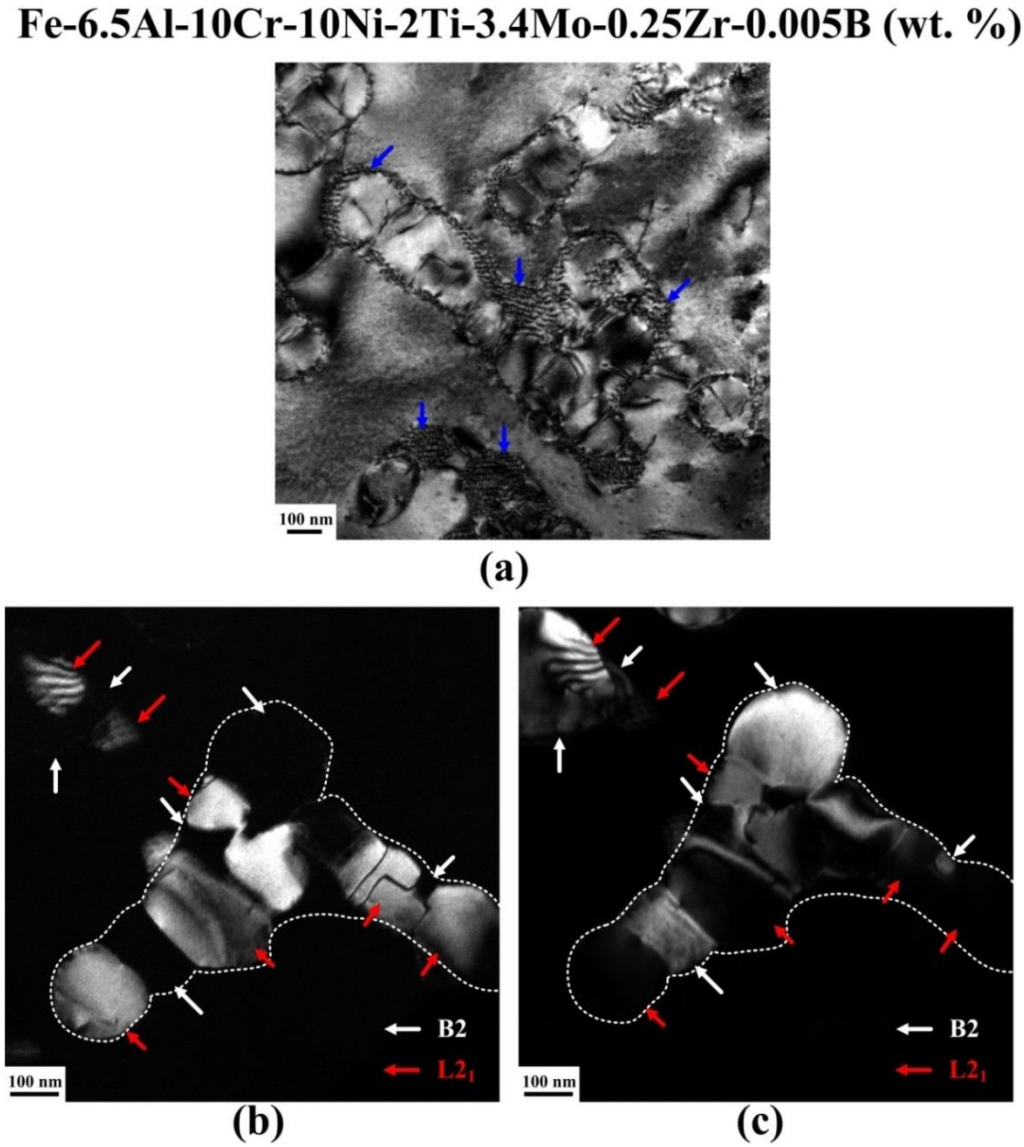

Figure 33. (a) Bright-field (BF), (b) and (c) dark-field (DF) transmission-electron microscopy (TEM) images along the (110) zone axis on the same region for 2-wt.-%-Ti alloy subjected to the aging treatment at 973 K for 500 hours. (b) and (c) DF images are taken using the <111> and <222> reflections, respectively. White dotted lines indicate the overall morphology of the precipitate in (a), and white and red arrows denote the B2 and $L2_1$ phases in (b) and (c), respectively.

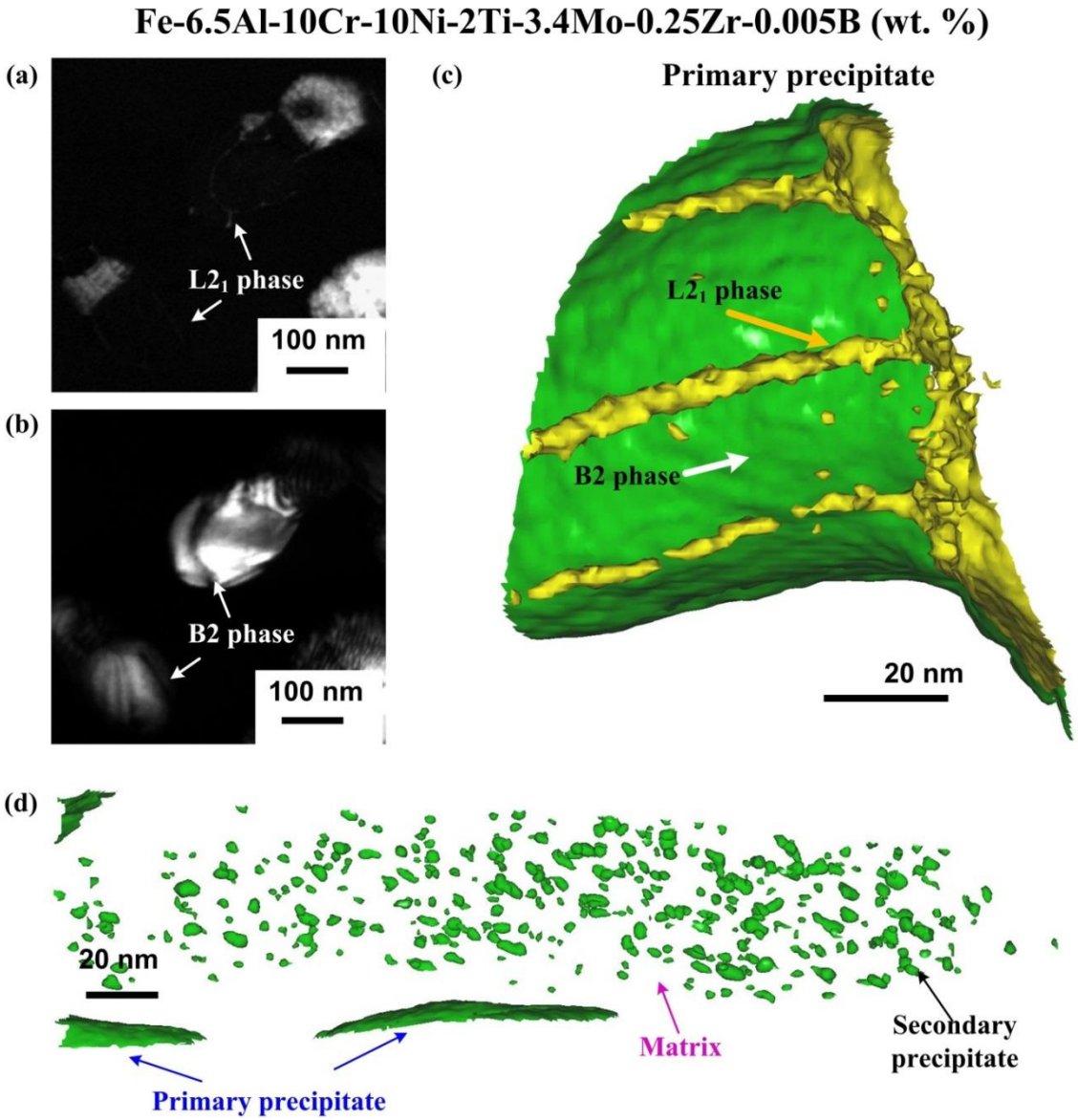

Figure 34. TEM and APT characterization of HPSFA aged for 500 hours. (a)-(b) dark-field (DF) transmission-electron-microscopy (TEM) images and (c) two iso-concentration surfaces of 10-at.-% Ti (yellow) and 10-at.-% Ni (green). The DF-TEM images (a) and (b) are acquired on the same region along the (101) zone axis using the <111> and <222> reflections, respectively. (d) An iso-concentration surface of 7.6-at.-% Ni.

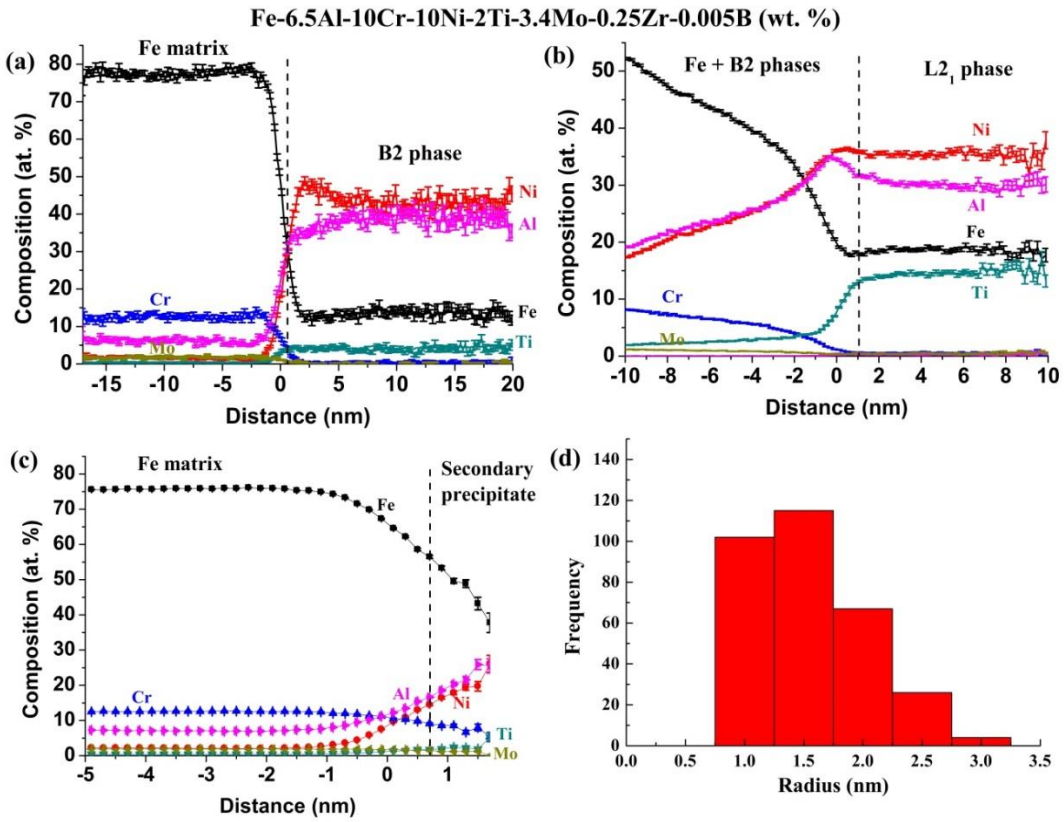

Figure 35. APT characterization of HPSFA aged for 500 hours. (a) and (b) Proximity histograms of 15-at.-% Ni and 7.5-at.-% Ti iso-concentration surfaces, respectively. (c) A proximity histogram of the secondary precipitates shown in Figure 34(d) for the HPSFA sample aged at 973 K for 500 hours after the 1,473 K, 0.5 hour solution-treatment, and (d) a radius-frequency histogram of the small precipitates obtained from the iso-concentration surface of 7.6-at.-% Ni in Figure 34(d).

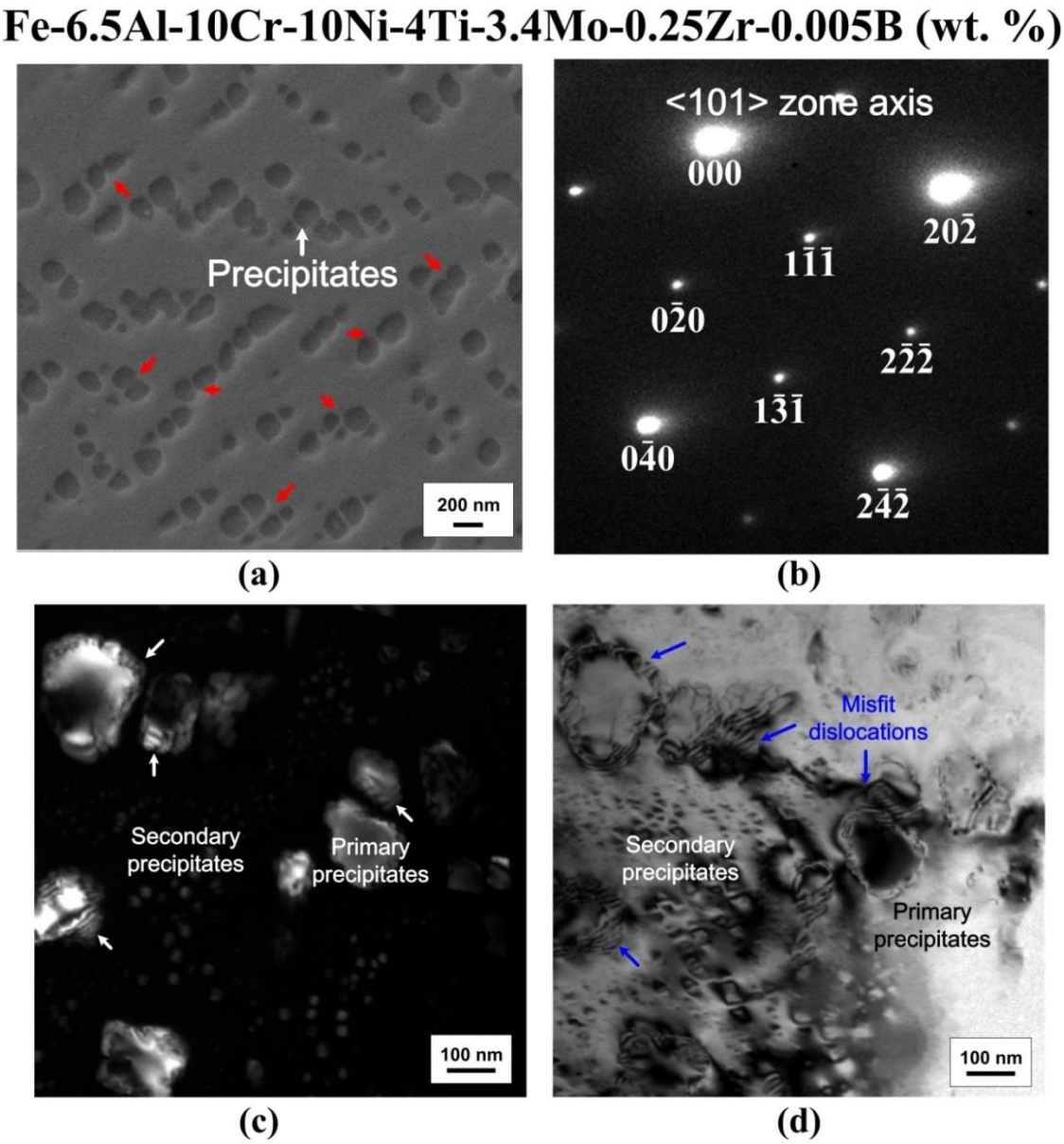

Figure 36. (a) A scanning-electron-microscopy (SEM) image, (b) a selected-area-diffraction-pattern (SADP) along the (101) zone axis, (c) dark-field (DF) transmission-electron-microscopy (TEM) image using the <111> reflection, and (d) a bright-field (BF) TEM image for the 4-wt.-%-Ti sample only solution-treated at 1,473 K for 0.5 hour, followed by air cooling.

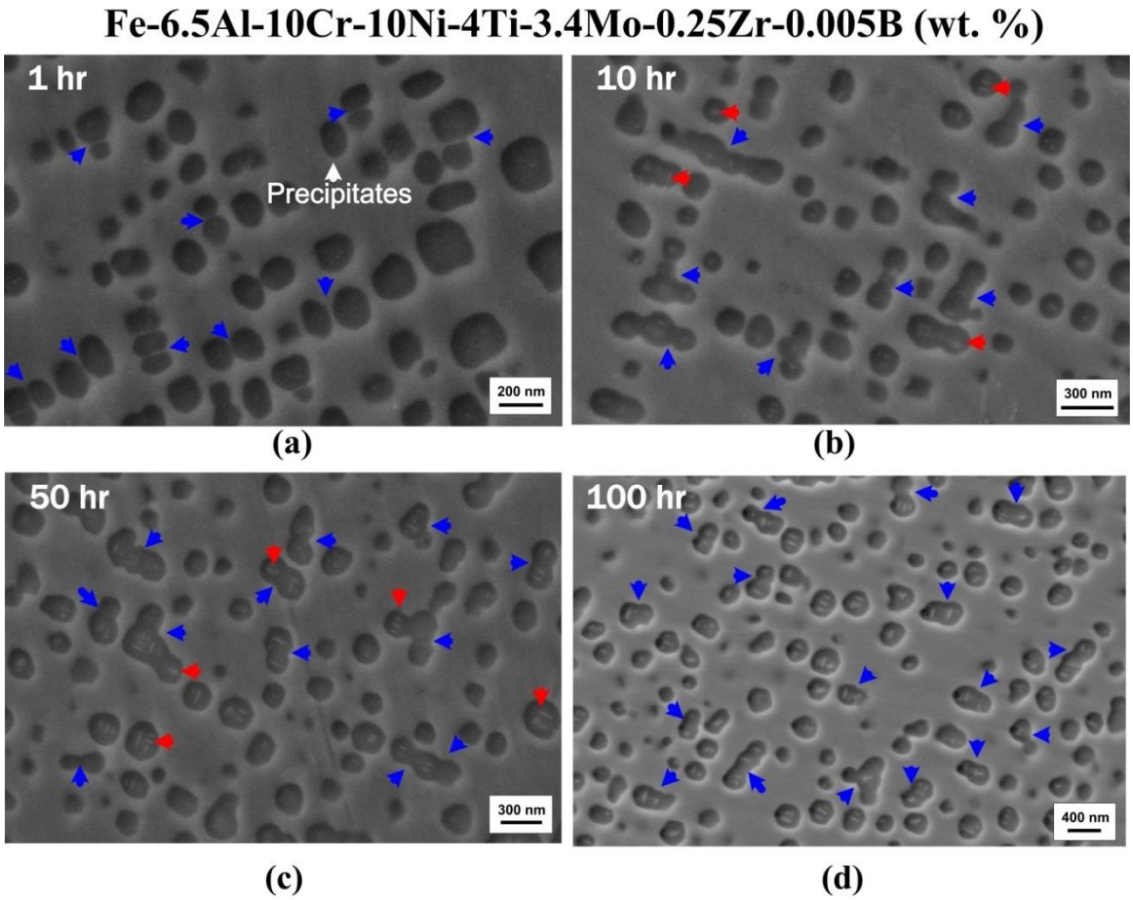

Figure 37. Scanning-electron microscopy (SEM) images of the 4-wt.-%-Ti samples subjected to the solution treatment at 1,473 K for 0.5 hour, followed by aging at 973 K for (a) 1hour, (b) 10 hours, (c) 50 hours, and (d) 100 hours.

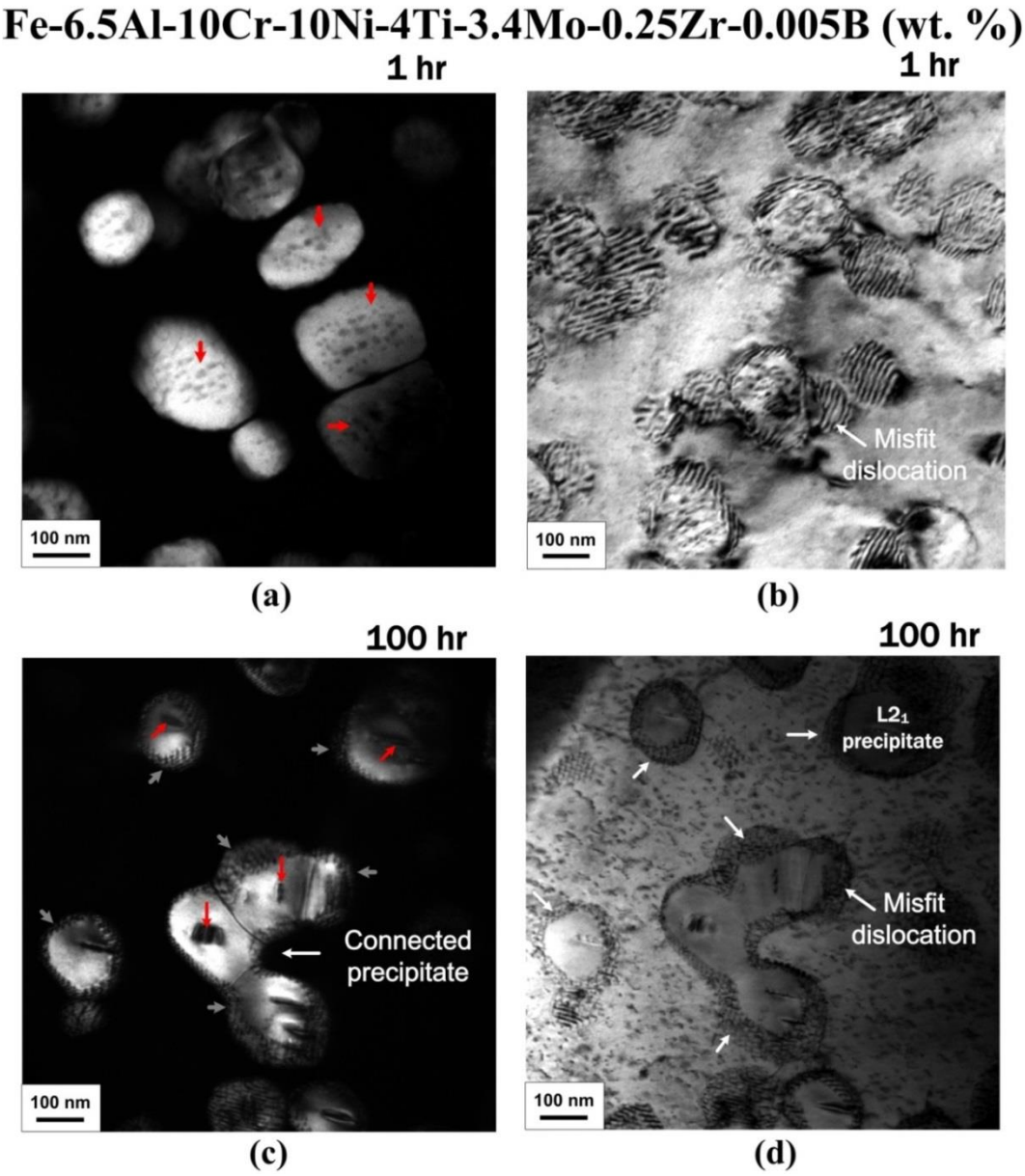

Figure 38. (a) and (c) Dark-field (DF) and (b) and (d) bright-field (BF) transmission-electron-microscopy (TEM) images of the 4-wt.-%-Ti samples subjected to the solution treatment at 1,473 K for 0.5 hour, followed by aging at 973 K for 1 hour (a)-(b), and 100 hours (c)-(d). DF-TEM images in (a) and (c) are acquired along the <101> zone axis using the <111> reflection.

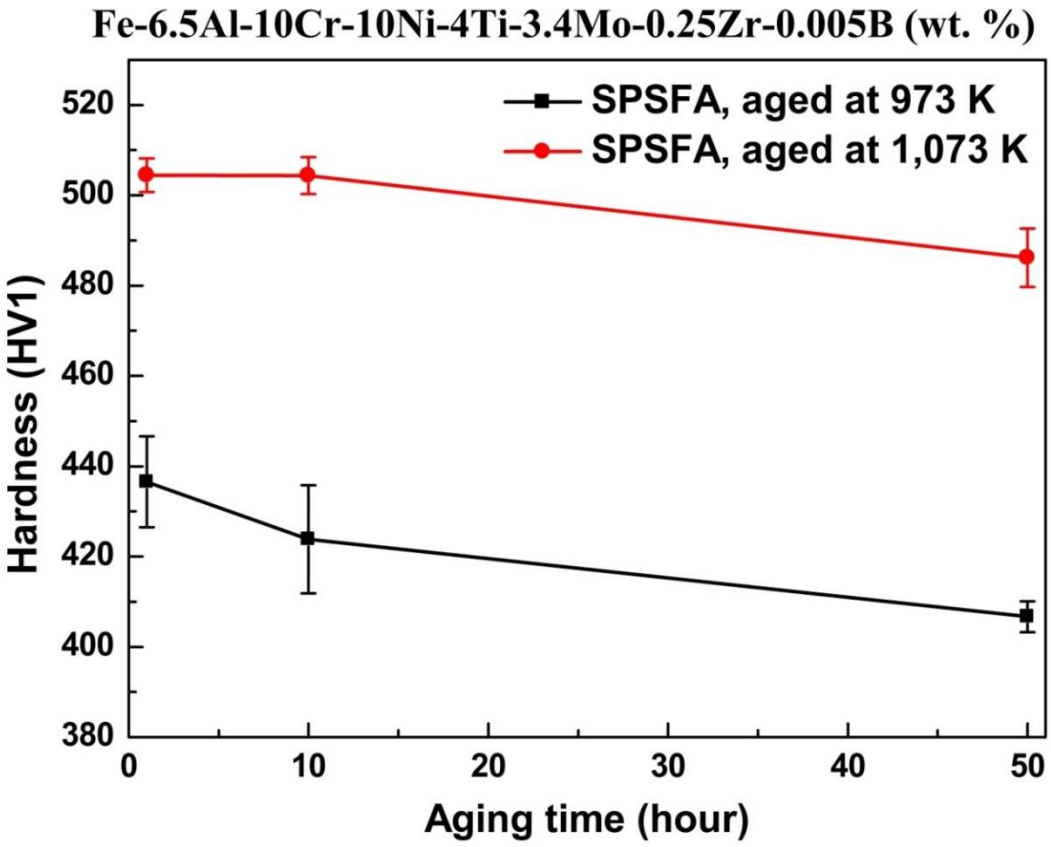

Figure 39. Hardness as a function of aging time at 973 and 1,033 K after the solution-treatment at 1,473 K for 0.5 hour for SPSFA.

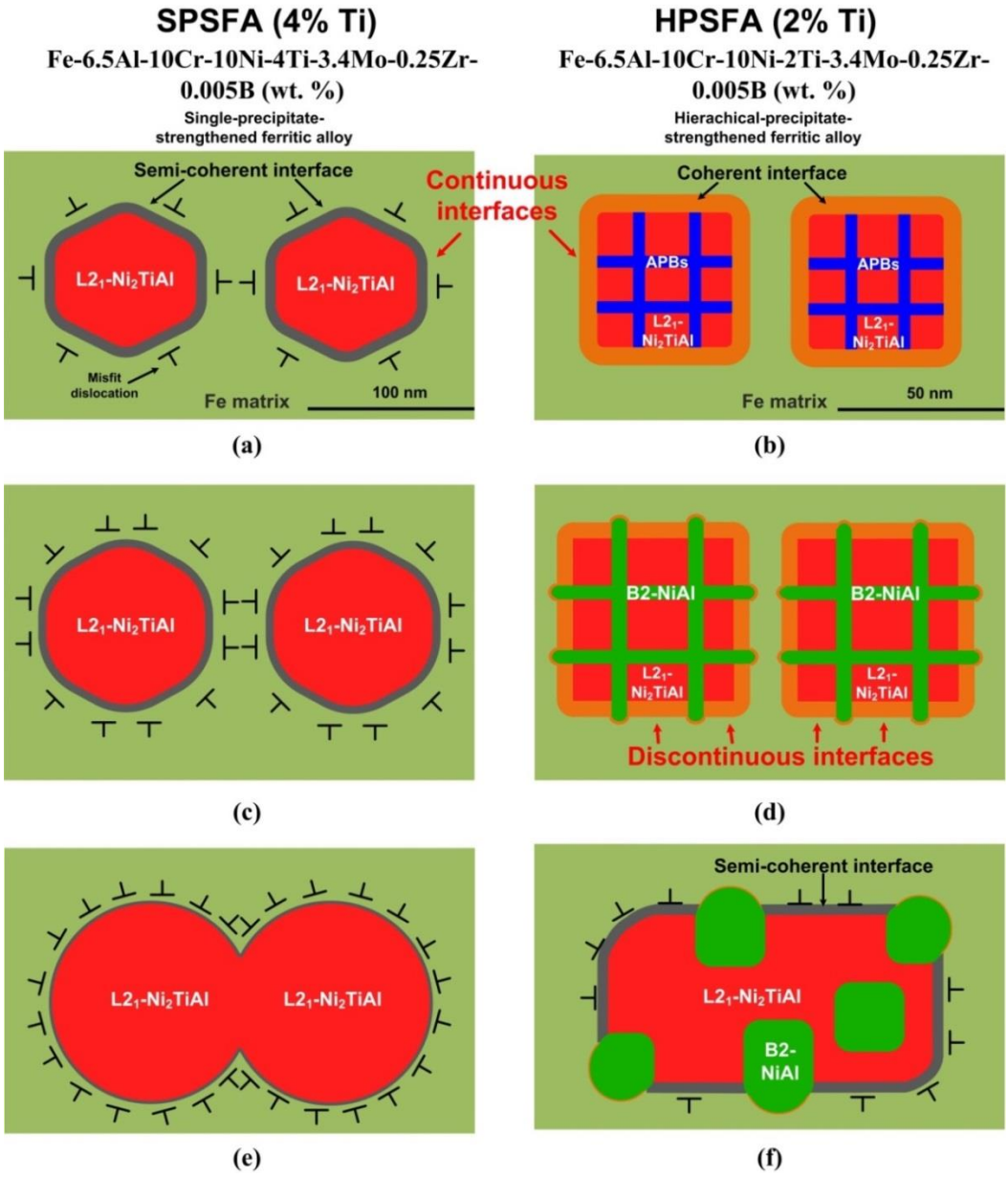

Figure 40. Schematic illustrations exhibiting the microstructural evolution of [(a), (c), and (e)] SPSFA and [(b), (d), and (f)] HPSFA during the aging treatments. The gray and orange colors of the interface lines between the Fe matrix and precipitate phases represent the semi-coherent and coherent states, respectively. The thickness of the interface lines indicates the magnitude of the elastic strain.

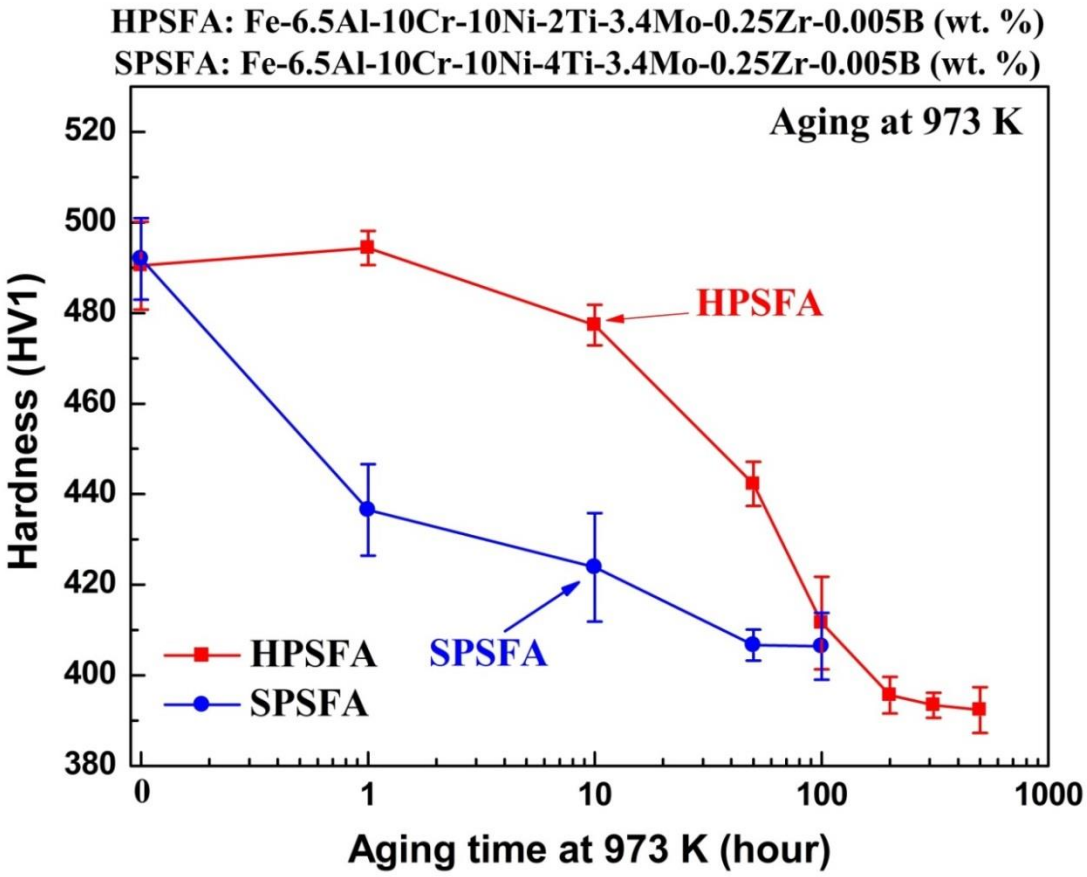

Figure 41. Hardness as a function of aging time at 973 K after the solution treatment at 1,473 K for 0.5 hour for HPSFA and SPSFA.

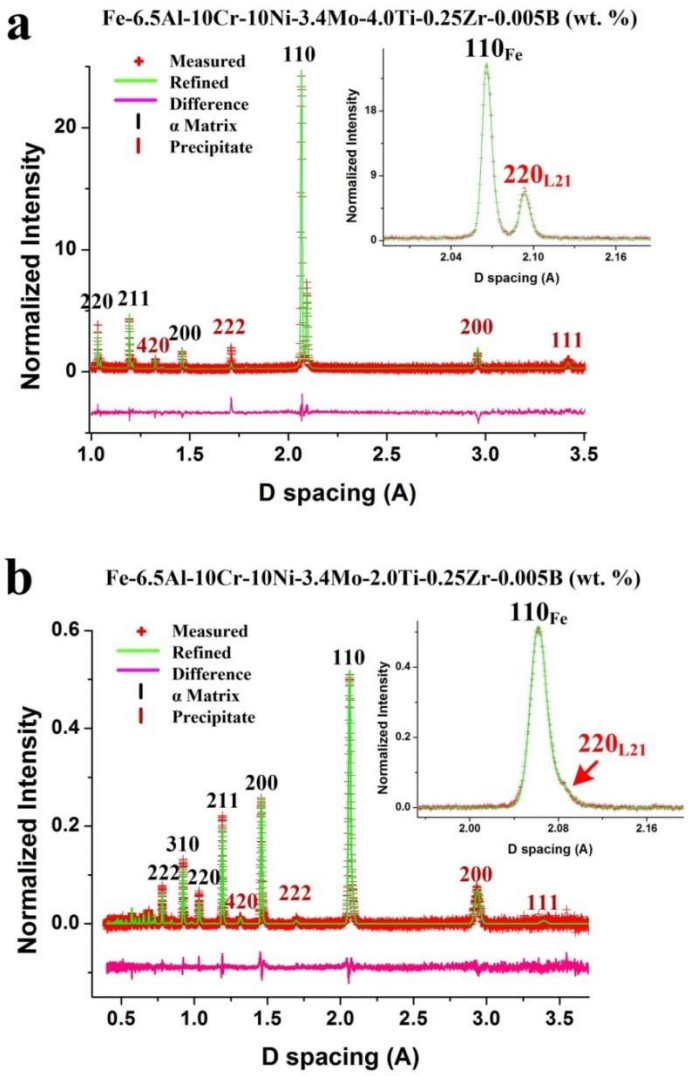

Figure 42. Comparison of the ND results between SPSFA and HPSFA. Representative neutron-diffraction patterns of (a) SPSFA and (b) HPSFA measured at room temperature without loading. Enlarged patterns in (a) and (b) clearly exhibit well-separated and overlapped fundamental $(110)_{Fe}$ and $(220)_{L21}$ peaks for SPSFA and HPSFA, respectively. The red cross represents the measured data. The green curve is the fitted profile using the General Structure Analysis System (GSAS) Rietveld analysis. The pink curve presents the difference between the fitted profile and measured data.

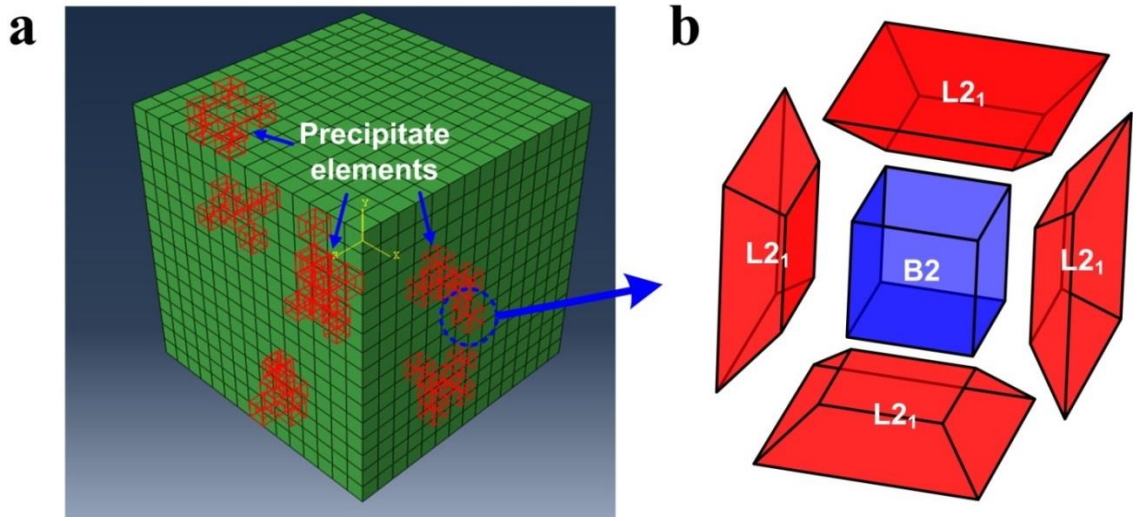

Figure 43. Elemental cubic model for CPFEM (a) Schematic illustration of a 15 × 15 × 15 elements cubic model, employed in the simulation of HPSFA, and (b) the detailed structure of a modeled precipitate element consisting of 6 trapezoidal elements of the $L2_1$ phase (only 4 elements are shown for better visualization) and a centered-cubic element of the B2 phase.

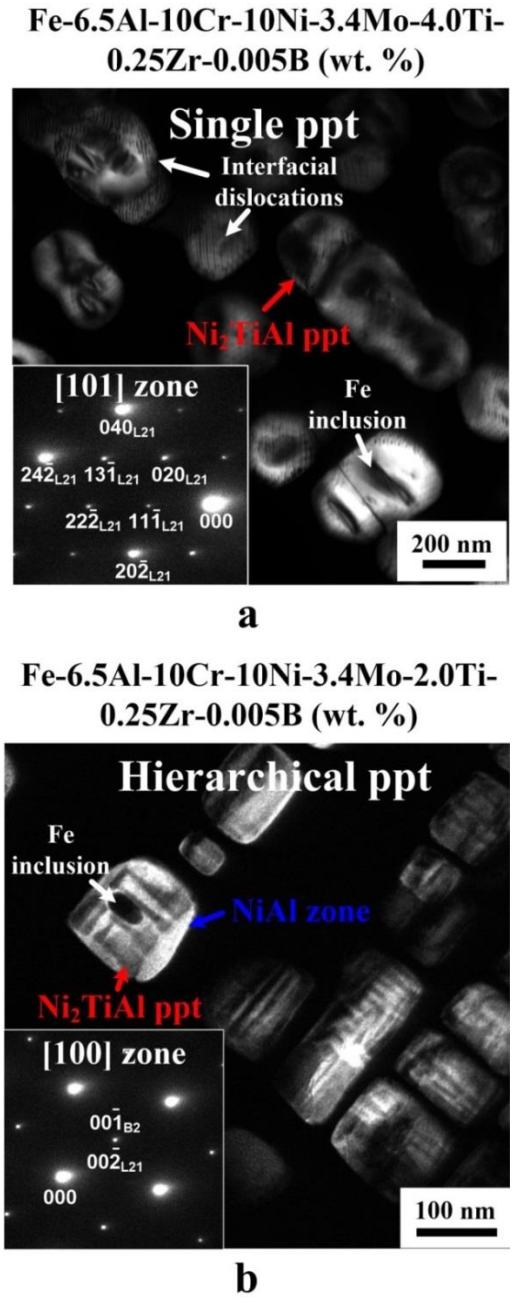

Figure 44. DF-TEM characterization of the precipitates-strengthened ferritic alloys. Dark-field (DF) transmission-electron-microscopy (TEM) images showing the microstructures of (a) SPSFA and (b) HPSFA, and each inset of (a) and (b) shows a selected-area-diffraction pattern (SADP) (ppt stands for precipitate).

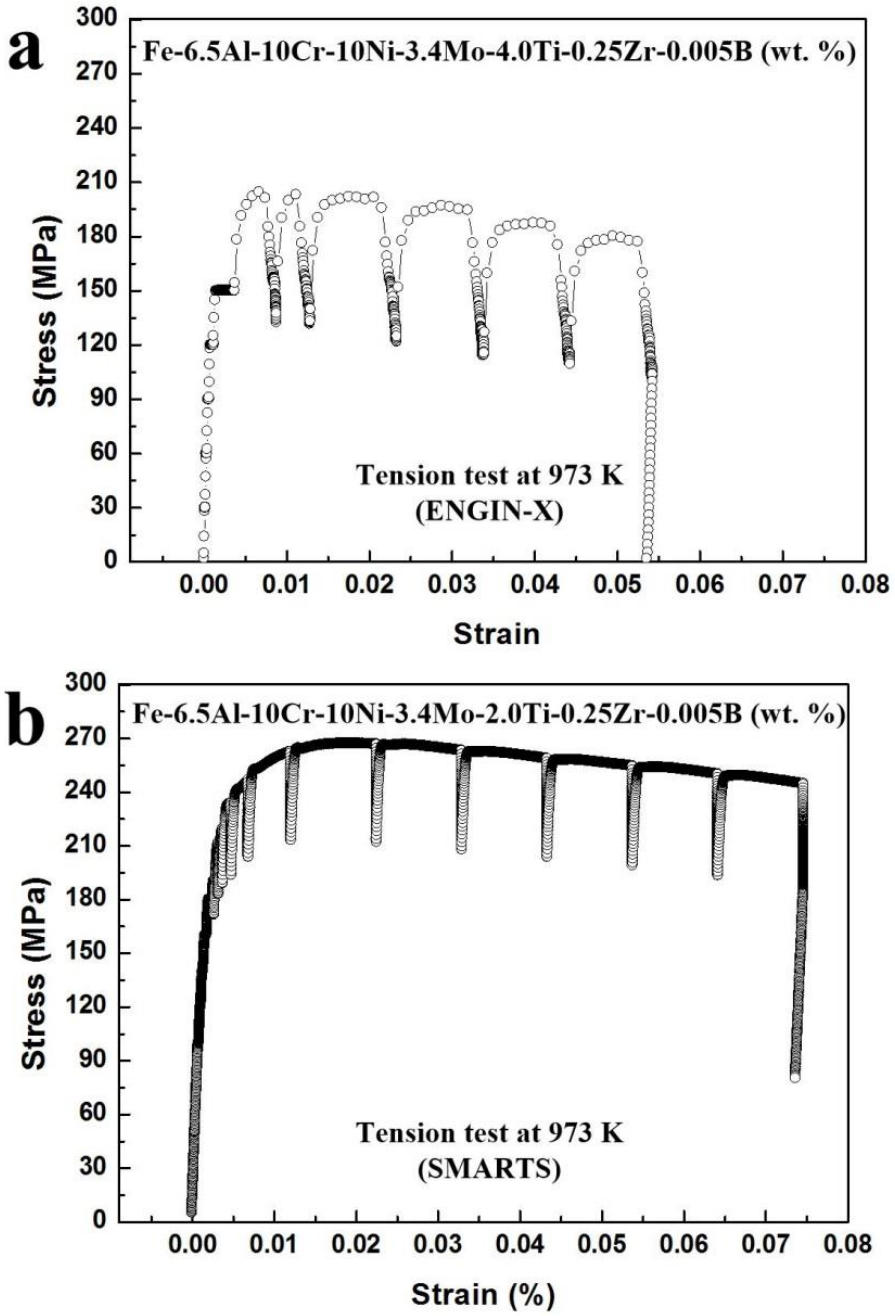

Figure 45. Macroscopic stress-strain curves. Stress-strain curves recorded during in-situ tensile experiments at 973 K for (a) SPSFA and (b) HPSFA.

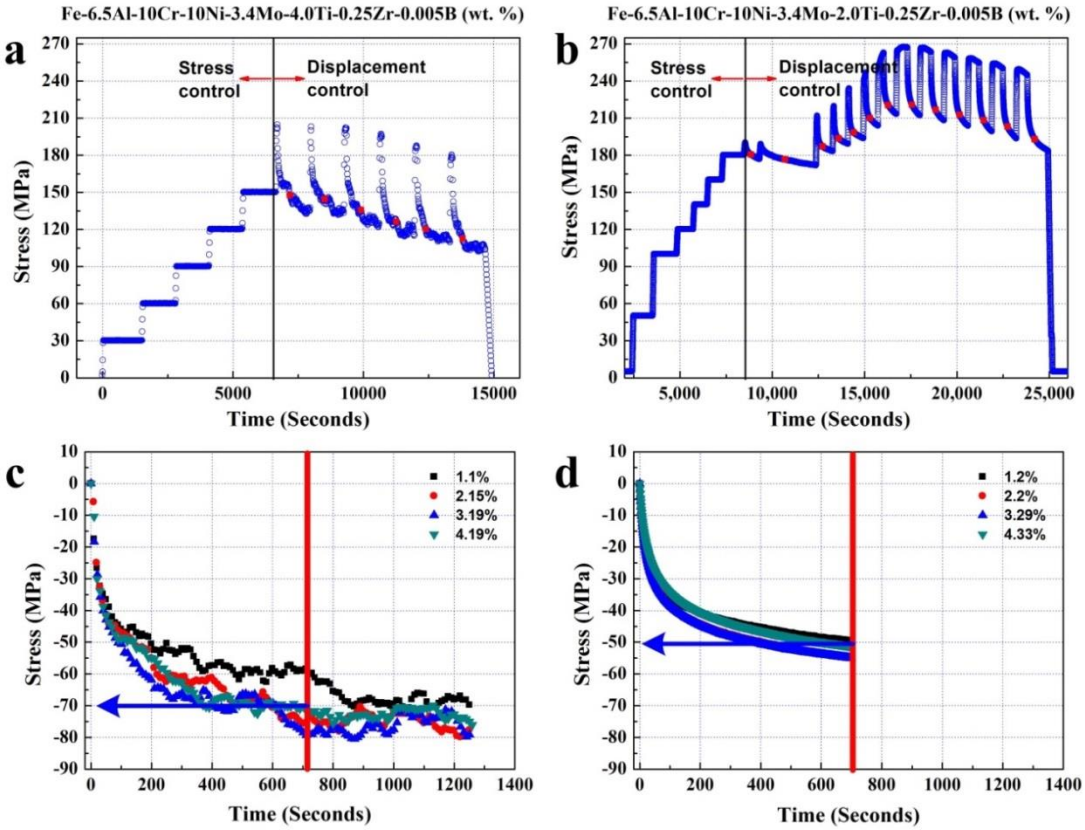

Figure 46. Temporal evolution of macroscopic stress. Temporal evolution of macroscopic stress for (a) SPSFA and (b) HPSFA during the whole in-situ tension experiments at 973 K. Temporal evolution of the relative stress relaxation for (a) SPSFA and (b) HPSFA during ND measurements with respect to the plastic strain.

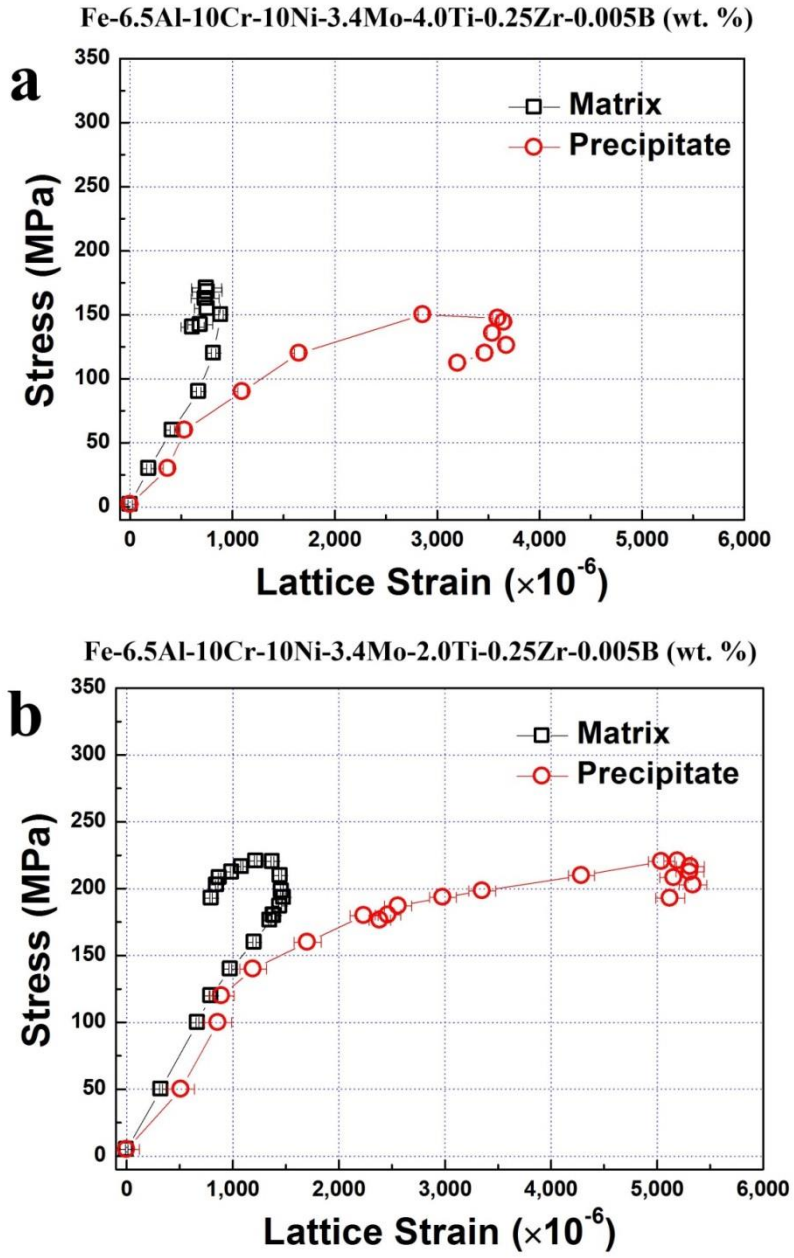

Figure 47. Lattice-strain evolution from the in-situ tension ND experiments. Average phase strains along the axial direction at 973 K as a function of average stress during the in-situ tension experiments on (a) SPSFA and (b) HPSFA.

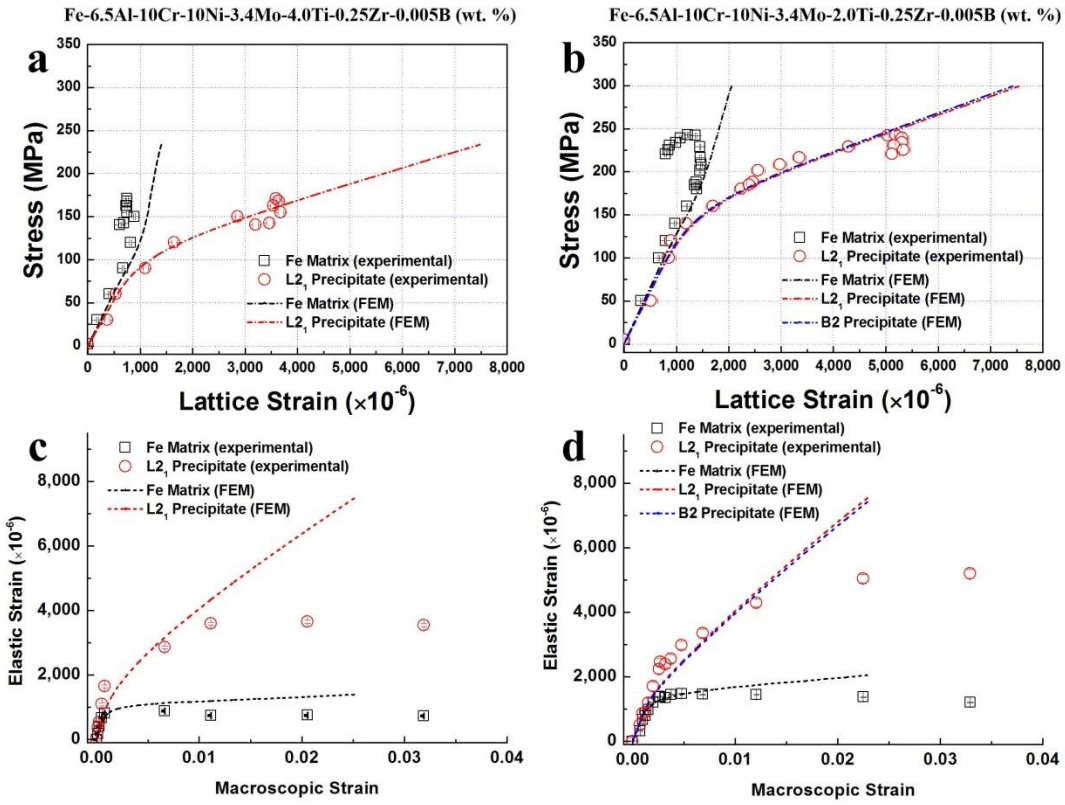

Figure 48. Comparison of lattice-strain evolution between the in-situ tension ND experiments and CPFEM. Average phase strains along the axial direction at 973 K as a function of stress during tension deformation for (a) SPSFA and (b) HPSFA. The evolution of the average strain with respective to the macroscopic strain for (c) SPSFA and (d) HPSFA. Symbols are the experimental data, while lines are the simulated results.

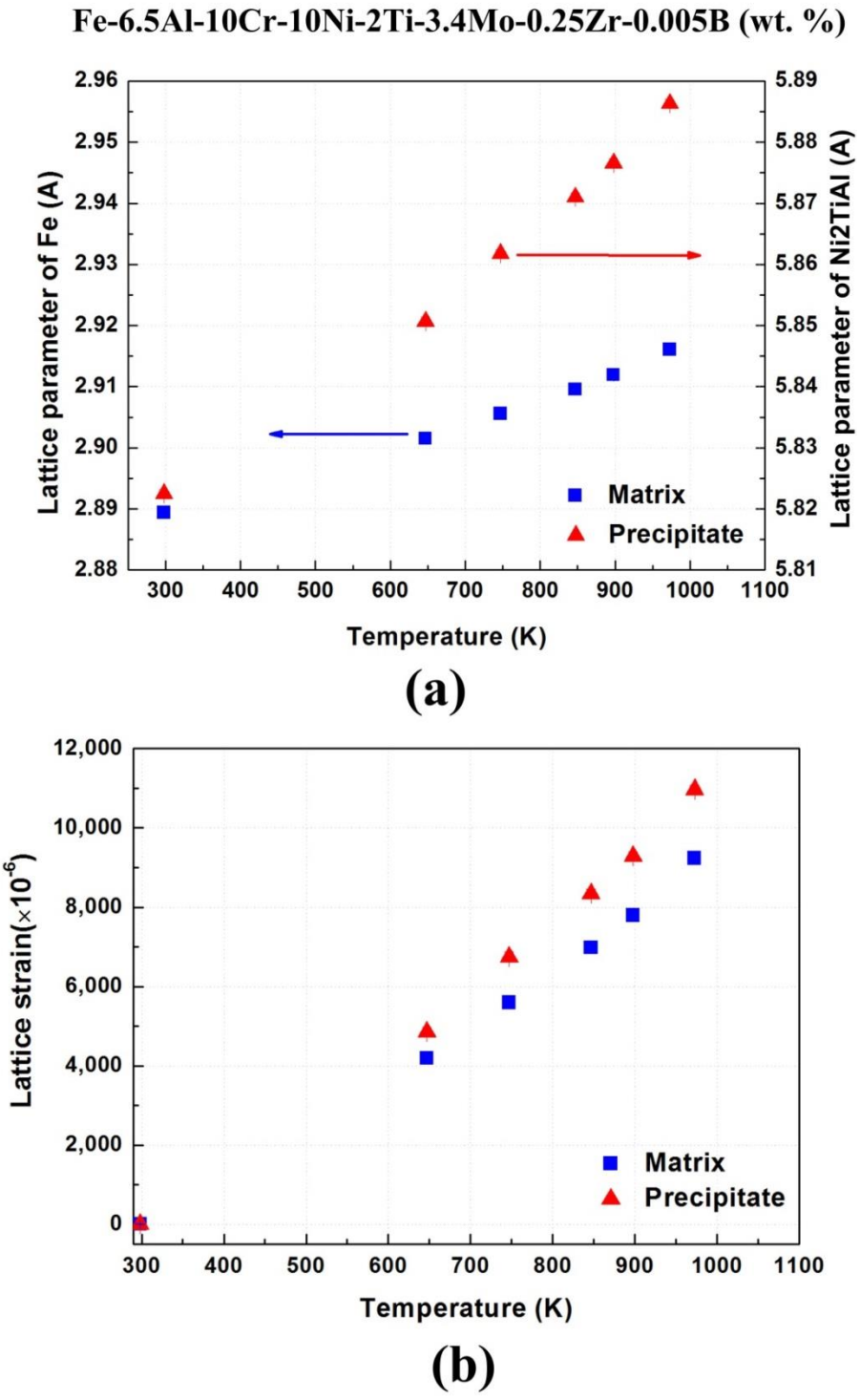

Figure 49. Plot of (a) lattice parameter and (b) thermal strain of α-Fe and Ni_2TiAl phases of HPSFA as a function of temperature.

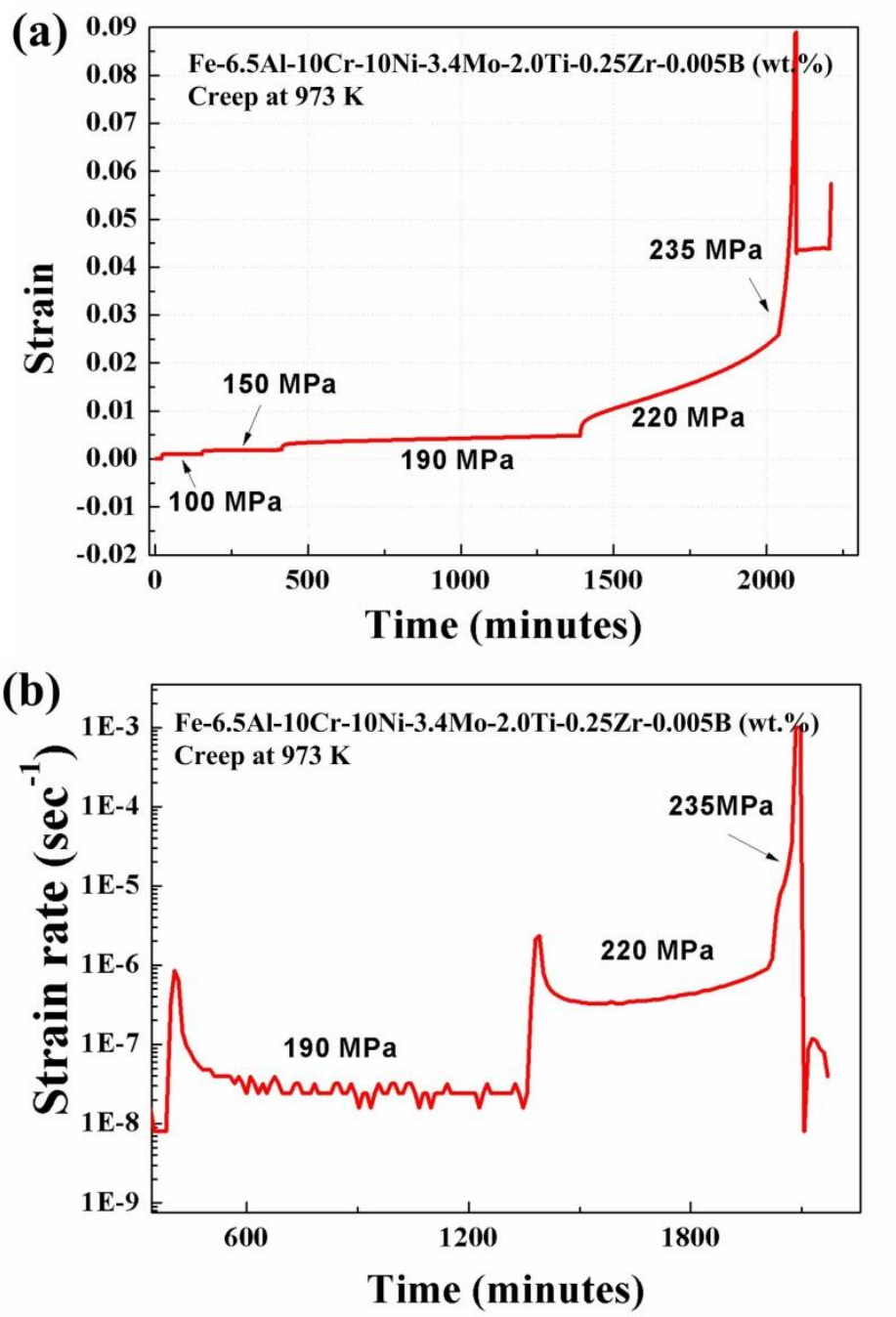

Figure 50. (a) Creep-strain versus time at 973 K and (b) corresponding strain-rates versus time at 190, 220, and 235 MPa in a step-loading creep test.

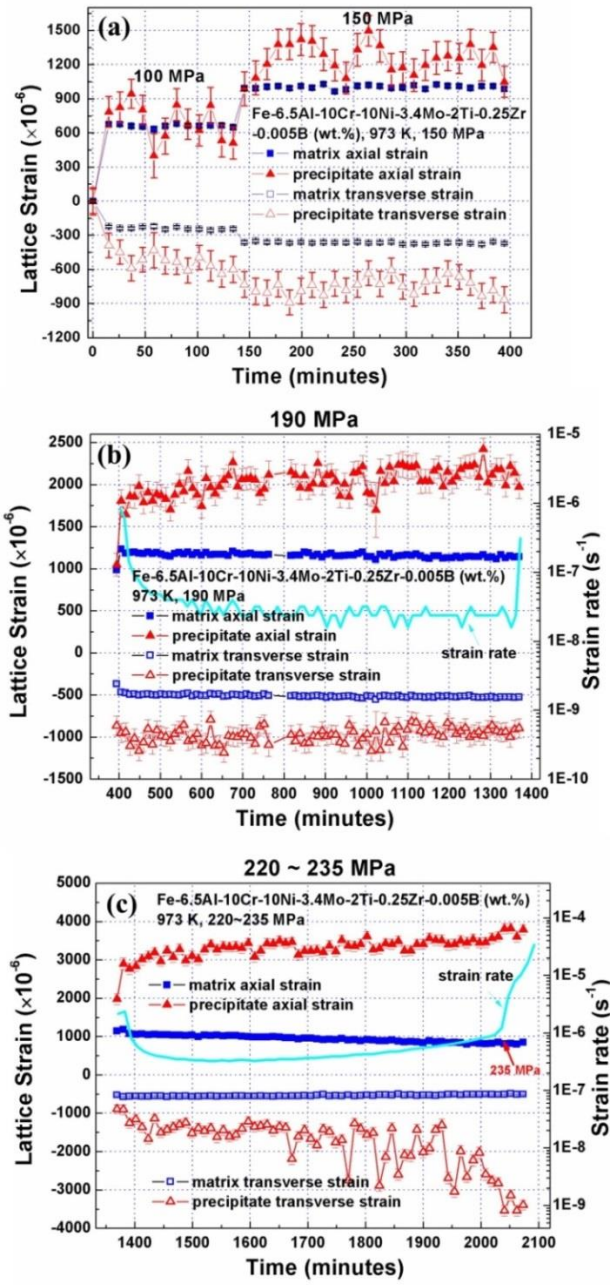

Figure 51. Average phase-strain evolution of α-Fe and Ni_2TiAl phases in axial and transverse directions at (a) 100 and 150 MPa, (b) 190 MPa, and (c) 220 and 235 MPa. Corresponding strain-rate curves vs. time at (b) 190 MPa and (c) 220 and 235 MPa are included.

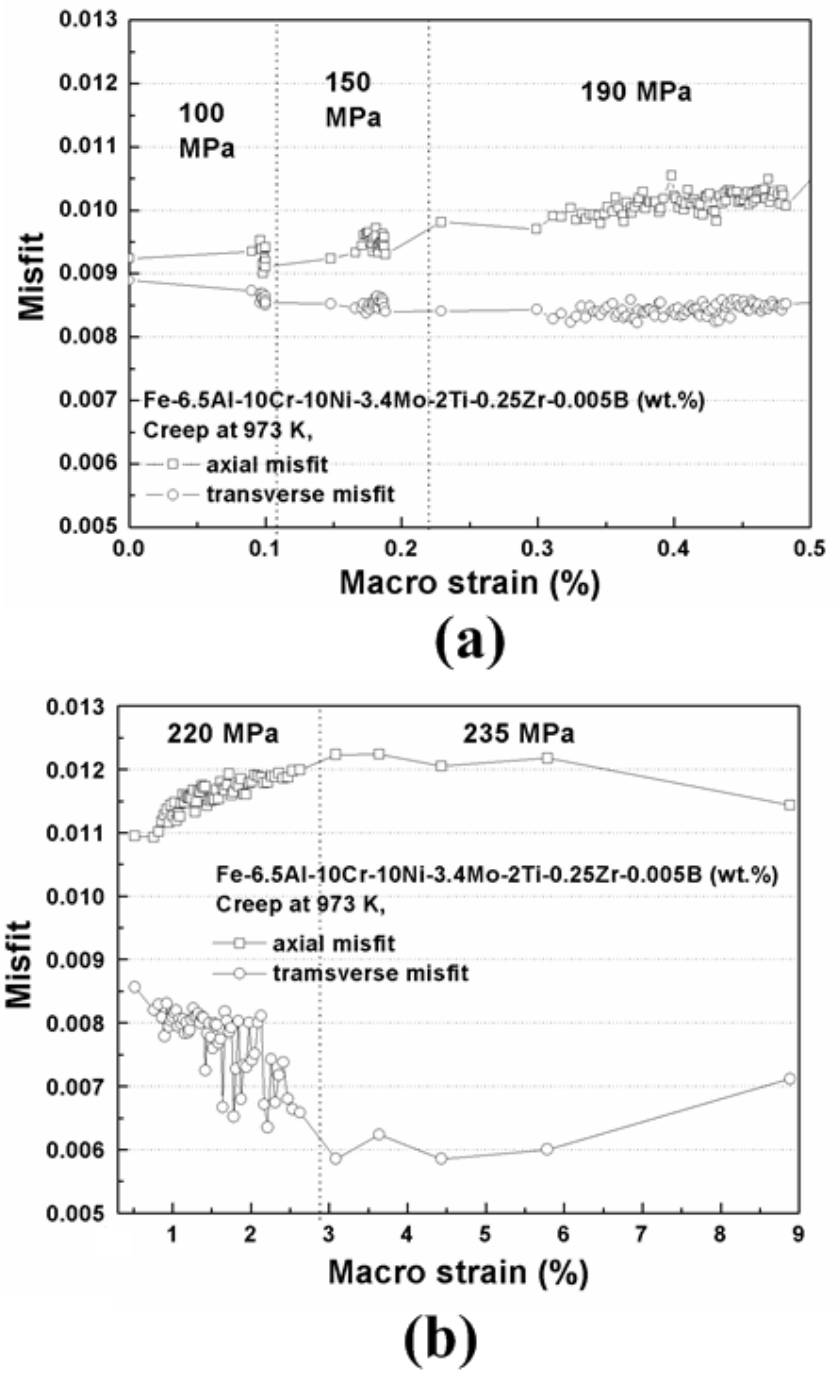

Figure 52. Lattice-misfit evolution along the axial direction as a function of macroscopic strain during the entire step-loading creep at 973 K.

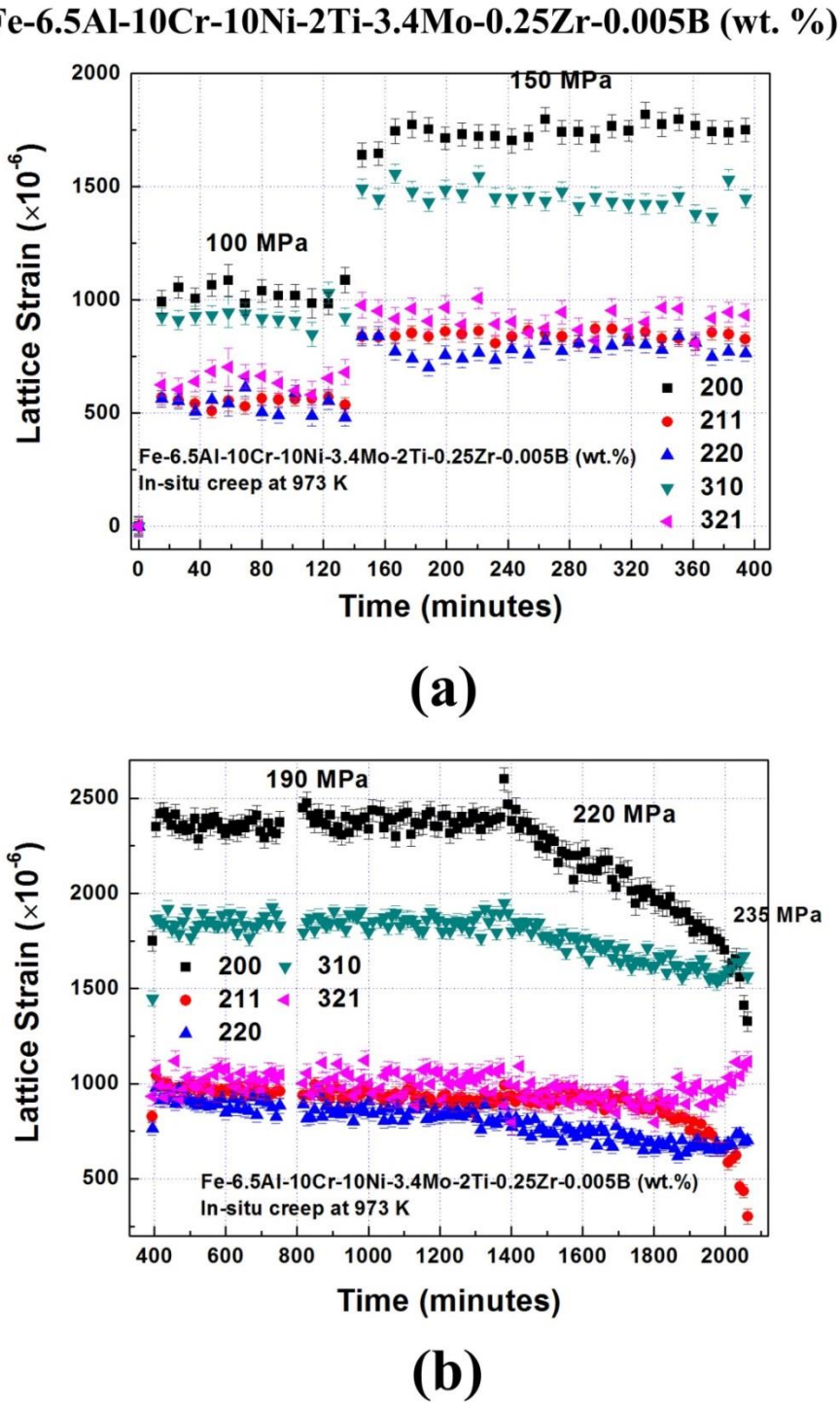

Figure 53. Temporal (hkl) plane-specific strain evolution along the axial direction at 973 K during the in-situ creep, (a) 100 and 150 MPa, (b) 190, 220, and 235 MPa.

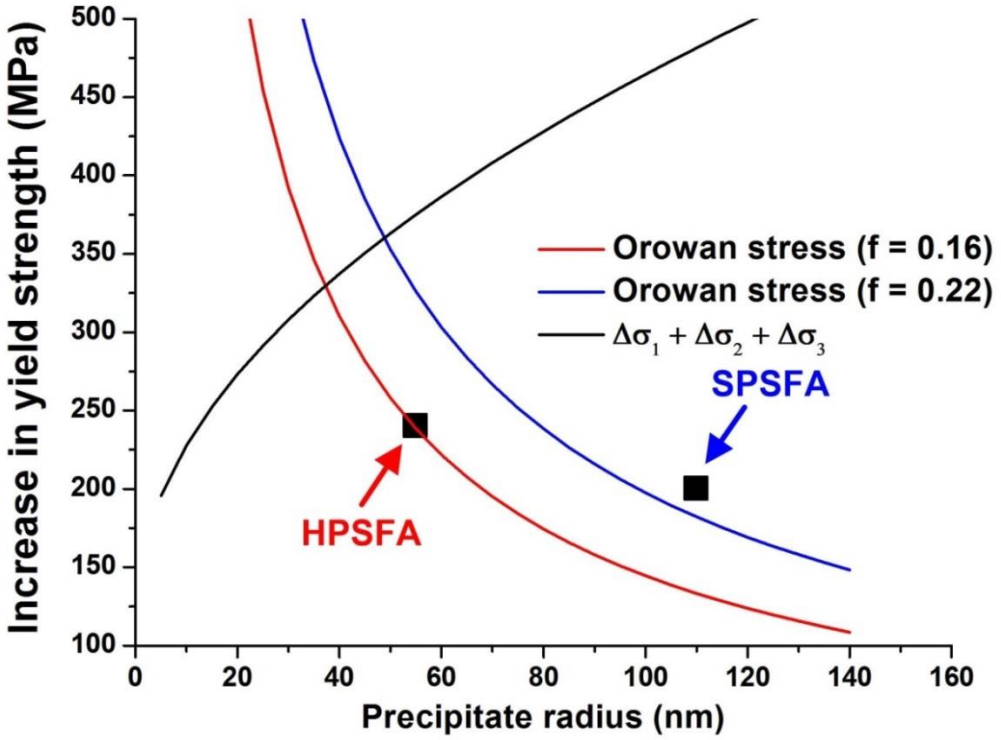

Figure 54. Strengthening contributions. Increase in yield stress as a function of precipitate radius at 973 K. Experimental points are obtained from the 0.2-%-yield stress measurements (Figure 45), and the theoretical lines are calculated from Eqs. [25] – [29] for the Orowan stress (σ_{OR}) and shearing stress due to the ordering ($\Delta\sigma_1$), lattice mismatch ($\Delta\sigma_2$), and modulus mismatch ($\Delta\sigma_3$) contributions.

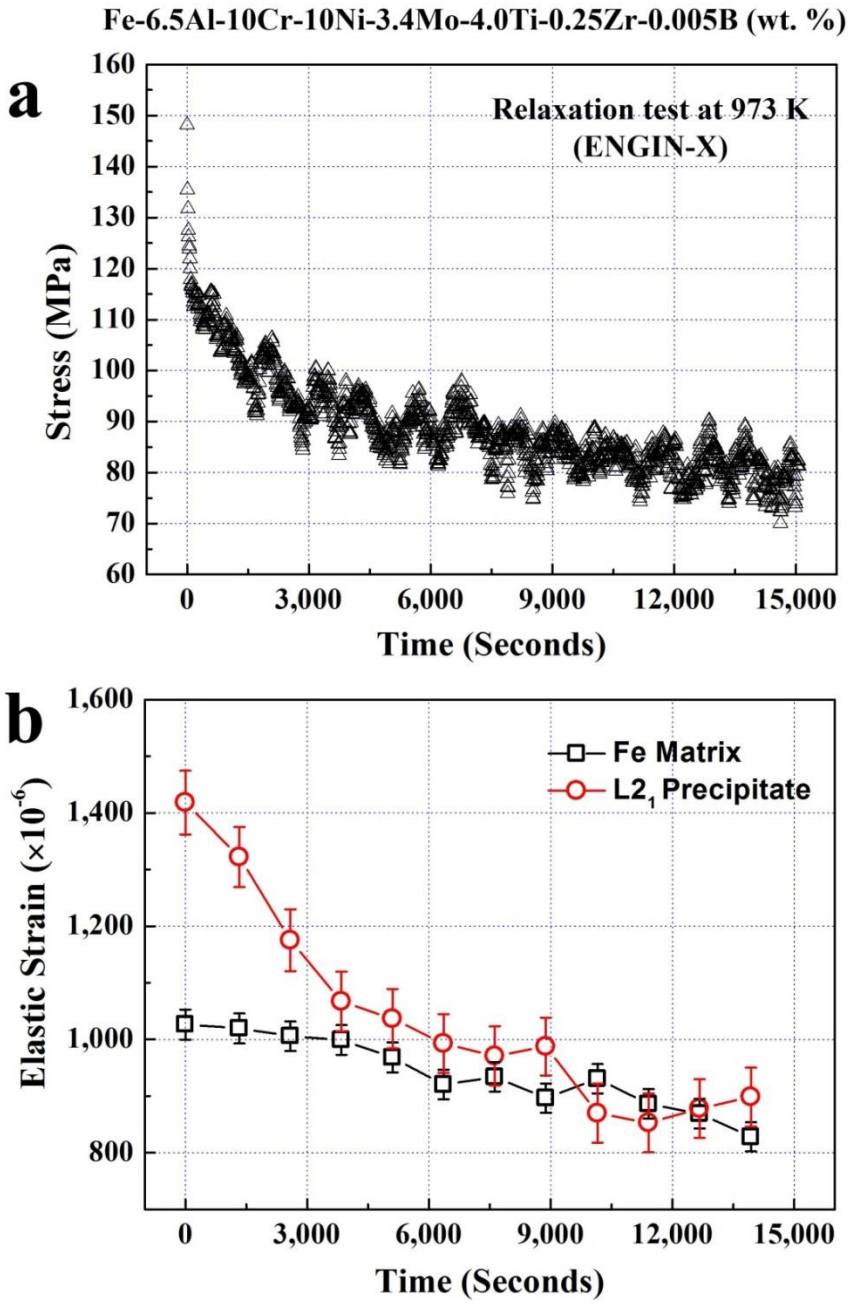

Figure 55. Temporal evolution of stress relaxation. (a) Temporal evolution of the macroscopic stress for SPSFA and (b) corresponding evolution of the elastic strain of the Fe and $L2_1$ phases during the stress relaxation at 973 K.

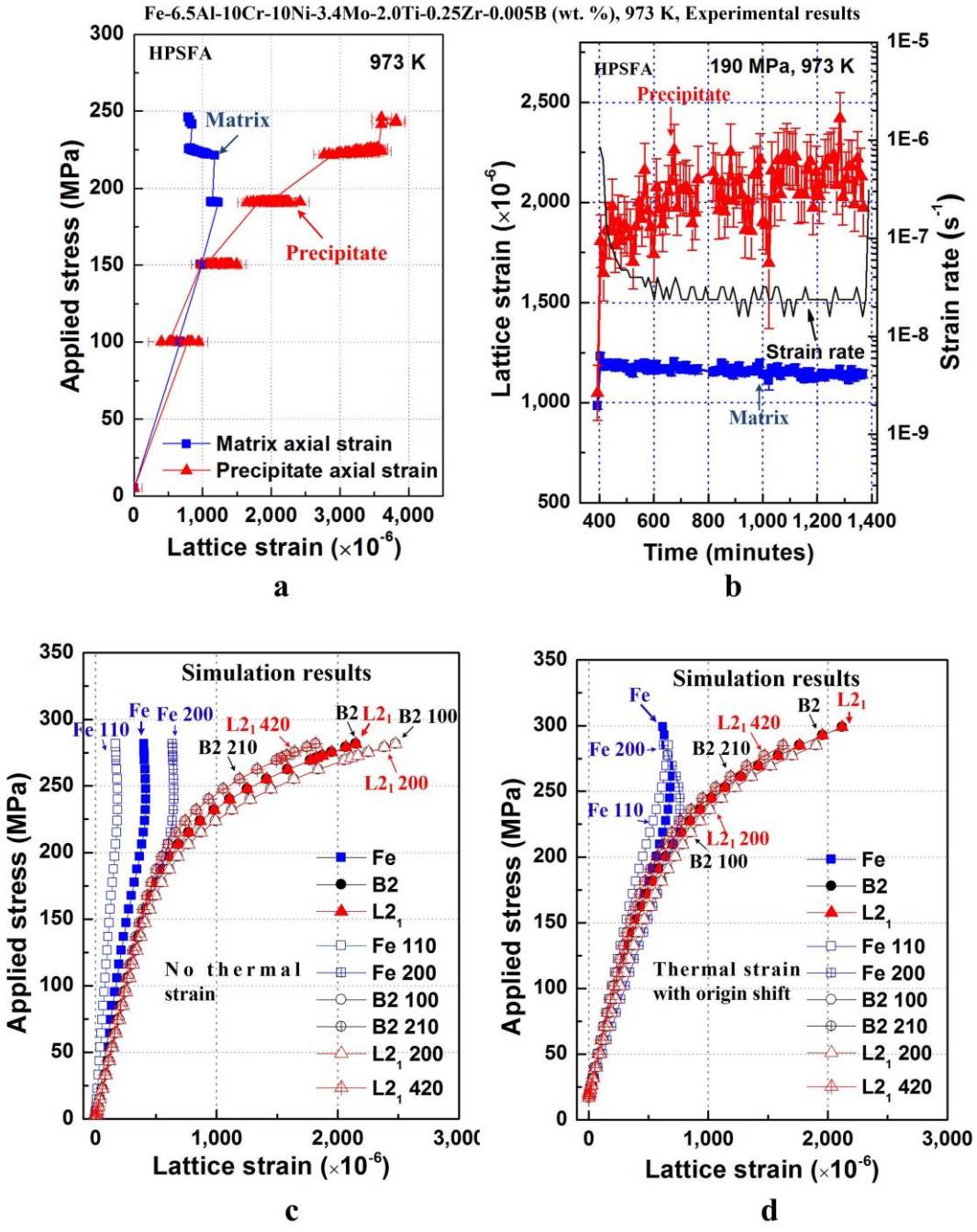

Figure 56. Lattice-strain evolution in HPSFA obtained from the in-situ creep ND experiments and CPFEM. (a) Average phase strains along the axial direction at 973 K as a function of applied stress during the entire in-situ creep experiments on HPSFA. (b) Average phase-strain evolutions of Fe and $L2_1$ phases in the axial direction during in-situ

creep deformation at 190 MPa and 973 K. The strain evolution of the Rietveld average and (hkl) plane lattices at 973 K under a uniaxial compressive stress, obtained using finite-element crystal-plasticity simulations (c) without and (d) with thermal residual stresses, respectively. Note that the (hkl) planes of the B2 and BCC Fe phases correspond to (2h2k2l) planes of the $L2_1$ phase, since a $L2_1$ unit cell contains eight unit cells of the B2 structure. [closed symbols: Rietveld average strains, open symbols: (hkl) plane strains]

VITA

Gian Song was born and grew up in the city of Seoul, Korea on April 24, 1981. He graduated with a B.S. degree and M.S. degree from the Department of Materials Science and Engineering at Sejong University, Seoul in 2008 and 2010. He subsequently joined the Department of Materials Science and Engineering at The University of Tennessee, Knoxville to start his Ph.D. study on August, 2011. In February 2016, he graduated from the University of Tennessee with Doctor of Philosophy degree in Materials Science & Engineering (concentrated in Metallurgy).